

DESIGN OF FAST-CHARGING PROFILES FOR THE PORSCHE TAYCAN EV BATTERY MODULE BASED ON ELECTROTHERMAL MODEL AND EXTENSIVE TESTING

By LUCIA IFUNANYA UWALAKA, B. Eng

A Thesis Submitted to the Department of Electrical & Computer Engineering and the School of Graduate Studies of McMaster University in Partial Fulfilment of the Requirements for the Degree Master of Applied Science

McMaster University © Copyright by Lucia Uwalaka, August 2024

McMaster University

MASTER OF SCIENCE (2024)

Hamilton, Ontario (Electrical and Computer Engineering)

TITLE: Design of Fast-Charging Profiles for the Porsche

Taycan EV Battery Module Based on Electrothermal

Model and Extensive Testing

AUTHOR: Lucia Ifunanya Uwalaka

B. Eng. (African Leadership University, Mauritius)

SUPERVISOR: Dr Ali Emadi

NUMBER OF PAGES: xxi, 123

Lay Abstract

Electric vehicles (EVs) are one of the most noteworthy ways the world is moving toward mitigating the impact of traditional internal combustion engine (ICE) vehicles on the environment. However, one major barrier to their adoption is the charging time, which is significantly longer than the time it takes to fill up a gas tank. Fast charging is one way to address this issue. However, fast charging also comes with the challenge of ensuring that the battery is still kept within safe operating temperatures. This thesis proposes a fast-charging profile for the Porsche Taycan battery module which beats its current fast-charging time designed by Porsche with a lower temperature rise. The method used to achieve this is easily replicated and could be used to design optimal fast charging profiles for other vehicles, enhancing the competitiveness of EVs and bolstering the argument for EVs over ICE vehicles.

Abstract

Fast charging technology is crucial for improving consumer acceptance and rapid adoption of electric vehicles (EVs), but it also poses significant thermal management challenges such as reduced battery life when left uncontrolled, performance degradation, and most importantly, the possibility of thermal runaway. To address these challenges and further improve the competitive advantage of EVs against their internal combustion engine (ICE) counterparts, most EV manufacturers are equipping their vehicles with fast-charging capabilities.

It is certain that temperature is a major limiting factor to the fast-charging capabilities of EVs. Therefore, this thesis addresses this challenge of fast-charging profile design by proposing an efficient electrothermal model to predict temperature rise for any fast-charging profile. The primary goal is to develop a method that generates the optimal fast-charging profile, while reducing charging time and minimising the battery temperature rise.

The electrothermal model is designed using a second-order Thevenin equivalent circuit model (ECM) combined with a simplified electrical equivalent circuit thermal model, whose parameters are obtained from cell characterisation and extensive battery module testing. Using this model, a wide range of current profiles is solved, and the optimal profile is determined. Finally, selected profiles are verified through experimental testing on a battery module. Compared to the reference fast-charging profile used in the production EV, the fastest profile achieved a 3% reduction in charging time with a reduction of 0.7°C in maximum temperature.

To those who believed in me when I couldn't believe in myself. Thank you.

Acknowledgements

I would like to express my sincerest gratitude to my supervisors, Dr Ali Emadi, without whom I would not have had the opportunity to write this thesis. I am eternally grateful for the chance you gave me to learn and grow under your guidance, and for reminding me to believe in myself. I am also deeply thankful to Dr Phillip Kollmeyer who has been the most patient and supportive mentor over the course of this programme. Your wealth of knowledge and experience were an invaluable resource for all my work at the McMaster Automotive Resource Centre (MARC).

Thank you to Josimar Duque, who gave me all my foundational knowledge about batteries and battery testing when I first started, and has always been the most willing and patient teacher. I am also thankful to Qi Yao for all her assistance with all my battery testing challenges, and for always being willing to give me feedback and help me improve.

I am also thankful to my friends, Hams Hefny, Joshua Budisa and Akira Shiguemoto, my support system at McMaster, and Kur Ngong, my support system outside of McMaster. You all helped me cope with the rigors of a master's programme and life alone in a foreign country. I also sincerely thank our industry partners, our research team, who were always supportive and welcoming, and the entire team at MARC, always ready to help, share knowledge and resources, and truly support one another.

I also couldn't have done this with my family and friends back in Nigeria and all over the world – my mother's constant prayers and concern, my father fighting to rise above his ill health to support me emotionally at a time when I needed him the most, my siblings for their patience, undying love and support, thank you for listening to me talk about batteries and trying to learn about them to help me, my nephew, Chinua, whose simple existence always lifts my spirits. Shallom Azuka, who worked so hard to help me become more organised, Achonye Richard Chooby who always put my mental health first, and my day one, Sonia Jamabo for whom I need to write an entire page of gratitude, you are not just friends – you are family. I made it here today, thanks to all of you.

Most of all, I thank God, who has been with me every step of this journey despite my lack of faith, and always shone a light for me in my darkest hour.

Table of Contents

1	Intro	oduction	1
	1.1	Background and Motivation	1
	1.2	Thesis Contributions	2
	1.3	Thesis Outline	3
2	Batt	tery Thermal Management Systems in Fast-Charging EVs	6
	2.1	Classes of Battery Thermal Management Systems	6
	2.1.	1 Air-Cooling	7
	2.1.2	2 Liquid Cooling	7
	2.1.	3 Phase Change Materials (PCMs)	10
	2.1.4	4 Heat Pipes	11
	2.2	Battery Cooling Architectures in Current Fast-Charging EVs	12
	2.2.	1 Air-Cooled Fast Charging Vehicles	13
	2.2.2	2 Liquid-Cooled Fast Charging Vehicles	14
	2.3	Cooling Architecture for the Taycan Battery Module	22
3	Exp	perimental Performance Analysis of LG E-66 Cells from the Porsche Tay	⁄can
В	attery N	Module	24
	3.1	Experimental Setup	25
	3.1.	Single Cell Characterization: Setup and Experimental Procedure	27

3.1.	.2 Module-Level Testing: Setup and Experimental Procedure	29
3.2	Cell Characterization and Module Performance Test Results	36
3.2.	.1 Cell Characterization Results	36
3.2.	.2 Module Test Results	37
3.3	Summary	46
4 Fas	st-Charging Protocols for Lithium-Ion Batteries	47
4.1	Constant Current-Constant Voltage (CCCV)	49
4.2	Multistage Constant Current Charging (MCCC)	50
4.3	Boost Charging (BC)	52
4.4	Pulse Charging (PC)	53
5 Ele	ectrical Model and Simplified Thermal Model of the Porsche Tayor	an Module
55		
5.1	The Thevenin Battery Equivalent Circuit Model	57
5.1.	.1 RC Parameter Estimation	58
5.1.	.2 Validation of Estimated Parameters	61
5.2	Simplified Electrical Equivalent Circuit Thermal Model	62
5.2.	.1 Thermal Model Parameter Identification	65
5.2.	.2 Heat Generation	66
5.2.	.3 Electrothermal Model Validation	67
6 Des	sign Methodology and Selection of the Fast-Charging Profile	71
6.1	Fast-Charging Profile Design Procedure	72

	6.1.	1 Variation 1 – Simple Ramped Step	73
	6.1.	2 Variation 2 – Ramped Step with Initial Step Current	78
	6.2	Simulation of the Designed Profiles with the Electrothermal Model	81
	6.2.	1 Variation 1 Performance – Simple Ramped Step	82
	6.2.	2 Variation 2 Performance – Ramped Step with Initial Step Current	87
7	Exp	perimental Verification of Selected Fast-Charging Profiles	92
	7.1	Verification Test Procedure	92
	7.2	Results for Simple Ramped Step Profile	93
	7.2.	Profile with Modelled Peak Temperature Less than 60°C	93
	7.2.	2 Fastest Designed Profile within Constraints	96
8	Con	aclusions and Future Work	00
	8.1	Summary and Conclusions	00
	8.2	Recommendations and Future Work	02
A	ppendi	x A1	04
A	ppendi	x B	07
R	eferenc	res 1	10

List of Figures

Figure 2.1: Cooling channel paths studied in (Farhan et al., 2022)
Figure 2.2: Cooling plate arrangements studied in (Li et al., 2022)
Figure 2.3: Cooling channel configuration I (single channel), II (small channels), and
III (S-shaped) for the two arrangements in (Li et al., 2022)
Figure 2.4: Cooling plate designs studied in (Monika & Datta, 2022)
Figure 2.5: Cooling media distribution in production fast-charging EVs
Figure 2.6: Range and capacity trends in production EVs
Figure 2.7: Minimum and maximum DC charging power for different cooling methods
in production EVs
Figure 2.8: Tesla's patented U-pass two-flow which runs in between rows of cells (Tesla
Model S Plaid Battery: Clever New Advancements Discovered, n.d.)
Figure 2.9: The BMW i3 battery pack (FIA Region I-Expert Study on Guidance and
Recommendations Regarding Electric Vehicle Propulsion Battery End-of-Life Policies,
n.d.)
Figure 2.10: The BMW i3 cooling plate (Kurmaev et al., 2020)
Figure 2.11: Nissan Ariya - coolant paths and inlets (NISSAN NISSAN TECHNICAL
REVIEW 2022 No. 88, 2022)
Figure 2.12: Audi e-Tron & Q8 e-Tron battery pack components (Audi Q8 E-Tron Audi
MediaCenter, n.d.)
Figure 2.13: Audi e-Tron & Q8 e-Tron cooling plate micro channels (<i>Audi Q8 E-Tron</i>
Audi MediaCenter, n.d.)
Figure 2.14: Porsche Taycan battery pack components (Porsche, 2023)

Figure 2.15: Porsche Taycan cooling plate components (Porsche, 2023)	20
Figure 2.16: Hyundai Group's Electric-Global Modular Platform (E-GMP)	20
Figure 2.17: Lucid Air battery pack (<i>Lucid Air</i> <i>Performance</i> , n.d.)	22
Figure 3.1: Digatron cycler (left) and Envirotronics thermal chamber (right)	25
Figure 3.2: AVL E-Storage.	26
Figure 3.3: Tenney TC20 thermal chamber	26
Figure 3.4: Polyscience 1200 W liquid chiller	27
Figure 3.5: Cell characterisation test setup inside chamber	28
Figure 3.6: Cell 1 tab separated from the rest of the module	28
Figure 3.7: A Porsche Taycan battery module	29
Figure 3.8: Exploded view of Porsche Taycan battery module	30
Figure 3.9: Module test setup inside chamber (without fire blanket)	31
Figure 3.10: Thermocouples on plastic inserts	32
Figure 3.11: Thermocouples on inserts inside the battery module	32
Figure 3.12: Cooling channel within the selected cooling plate	32
Figure 3.13: Placement of cooling plates showing inlets and outlets	33
Figure 3.14: Discharge capacity at different temperatures	36
Figure 3.15: Open circuit voltage at different temperatures	36
Figure 3.16: Terminal voltage and discharge resistance versus capacity discharge	ged for
1C at different temperatures	37
Figure 3.17: Fast charging power profile from the Porsche Taycan scaled down	to the
module with current and state of charge	38
Figure 3.18: Voltage and current vs SOC for the different charging rates	38
Figure 3.19: State of charge at transition to constant voltage charging	39

Figure 3.20: Time to reach 80% SOC at different C-rates	39
Figure 3.21: Ah charged into the module during fast charge with the Porsche Ta	aycan
power profile, assuming a module capacity of 124.35 Ah	40
Figure 3.22: Charging efficiency of the Porsche Taycan module	41
Figure 3.23: Charging loss scaled to the 93.4 kWh pack for the different charging	rates
	41
Figure 3.24: Thermocouple placement on the cell surface inside the module	42
Figure 3.25: Temperatures on the cell surface and T1 for the different charging ra	tes 42
Figure 3.26: Temperature distribution across the cell surface for the different cha	ırging
rates	43
Figure 3.27: Sample 60s of current during 1.5C constant power loss test	44
Figure 3.28: Accumulated cycler energy for 1.5C constant power loss test	44
Figure 3.29: Temperatures at A1 for each C-rate and cell loss	45
Figure 3.30: Temperature rise versus power loss for each C-rate	45
Figure 4.1: Illustration of the constant current-constant voltage protocol	50
Figure 4.2: Illustration of a four-step multistage constant current charging protoco	ol . 51
Figure 4.3: Illustration of the boost charging protocol	52
Figure 4.4: Zoomed-in illustration of pulse charging	53
Figure 5.1: Thevenin equivalent circuit for a with n number of parallel RC branch	ies 57
Figure 5.2: Parameter optimisation on the HPPC data at 25°C	60
Figure 5.3: R0 at 25°C	60
Figure 5.4: R1 at 25°C	61
Figure 5.5: tau1 at 25°C	61
Figure 5.6: R2 at 25°C	61

Figure 5.7: tau2 at 25°C
Figure 5.8: Current profile for the US06 drive cycle
Figure 5.9: Measured and modelled voltage profile for the US06 drive cycle
Figure 5.10: Thermal model electrical equivalent circuit
Figure 5.11: Fitted constant power loss test temperature for 1.5C using $Cth = 850 \text{J/kg}^{\circ}\text{C}$
66
Figure 5.12: Simulink model of the simplified electrical equivalent circuit thermal
model
Figure 5.13: The combined electrothermal model
Figure 5.14: Current profile of the Porsche Taycan fast-charging profile
Figure 5.15: Battery module state of charge for the Porsche Taycan fast-charging profile
Figure 5.16: Estimated and measured module voltage during the fast charge 69
Figure 5.17: Estimated and measured module temperature during the fast charge 69
Figure 5.18: Measured voltage used for temperature prediction
Figure 5.19: Estimated temperature with a lower error of 0.23°C at maximum when
model uses measured voltage
Figure 6.1: Outline of the fast-charging profile variation 1 – simple ramped step 74
Figure 6.2: Outline of the fast-charging profile variation 2 – ramped step with initial
step current
Figure 6.3: Peak temperature vs charging time for both options of the simple ramped
step profile variation
Figure 6.4: Simulated fastest charging simple ramped step profile (from the 375 A
option) compared to the simulated Taycan profile

Figure 6.5: Simulated lowest temperature from simple ramped step profile (from the
400 A option) compared to the simulated Taycan profile
Figure 6.6: Simulated simple ramped step profile (375 A Option) with the same charge
time (22.4 minutes) as the Taycan profile compared to the simulated Taycan profile 86
Figure 6.7: Simulated simple ramped step profile (400 A Option) with the same charge
time (22.43 minutes) as the Taycan profile compared to the simulated Taycan profile
86
Figure 6.8: Peak temperature vs charging time for the five options of the ramped step
with initial step current profile variation
Figure 6.9: Simulated fastest charging (20.8 minutes) ramped step with initial step
current profile (from the 358 A option) compared to the simulated Taycan profile 89
Figure 6.10: Simulated lowest temperature ramped step with initial step current profile
(from the 283 A option) 20.8 minutes
Figure 7.1: First profile selected for experimental verification with modelled peak
temperature less than 60°C
Figure 7.2: Modelled and measured data for the first selected profile with peak
temperature less than 60°C
Figure 7.3: Cell surface temperature distribution when Tcell is maximum for the
selected 24-minute profile
Figure 7.4: Temperature at A1 (hottest spot), E3 (coolest spot), and the inlet coolant
temperature
Figure 7.5: Updated temperature limit at 62°C showing the updated selected fast-
charging profile for the simple ramped step profile variation 97

Figure 7.6: Modelled and measured data for the fastest charging profile within
constraints
Figure 7.7: Comparison of the fastest charging profile within constraints with the
Taycan profile
Figure 7.8: Cell surface temperature distribution when <i>Tcell</i> is maximum for the fastest
22-minute profile within constraints 99
Figure B.1: Simulated performance of the ramped step with initial 219 A step current
profile for 80% charge time of 22.4 minutes compared to the simulated Taycan profile
Figure B.2: Simulated performance of the ramped step with initial 283 A step current
profile for 80% charge time of 22.4 minutes compared to the simulated Taycan profile
Figure B.3: Simulated performance of the ramped step with initial 358 A step current
profile for 80% charge time of 22.4 minutes compared to the simulated Taycan profile
Figure B.4: Simulated performance of the ramped step with initial 400 A step current
profile for 80% charge time of 22.4 minutes compared to the simulated Taycan profile
Figure B.5: Simulated performance of the ramped step with initial 500 A step current
profile for 80% charge time of 24.2 minutes

List of Tables

Table 2.1: Qualitative comparison of the four different cooling media
Table 2.2: EVs with air-cooled battery packs
Table 2.3: EVs with liquid-cooled battery packs
Table 2.4: Four types of edge-cooling architectures16
Table 3.1: Characterisation test procedures performed at test temperatures of -20, -10,
0, 10, 25 and 40°C
Table 3.2: Dimensions and properties of the cooling system components
Table 3.3. Test conditions for the Taycan module
Table 3.4: Module charging test procedure
Table 3.5: Constant power loss test procedure
Table 3.6: Constant power loss tests
Table 6.1: Durations for each step height for profile variation 1, 375 A Option 75
Table 6.2: Sample of 15 generated duration combinations for the 375 A option of the
simple ramped step profile
Table 6.3: Durations for each step height for variation 1, 400 A Option
Table 6.4: Sample of 15 generated duration combinations for profile variation 1, 400 A
Option
Table 6.5: Initial step current magnitudes and durations for variation 2 of the fast-
charging profile
Table 6.6: Durations for each ramped step height after initial step current to 10% SOC
81

Table 6.7: Estimated maximum temperature from electrothermal model and
approximated actual temperature for each initial step current option with the same 22.4-
minute charging time as the Taycan
Table 7.1: Selected fast-charging profile verification test procedure
Table A.1: Sample of 15 generated duration combinations for the ramped step with
initial step current profile (219 A option)
Table A.2: Sample of 15 generated duration combinations for the ramped step with
initial step current profile (283 A option)
Table A.3: Sample of 15 generated duration combinations for the ramped step with
initial step current profile (358 A option)
Table A.4: Sample of 15 generated duration combinations for the ramped step with
initial step current profile (400 A option)
Table A.5: Sample of 15 generated duration combinations for the ramped step with
initial step current profile (500 A option)

List of Abbreviations and Symbols

BC Boost Charging

BEV Battery Electric Vehicle

BMS Battery Management System

BTMS Battery Thermal Management System

CC Constant Current

CCCV Constant Current-Constant Voltage

CV Constant Voltage

DC Direct Current

ECM Equivalent Circuit Model

E-GMP Electric-Global Modular Platform

EV Electric Vehicle

FFPC Fixed Frequency Pulse Charging

ICE Internal Combustion Engine

KiBaM Kinetic Battery Model

LFP Lithium Iron Phosphate

LIB Lithium-Ion Battery

MCCC Multistage Constant Current Charging

NMC Nickel Manganese Cobalt

OCV Open-Circuit Voltage

PC Pulse Charging

PCM Phase Change Material

RC Resistor-Capacitor

SOC State of Charge

SOH State of Health

VFPCS Variable Frequency Pulse Charge System

Declaration of Academic Achievement

I hereby declare that I am the sole author of this master's thesis.

The content in Chapter 2 is adapted from the SAE WCX 2024 conference paper:

Uwalaka, L. I., Yao, Q., Kollmeyer, P., & Emadi, A. (2024). Review of Production Electric Vehicle Battery Thermal Management Systems and Experimental Testing of a Production Battery Module. *SAE Technical Papers*. https://doi.org/10.4271/2024-01-2672

The content in Chapter 3 is adapted from the ITEC 2024 conference paper:

Uwalaka, L., Yao, Q., Duque, J., Kollmeyer, P., & Emadi, A. (2024). Experimental Performance Analysis of LG E-66 Cells from a Fast-Charging Porsche Taycan Battery Module. 2024 IEEE Transportation Electrification Conference and Expo (ITEC), 1–6. https://doi.org/10.1109/ITEC60657.2024.10599015

The major contributions to this work were performed by the first author; Lucia Uwalaka – literature review, design and execution of the experiment, discussion and conclusions. Dr. Phillip J. Kollmeyer provided the research guidance, experimental apparatus, technical support, suggestions, and revisions. Josimar Duque and Qi Yao also provided support with the setup and execution of experiments. The controller which regulates the temperature under the module to 30°C was designed by Qi Yao. Dr. Ali Emadi supervised the research work.

1 Introduction

1.1 Background and Motivation

Electric vehicle (EV) battery technology has witnessed substantial advancements, particularly in lithium-ion battery systems (Duan et al., 2020; Miao et al., 2019) which form the backbone of modern EVs due to their high energy density and rechargeability (Cano et al., 2018; Hou et al., 2020). However, unlike conventional gasoline vehicles which can be refuelled within minutes, and despite the accelerated advancements in EV technology to make them a stronger competitor against the conventional internal combustion engine (ICE) vehicles, there are still barriers to EV adoption. One of the biggest challenges is the charging time and infrastructure – EVs have long charging time requirements which, in turn, influences driving range, and therefore, also impacts range anxiety (Michael et al., 2022; Mpoi et al., 2023).

Fast charging is a potential solution for this, but it often poses additional problems related to battery degradation, including increased internal resistance, capacity loss, and thermal management issues. According to (Kumar Thakur et al., 2023). Although charging stations are now capable of higher power outputs, EVs have limitations on the current or voltage they can accept, as the increased temperature rise and temperature gradient during fast charging can influence battery performance. Many existing studies have investigated the use of lithium-ion batteries in automotive applications, focusing on how different charging protocols influence degradation mechanisms and related safety considerations (Lu et al., 2019; Tanim et al., 2018; Tomaszewska et al., 2019).

Of the different power sources used in EVs, the lithium-ion battery is the most common due to its high specific energy, high energy density, long service life, low self-discharge, technical maturity, and environmental friendliness (Cano et al., 2018; Ghaeminezhad et al., 2023; Hou et al., 2020). However, the operation of lithium-ion batteries is limited by temperature, which can accelerate or decelerate the chemical reactions in the battery (Vidal et al., 2019). Extreme low temperatures lead to reduced usable battery capacity and power capability, as well as dendrite formation or lithium plating during charging, which could cause an internal short, a major safety issue (X. Zhang et al., 2022). Extreme high temperatures impact the lifespan of the battery, speed up the capacity degradation, increase the rate of self-discharge (Bandhauer et al., 2011) and pose the safety concern of thermal runaway. Because of the significant effects of temperature on battery operation, this work is based on the design of the fast-charging profile using battery surface temperature estimation.

The case study for the design and verification process in this thesis is the Porsche Taycan module. This is because the Porsche Taycan, with an 800 V architecture that reduces the charging current required, was the first EV which could charge at up to 270 kW (Porsche, 2023). Finally, this work does not include the impacts of fast charging on the battery state of health, as the only focus is the design of a faster, more efficient charging current profile.

1.2 Thesis Contributions

The development and testing of the fast-charging profile, as well as the simplified thermal model combined with the equivalent circuit model, used for profile verification are the most significant research contributions of this work. The main contribution of

this thesis is the development of a method to reduce the 5 to 80% charging time of 22.4 minutes for the Porsche Taycan battery module as obtained experimentally on a Porsche Taycan battery module, by 3% while ensuring that the battery surface temperature never exceeds 60°C in the process, and even achieving a lower peak cell surface temperature. This method also includes the additional constraint of employing coolant flow rates and temperatures which are typical in production EVs, scaled down to the module level.

While there are several studies on the different fast-charging protocols, there is not much work available on a specific application such as this, which focuses on the LG E-66 cells in the Porsche Taycan. This work provides experimental data which includes the cell surface temperatures inside an actual battery module obtained from the Porsche Taycan EV. Other works on the module level usually are systems designed by the researchers, not the manufacturers, which may not necessarily reflect what is obtainable in production EVs. So, the temperature spread across the cell surface in the battery module from an actual EV is usually unknown. This is addressed using thermocouples placed on the cell surface in the module.

This thesis also contributes a compilation of a thorough review on the battery thermal management systems (BTMS) in up to fifty production EVs, with information obtained from multiple sources available online.

1.3 Thesis Outline

The aim of this thesis is to create a fast-charging profile for the Porsche Taycan battery module. The process of achieving this is organised into seven chapters. The motivation for this work and the research contributions are stated here in Chapter 1.

Chapter 2 gives a comprehensive review of battery thermal management systems (BTMS) in fast-charging EVs. This is important to understand the state-of-the-art in fast-charging vehicles and guide the choice and specifications of the BTMS in the designed system.

In Chapter 3, a performance analysis of the LG E-66 cells inside the Porsche Taycan battery module is presented. This includes characterisation done on a single cell tested while still within, but separated from other cells in the battery module, as well as different charging tests done on another separate module where the cell surface was instrumented with thermocouples. Constant power loss tests were also performed on the module to assess the performance of the selected cooling system at our disposal. The data from this analysis is instrumental in creating an accurate model for the Porsche Taycan battery.

The fast-charging protocols used in lithium-ion batteries are then presented in **Chapter** 4 to give an overview of the different possible methods discussed in literature to address the fast-charging challenge, and to serve as a guide for the designed fast-charging profile.

In **Chapter 5**, the process of creating the simplified thermal model and equivalent circuit model which were combined into an electrothermal model for the Porsche Taycan battery module is explained in detail. The development of these models is necessary to feed in the designed fast-charging profile and observe its simulated performance, thereby determining feasibility before pursuing experimental verification.

The process of developing this fast-charging profile considering the required constraints and conditions is then presented in **Chapter 6**. The simulated performance of the different profiles obtained is also compared to the Porsche Taycan in this chapter.

Finally, the experimental verification of the selected fast-charging profiles is performed in **Chapter 7** to ensure the designed profile also gives the desired results in application. Experimental results are also presented.

Chapter 8 gives a summary of the work done in this thesis, and a comparison of the experimental results compared to the modelled results. Potential areas for further research in future work are also suggested in this chapter.

2 Battery Thermal Management Systems in Fast-Charging EVs

Battery thermal management systems (BTMS) are used to maintain batteries at their optimal temperature range. A good BTMS should keep temperature variations between cells small, while also ensuring that the cells are kept within their optimal operating range (Akbarzadeh et al., 2021). Battery cooling systems are usually classified based on the control method of the system and the cooling medium. Based on the control method, BTMS could be active, passive or a combination of these two known as hybrid, as described in (Akbarzadeh et al., 2021; Ghaeminezhad et al., 2023; Najafi Khaboshan et al., 2023; Rajan et al., 2022). According to these sources, active methods such as forced air or liquid flow using a fan, blower or pump require an external power source for control, while passive methods such as natural air convection, heat pipes and phase change materials (PCMs) do not require any power source for control of the cooling medium. Active methods are more complicated and reduce the overall efficiency of the system because they consume power from external sources, but they are more effective than passive methods (Akbarzadeh et al., 2021; Rajan et al., 2022). A detailed comparison of the advantages and disadvantages of the different active and passive cooling methods is given in (Ghaeminezhad et al., 2023).

2.1 Classes of Battery Thermal Management Systems

The four main cooling media which will be discussed in this section are air, liquid, PCMs and heat pipes (Ghalkhani & Habibi, 2023; Peng et al., 2017).

2.1.1 Air-Cooling

In air cooled systems, the air either flows freely through the battery pack by means of natural convection in a passive system, or air is forced through by means of a fan or air blower in an active system. Air cooled systems are known to be simple, light, low cost and easy to maintain (Akbarzadeh et al., 2021; Wang et al., 2018), which gives air-cooled systems an edge over other media. However, the main disadvantage of these systems is the low heat capacity and thermal conductivity of air (Akbarzadeh et al., 2021). Table shows a qualitative comparison of the four different cooling media considering the overall cooling system, where + represents the least and ++++ represents the highest value.

Table 2.1: Qualitative comparison of the four different cooling media

Criteria	Air	Liquid	PCMs	Heat
	Cooling	Cooling		Pipes
Cost	++	++++	+	+++
Complexity	+	+++	++	++++
Heat removal capability	++	+++	+	++++
Volume	+	++++	++	+++
Mass	++++	+++	++	++

2.1.2 Liquid Cooling

Compared to air cooling, liquid cooling is more effective due to the higher thermal conductivity and heat capacity of liquids, but also more complex, heavy, and expensive (Akbarzadeh et al., 2021; Wang et al., 2018). Liquid cooling can be direct, where the

cells are immersed directly in the cooling liquid (usually dielectric), or indirect, where the liquid runs through a cooling plate separate from the cells. Direct or immersive liquid cooling has been found to conduct heat away from the cells very effectively, but uniformly directing coolant flow around the immersed cells and preventing leaks adds to the challenge of designing immersive cooling systems.

Two forms of indirect liquid cooling have been researched extensively – edge cooling, where the cooling plate is placed on the edge of the modules; and intercell cooling, where the cooling plate is placed in between the cells. Additionally, various studies have been performed on the influence of different coolant channel paths on the performance of the indirect liquid cooling system performance. An analysis of the performance of four liquid cooling plates which have different coolant paths for electronic equipment, shown in Figure (Farhan et al., 2022) concludes that the Distributor-I channel configuration which has parallel paths is the most efficient design because of the uniform flow distribution, location of hot spots, and the low pressure drop which reduces the power needed to pump the coolant.

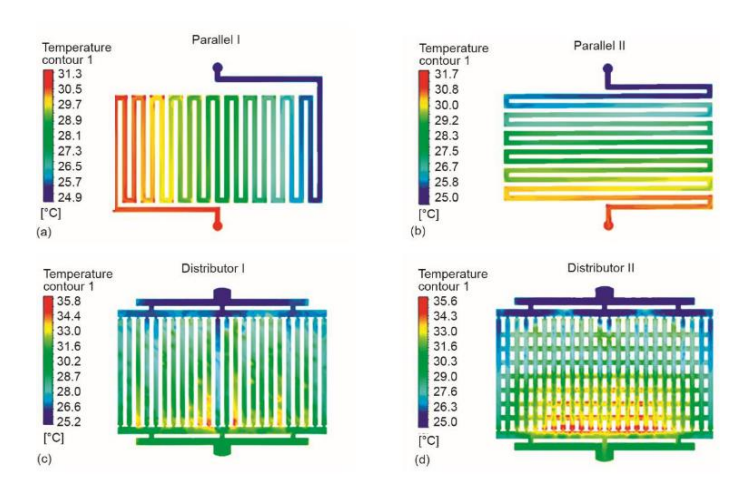


Figure 2.1: Cooling channel paths studied in (Farhan et al., 2022)

The study of (Li et al., 2022) shown in Figure evaluates the effect of channel design for six cooling plates with two layouts: A - at the bottom of the battery module or B - on both sides of the battery module. The coolant channels studied include single channel (I), multiple small channels (II), and S-shaped channel (III) shown in Figure, scaled to cover the length on either the bottom or the sides of the module. Design B-II, the straight cooling channels on both sides of the module, was found to yield the best cooling performance in this study.

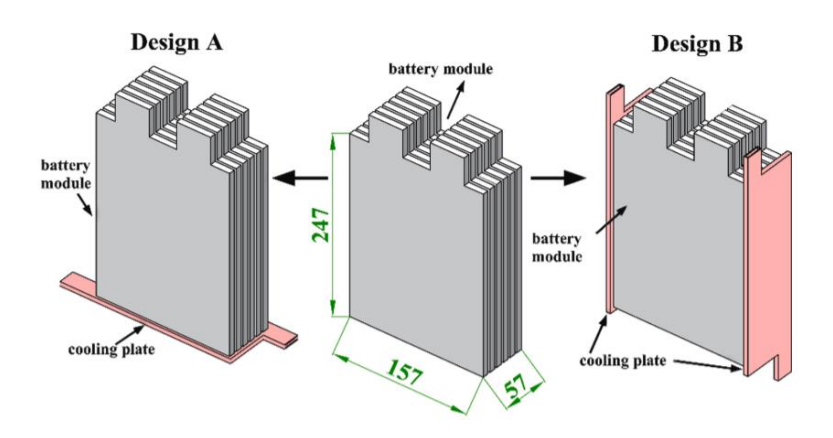


Figure 2.2: Cooling plate arrangements studied in (Li et al., 2022)

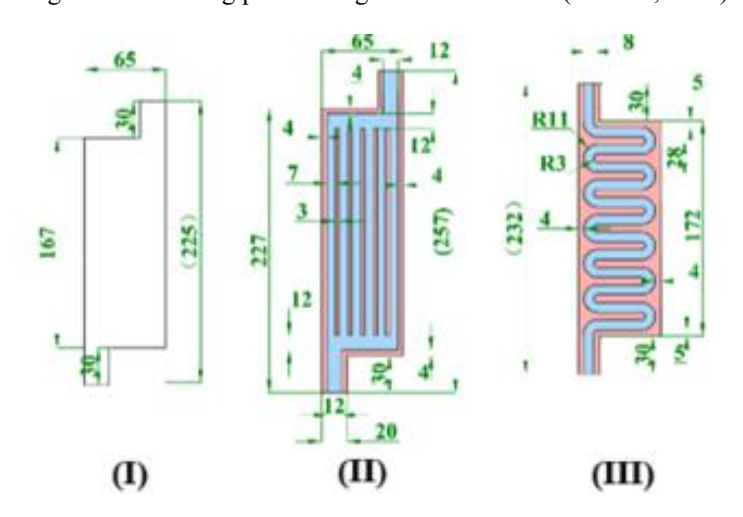


Figure 2.3: Cooling channel configuration I (single channel), II (small channels), and III (S-shaped) for the two arrangements in (Li et al., 2022)

In (Monika & Datta, 2022), six different cooling channel paths, shown in Figure 4 are considered for cooling a pouch-type battery on its largest surface. The serpentine and

hexagonal channels gave the best cooling performance of the six channels, while the pumpkin channel gave the least pressure drop and pumping power requirements. While this study provides insight into the performance of the different coolant pathways, the placement of the cooling plate may not be feasible in production because, cooling on the largest surface points towards intercell cooling for pouch cells, and this leads to a significant addition in volume.

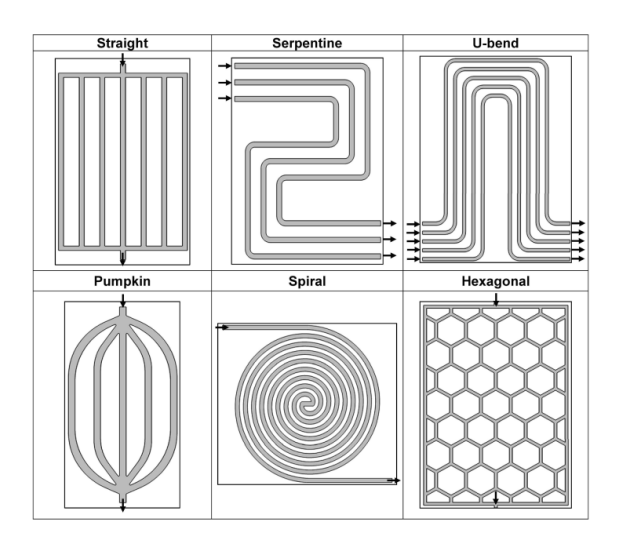


Figure 2.4: Cooling plate designs studied in (Monika & Datta, 2022)

2.1.3 Phase Change Materials (PCMs)

Phase Change Materials (PCMs) are materials that can absorb or release large amounts of latent heat during phase change, while maintaining a relatively constant temperature (Luo et al., 2022). This is a passive battery thermal management system because no external power source is required to control the operation of the PCM. PCMs store the heat generated by the batteries in the thermal mass of the PCM until the phase transition temperature, at which heat, referred to as latent heat, gets stored in the phase change process of the material. The design of the material determines at what temperature the phase change will occur. As the material cools below the phase transition temperature,

the stored heat is released and the PCM returns to its initial state. Although the applications of PCMs are limited due to their shortcomings, such as poor thermal conductivity, electrical leakage current concerns, and low strength, researchers such as (Goli et al., 2014; Wu et al., 2016; X. Zhang et al., 2018) have developed some composite PCMs to overcome these shortcomings (C. Liu et al., 2020). In (Wazeer et al., 2022) the desirable characteristics of ideal PCMs are listed as high latent heat, high specific capacity and thermal conductivity, chemical stability, non-toxicity, and affordability. Additionally, the phase change temperature which is usually higher than the ambient temperature according to (Al-Hallaj & Selman, 2002) should also be ideal for the application. In (Wazeer et al., 2022) the properties of some of the PCMs available on the market today are described as well.

2.1.4 Heat Pipes

A heat pipe is a vacuum-sealed pipe which transports heat from one point to another through a working fluid (usually refrigerant). Heat applied to one end of the heat pipe called the evaporator is absorbed through the heat pipe wall by the working fluid which then vaporises. During the process, the vaporised working fluid moves to the cooler end of the heat pipe called the condenser where it condenses back to liquid, releasing the stored heat energy. Capillary action, or sometimes gravity, then moves the condensed working fluid back to the evaporator, where the process repeats itself (Weragoda et al., 2023). This study also states that some of the reasons for the limited commercialisation of heat pipes include the limitations during rapid heat fluctuations and adverse environmental conditions and performance under multiple heat loads. An in-depth review of heat pipe technologies is presented in (Bernagozzi et al., 2023).

2.2 Battery Cooling Architectures in Current Fast-Charging EVs

Publicly available data on the battery cooling methods for 51 fast charging vehicles was compiled. A spreadsheet summarizing the characteristics of each vehicle can be (Uwalaka & Kollmeyer, n.d.). The predominant cooling method for these production vehicles was found to be liquid edge cooling, and the cooling medium distribution is shown in Figure .

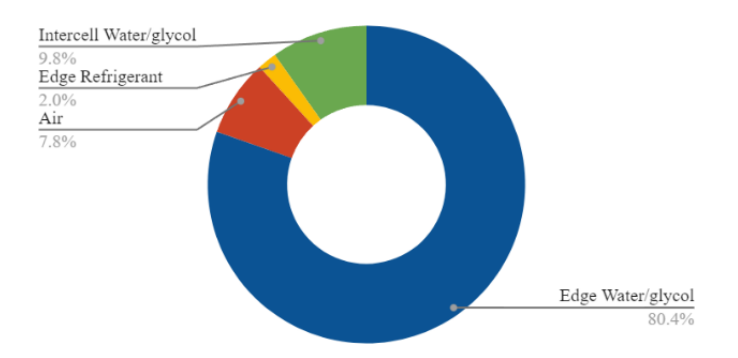


Figure 2.5: Cooling media distribution in production fast-charging EVs

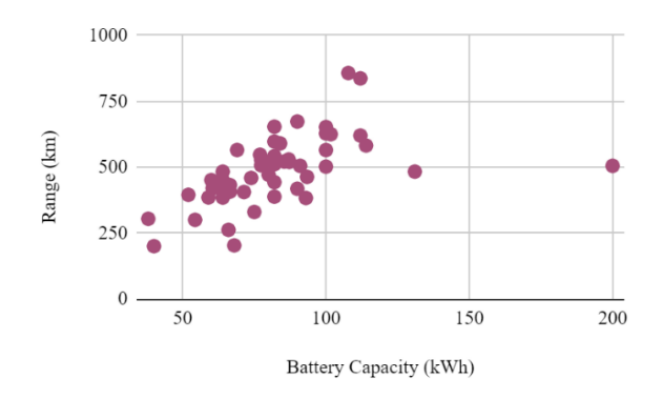


Figure 2.6: Range and capacity trends in production EVs

Figure 2.6 shows the relationship between the range and battery capacity of the EVs, while Figure shows the minimum and maximum direct current (DC) charging power for each cooling method.

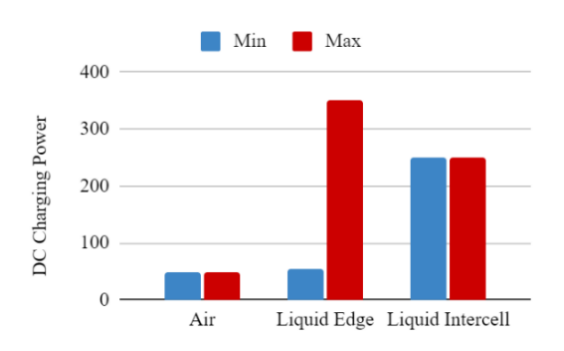


Figure 2.7: Minimum and maximum DC charging power for different cooling methods in production EVs

2.2.1 Air-Cooled Fast Charging Vehicles

Air cooling is the most affordable and lightweight method of the three media. It also offers the least complexity during installation because of the simplified components. However, its thermal conductivity is also the least of all three methods. This disadvantage of air-cooling limits, but does not eliminate, its applications in fast charging EVs in production. Four of the fast-charging EVs included in this paper are air-cooled, as shown in Table shows. These EVs air cooled battery packs have relatively low maximum charging power, around 50 kW and their charging time from 0 or 10% to 80% is quite slow as well, between 40 and 90 minutes.

Table 2.2: EVs with air-cooled battery packs

EVs with Air-	Battery Pack	Max DC Power	Charging Time
Cooled Battery	Capacity (kWh)	(kW)	
Packs			
Nissan Leaf e+	59	50	60 min
			(20 - 80%)
Nissan e-NV200	40	50	40 min
			(0 - 80%)
Lexus UX 300e	54.35	50	50 min
			(10 - 80%)

M.A.Sc. Thesis – L. Uwalaka; McMaster University – Electrical and Computer Engineering

Renault Zoe	52	50	65 min
			(0 - 80%)

2.2.2 Liquid-Cooled Fast Charging Vehicles

There is currently no EV in production which makes use of direct or immersive cooling, but there is substantial interest in academia and industry around this topic, so there is a high possibility of production applications being introduced in the near future. There is only one pure EV brand on the market with intercell cooling, and most of the other cooling architectures employ edge cooling. Table shows some fast-charging EVs with liquid-cooled battery packs.

Table 2.3: EVs with liquid-cooled battery packs

EVs with Liquid-	Battery Pack	Max DC Power	Charging Time
Cooled Battery	Capacity (kWh)	(kW)	
Packs			
Tesla Model Y	82	250	27 min
			(10 - 80%)
BMW i3	38	50	42 min
			(0 - 80%)
BMW i4	84	190	40 min
			(10 - 80%)
BMW iX	112	200	35 min
			(10 - 80%)
Audi e-Tron GT	93	270	22.5 min
			(0 - 80%)
Audi Q8 e-Tron	114	170	31 min
			(10 - 80%)
Nissan Ariya	130	130	30 min
			(10 – 80%)

M.A.Sc. Thesis – L. Uwalaka; McMaster University – Electrical and Computer Engineering

Hyundai Ioniq 5	77.4	350	36 min
			(0 - 80%)
Lucid Air	112	350	37 min
			(0 - 80%)
Porsche Taycan	93.4	270	22.5 min
			(0 - 80%)
Ford F-150	131	150	41 min
Lightning			(15 – 80%)
Ford Mustang	91	150	45 min
Mach-E			(10 - 80%)

2.2.2.1 Intercell Cooling

The only fast charging battery electric vehicles (BEVs) with intercell cooling today are Tesla EVs. The most recent design Tesla uses in their EVs today has several cooling channels running in between every other row of cells, to further reduce the temperature deviation between the cells in the pack. It uses their patented U-shaped coolant channel shown in Figure to achieve a more uniform temperature distribution. This cooling design is used in the Tesla Model S Plaid, and is believed to be used in all newer models such as the Tesla Model Y.



Figure 2.8: Tesla's patented U-pass two-flow which runs in between rows of cells (*Tesla Model S Plaid Battery: Clever New Advancements Discovered*, n.d.)

2.2.2.2 Edge Cooling

Most of the fast-charging EVs in production today use liquid edge cooling under either the entire battery pack or each module for battery thermal management. The edge cooling architectures found for the EVs in (Uwalaka & Kollmeyer, n.d.) can be classified into four main architectures - longitudinal, latitudinal, snake-like, and individual module - as shown in Table .

Table 2.4: Four types of edge-cooling architectures

Edge-Cooling Architecture		Description	
Longitudinal Edge-	The state of the s	Cooling channels run along the pack	
Cooling		from the front to the back of the vehicle	
Latitudinal Edge-		Cooling channels run across the pack	
Cooling		from one side to the other in the vehicle	
Snake-like Edge-		Single cooling channel runs in a snake-	
Cooling		like pattern under the entire battery	
		pack from front to back	
Individual Module		Each module has its own cooling	
Edge-Cooling		channel, inlet, and outlet	

1.1.1.1 Longitudinal Edge-Cooling

Vehicles with longitudinal cooling include the BMW i3 and Nissan Ariya. The BMW i3, whose battery pack and cooling plate are shown in Figure 2.9 and Figure 2.10

respectively, is the only production EV whose cooling medium is refrigerant, which has higher cooling rates compared to liquid glycol. The disadvantage of using refrigerant is that an additional component (heating strip) is required to warm up the batteries in lower temperature conditions.

Figure 2.11 shows the coolant paths and coolant inlet and outlet on the cooling plate in the Nissan Ariya, illustrating that coolant flows in opposite directions on opposite sides of the pack.

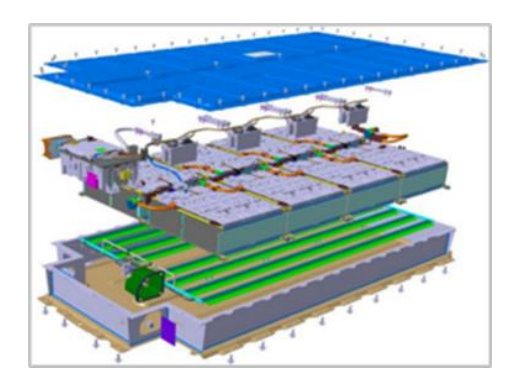


Figure 2.9: The BMW i3 battery pack (FIA Region I-Expert Study on Guidance and Recommendations Regarding Electric Vehicle Propulsion Battery End-of-Life Policies, n.d.)

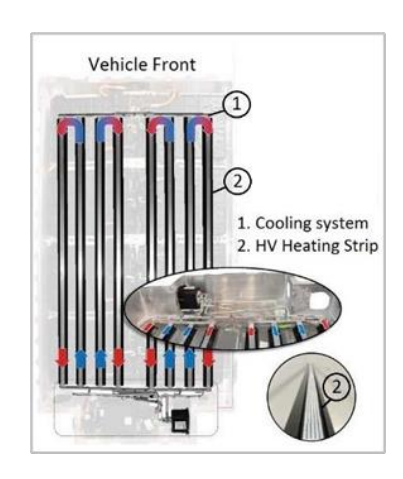


Figure 2.10: The BMW i3 cooling plate (Kurmaev et al., 2020)

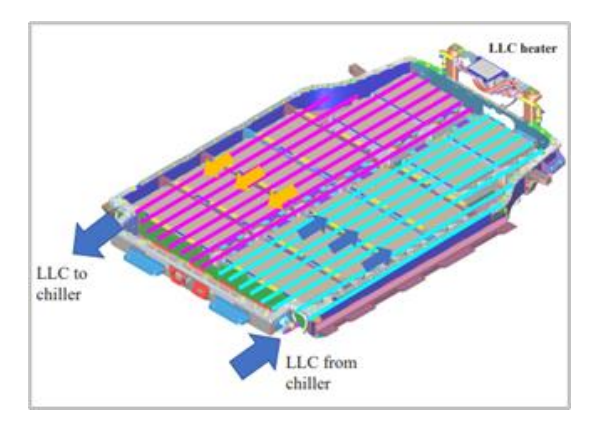


Figure 2.11: Nissan Ariya - coolant paths and inlets (NISSAN | NISSAN TECHNICAL REVIEW 2022 No. 88, 2022)

2.1.1.1.1 Latitudinal Edge-Cooling

Vehicles with latitudinal edge-cooling include the e-Tron and Q8 e-Tron from Audi which both have the same cooling architecture shown in the battery back in Figure . One unique feature of the packs, as shown in Figure , is that the wide cooling channel which runs under each module has smaller micro channels within it to increase the velocity. This is because, as the cooling channel divides into smaller microchannels, the total mass flow rate must remain constant. However, because the microchannels have reduced cross-sectional areas, the fluid within them must flow at higher velocities to maintain this constant mass flow rate.

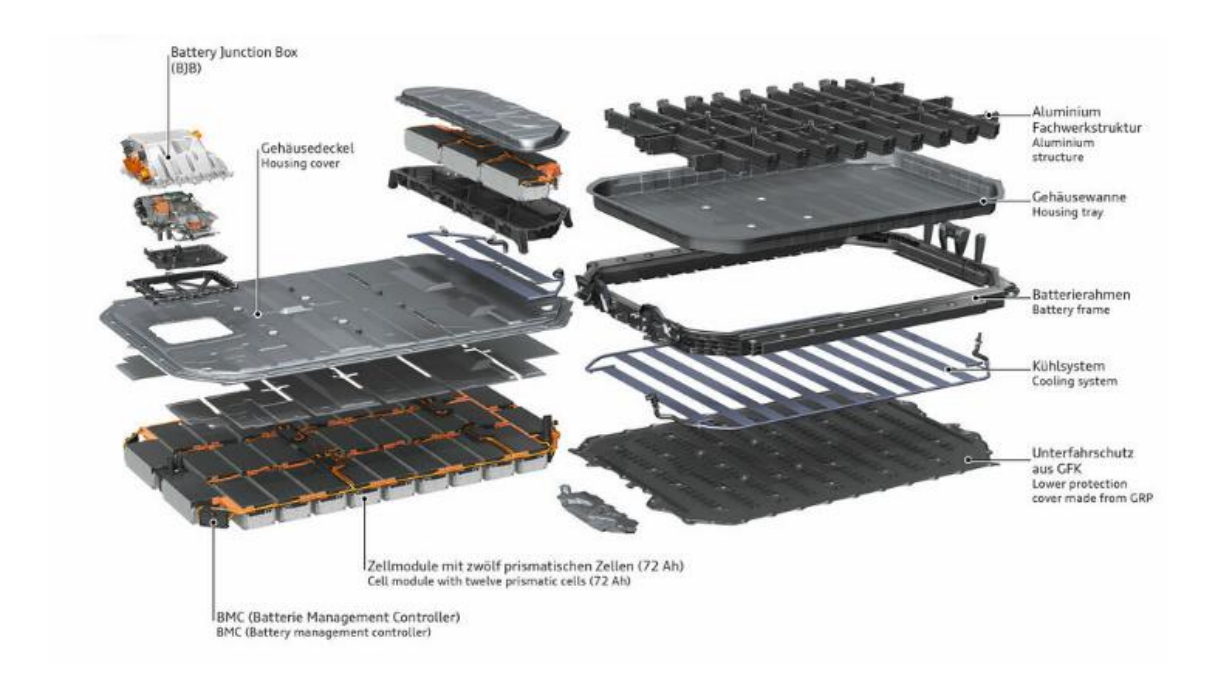


Figure 2.12: Audi e-Tron & Q8 e-Tron battery pack components (*Audi Q8 E-Tron | Audi MediaCenter*, n.d.)



Figure 2.13: Audi e-Tron & Q8 e-Tron cooling plate micro channels (*Audi Q8 E-Tron | Audi MediaCenter*, n.d.)

The Porsche Taycan, whose battery pack and cooling plate components are shown in Figure and Figure respectively, also falls under this category.

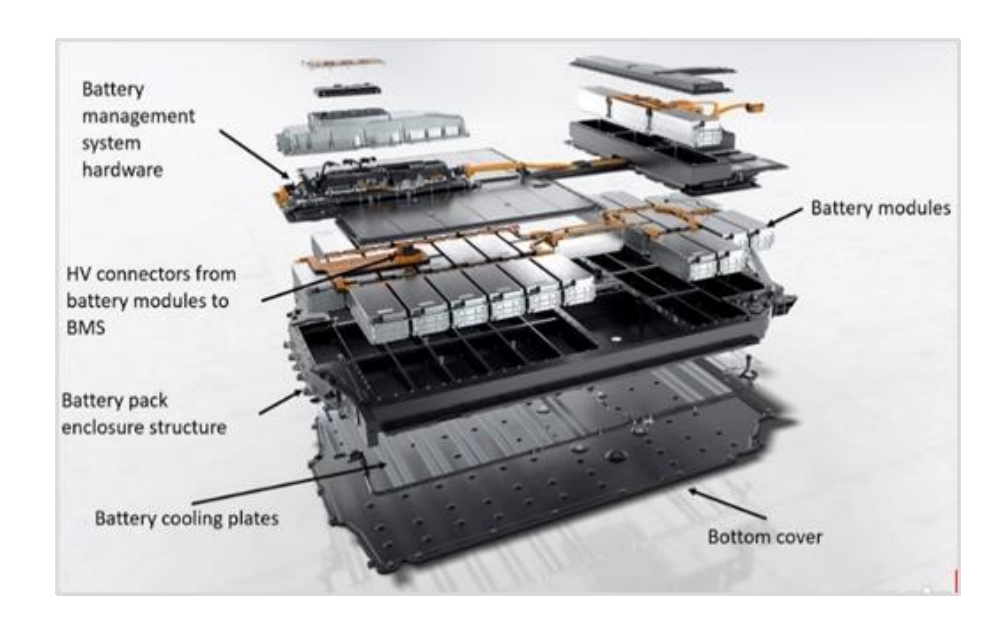


Figure 2.14: Porsche Taycan battery pack components (Porsche, 2023)

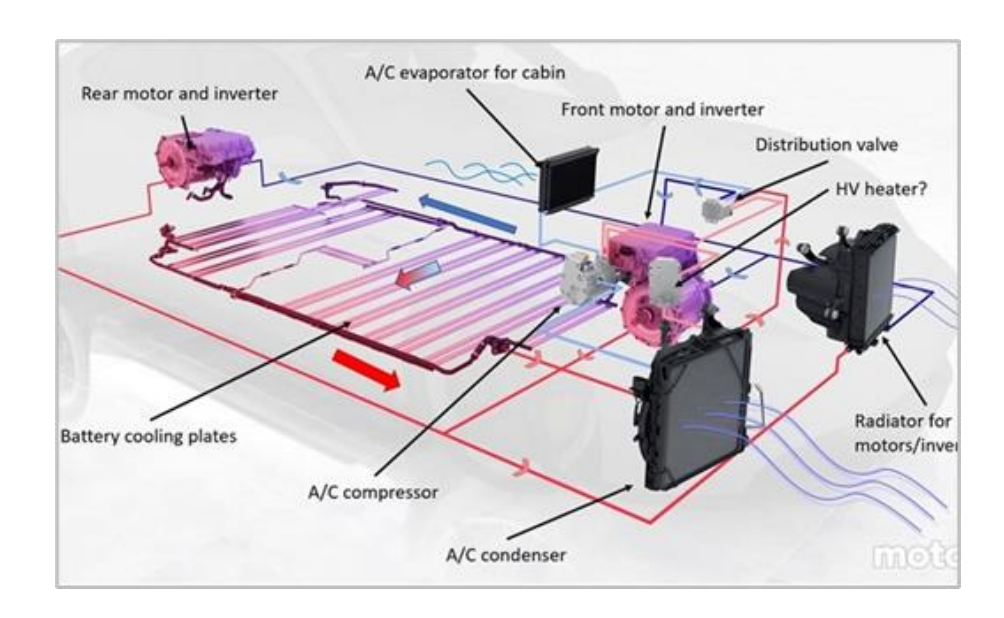


Figure 2.15: Porsche Taycan cooling plate components (Porsche, 2023)

3.1.1.1.1 Snake-Like Edge-Cooling

For the snake-like edge cooling architecture, Figure shows the Electric-Global Modular Platform (E-GMP) designed to be scalable for all Hyundai Group's EVs. It is currently in the Hyundai Ioniq 5, the KIA EV6, and possibly in the Hyundai Genesis. These three vehicles can charge from 10 to 80% in 18 minutes and are currently among the fastest charging EVs today.

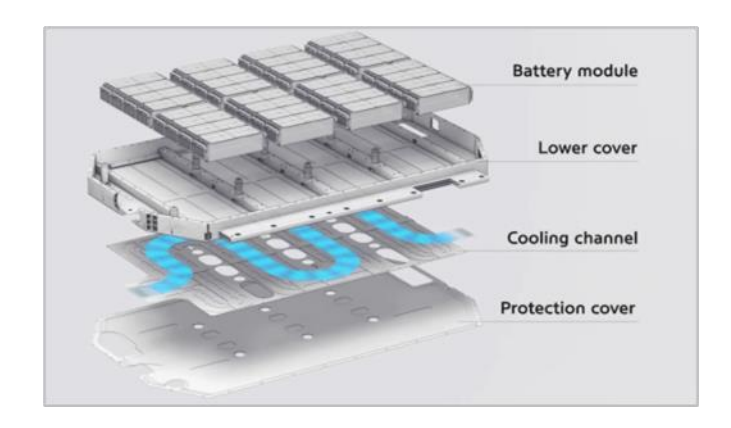


Figure 2.16: Hyundai Group's Electric-Global Modular Platform (E-GMP)

4.1.1.1 Individual Module Edge-Cooling

Vehicles with individual module edge-cooling include the Lucid Air, the BMW i4 and the BMW iX. The Lucid Air battery pack in Figure shows the cooling plates of the Lucid Air are on top of the modules, an uncommon arrangement in production EVs. Their reason for this is to have an additional layer of protection between the passengers and the battery pack in the event of a fire or thermal runaway. Additionally, their cooling plates are held together by dimples, unlike the cooling channels shown in most other EVs. While the dimples are meant to increase turbulence and hence improve thermal conductivity, the only other EV which has this feature among those covered in (Uwalaka & Kollmeyer, n.d.) is the Ford Mustang Mach-E. This could be because it is more difficult to control the flow rate of the coolant with this design, and the coolant can only be pumped at the maximum possible flow rate. However, the Lucid Air is currently the fastest charging vehicle in the world today, with a charging rate of up to 20 miles (32.2 km) per minute.



Figure 2.17: Lucid Air battery pack (*Lucid Air* | *Performance*, n.d.)

Other EVs with individual module cooling are the Ford F-150 Lightning and the Ford Mustang Mach-E whose cooling plates are discussed in teardowns by Munro and Associates (*F -150 Lightning Battery Pack Structure - YouTube*, n.d.; *Mach-E: Battery Tray and Battery Cell Features - YouTube*, n.d.).

2.3 Cooling Architecture for the Taycan Battery Module

This review has shown liquid edge cooling to be the predominant cooling architecture in EVs capable of fast charging. This is due to the higher thermal conductivity offered by liquid cooling as compared to air and other cooling media. Based on this, the cooling mechanism for the Taycan battery module studied in this thesis will also be liquid edge cooling. However, as the latitudinal cooling plate used in the Porsche Taycan was not readily available, a cooling plate with a snake-like cooling architecture was used for the thermal management of the Taycan battery module. However, the inlets for the cooling

system used are on both ends of the battery module, and the outlets are in the middle. Additionally, because this work focuses on just a single module and not a battery pack, the architecture used could be considered as a fusion of individual module cooling and snake-like cooling. More details will be presented in the next section.

3 Experimental Performance Analysis of LG E-

66 Cells from the Porsche Taycan Battery

Module

The Porsche Taycan is available in two battery pack sizes 79.2 kWh and 93.4 kWh, which have 28 and 33 modules, respectively. Each module in both variations consists of twelve cells in a six-series-two-parallel (6s2p) configuration. Since the Porsche Taycan uses the LG E-66 nickel-manganese-cobalt (NMC) cells, understanding their performance characteristics, especially during fast-charging scenarios is particularly important.

According to the information shared by Porsche with the public, the Porsche Taycan, with its 800 V architecture and 270 kW DC fast charging capability, achieves 5 – 80% state of charge (SOC) within 22.5 minutes. To better evaluate the battery storage system performance of the Taycan and explore ways to improve its fast-charging capability, a battery module, as well as a battery cell, taken from the Porsche Taycan EV was comprehensively tested.

The single LG E-66 cell was characterised at different temperatures, including -20, -10, 0, 10, 25, and 40°C, while the performance of a separate module comprising these cells is evaluated during different charging tests. The module was instrumented underneath with three thermocouples, and nine more on the cell surface within the actual module to monitor the thermal performance of the module during charging. A rescaled fast charge profile from the Porsche Taycan EV was also used to charge the module.

Constant power loss tests were performed on the battery module at 0.7C, 1.2C, and 1.5C to determine the thermal resistance and capacity of the selected cooling system. The characterization data presented is available on an open-access website (Uwalaka et al., n.d.), to support battery research.

3.1 Experimental Setup

Two battery testing platforms were used, one for testing the individual battery cell and one for testing the battery module. The single battery cell was tested using a Digatron battery cycler with five parallel-connected 75 A, 0 V to 5 V channels, which are rated for 0.1% accuracy. The cell was placed inside the Envirotronics ET8-2-1.5 thermal chamber, which has a capacity of 8 cubic feet, and a temperature accuracy of +/-1°C. The battery cycler and chamber, respectively, are shown in Figure .



Figure 3.1: Digatron cycler (left) and Envirotronics thermal chamber (right)

On another testing platform, the battery module, consisting of twelve cells in six-series and two-parallel configuration (6s2p) was tested with an AVL E-Storage battery cycler

shown in Figure , which can also serve as a battery emulator or a fast charger, and has a voltage range of 8-800 V, a current limit of 600 A, power limit of 160 kW, and an accuracy of $\pm 0.1\%$.



Figure 3.2: AVL E-Storage

The module was placed inside a Tenney TC20 thermal chamber shown in Figure , which has a capacity of 20 cubic feet, a temperature range of -68°C to 180°C, and a temperature accuracy of +/- 1°C.



Figure 3.3: Tenney TC20 thermal chamber

Figure shows the Polyscience LS51MX 1200 W chiller, with a temperature range of -20-40 °C, and a temperature accuracy of +/-0.25 °C, which was used to pump coolant through a cooling plate placed under the module.



Figure 3.4: Polyscience 1200 W liquid chiller

3.1.1 Single Cell Characterization: Setup and Experimental Procedure

In the cell characterization tests, the minimum and maximum voltage limits for the cell were set to 2.8 V and 4.2 V, respectively, corresponding to 0% and 100% SOC. The maximum voltage determines the transition from constant-current (CC) to constant-voltage (CV) charging. The setup for the cell characterization is shown in Figure . Characterization tests were performed at different temperatures on the first cell in the module, with its tab and bus bar carefully cut to separate it from the rest of the cells, as shown in Figure .



Figure 3.5: Cell characterisation test setup inside chamber



Figure 3.6: Cell 1 tab separated from the rest of the module

Before characterization at each temperature, a slow discharge at C/20 was performed at 40°C to establish a reference for the cell's capacity and track any aging. Table shows the characterization test procedures, where "test temperature" refers to the temperatures of interest: -20, -10, 0, 10, 25, and 40°C.

Table 3.1: Characterisation test procedures performed at test temperatures of -20, -10, 0, 10, 25 and 40°C

Test	Temperature	Description
C/20 Discharge	40°C	Measure cell capacity before testing at each temperature
C/3 Discharge	Test temperature	Measure cell capacity at the test temperature
HPPC	Test temperature	Four charge and four discharge pulse magnitudes at different SOCs
GITT	Test temperature	0.3C discharge to different SOCs with two-hour wait; process repeated for charge
C/20 Charge & Discharge	Test temperature	Obtain OCV at the test temperature
0.5C & 1C Discharge	Test temperature	Obtain terminal voltage and capacity

M.A.Sc. Thesis – L. Uwalaka; McMaster University – Electrical and Computer Engineering

Test	Temperature	Description
Drive Cycles	Test temperature	Fifteen drive cycles for testing and training of algorithms and models

3.1.2 Module-Level Testing: Setup and Experimental Procedure

Figure shows a Porsche Taycan battery module, and an exploded view of the module is shown in Figure . The twelve cells are grouped into three sets of four, separated by foam pads to allow for the expansion of the pouch cells.



Figure 3.7: A Porsche Taycan battery module

Because of the folded edges of the pouch cell, there is a solidified thermal paste, not shown in the exploded view, which was injected at the bottom of the module to increase thermal conductivity with the cooling plate underneath through the module casing.

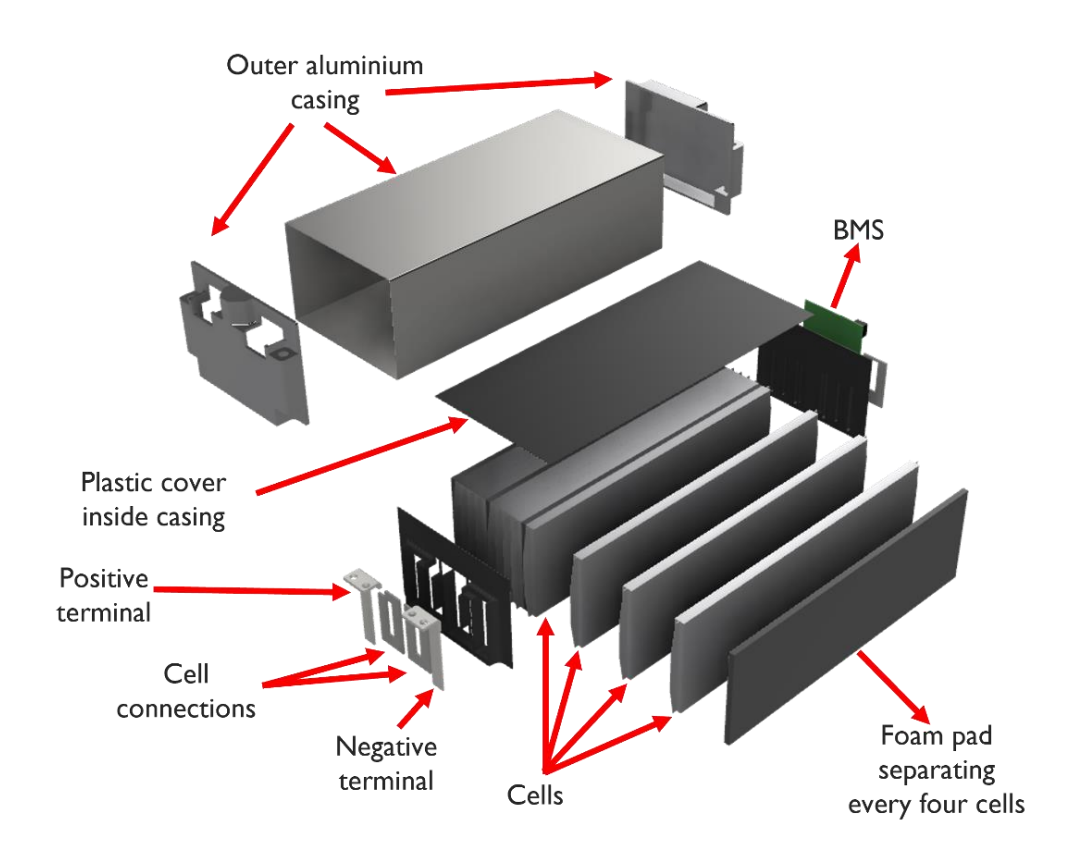


Figure 3.8: Exploded view of Porsche Taycan battery module

For the module tests, the minimum and maximum voltage limits for each cell were set to 2.8 V and 4.18 V, respectively. Charge tests on the module were performed using the multistage constant-current charging (MCCC) protocol, where the charging current is progressively reduced in steps each time the battery voltage reaches the maximum voltage limit, until the voltage limit is reached at a current threshold value. MCCC has been studied as one of the promising methods for fast charging lithium-ion batteries, as it is faster than constant-current constant-voltage (CCCV) charging and can prevent lithium deposition and increase cycle life (Khan et al., 2016; Mai et al., 2020; Makeen et al., 2022). Figure shows the battery module for module testing, which was instrumented to perform the charging tests and observe the thermal behaviour of the cells in the 6s2p configuration inside the module.

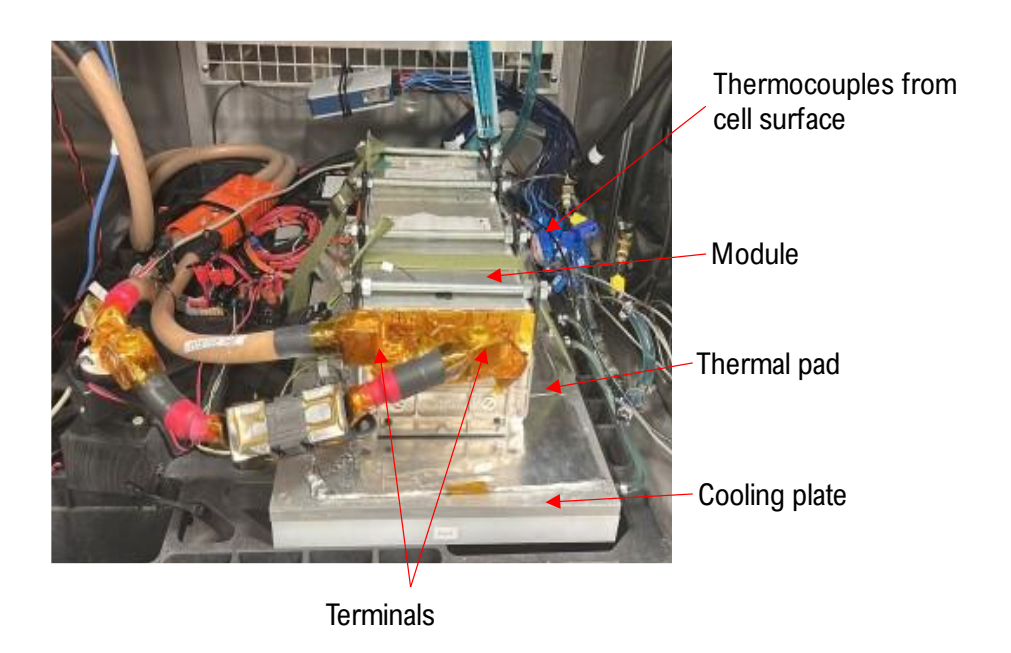
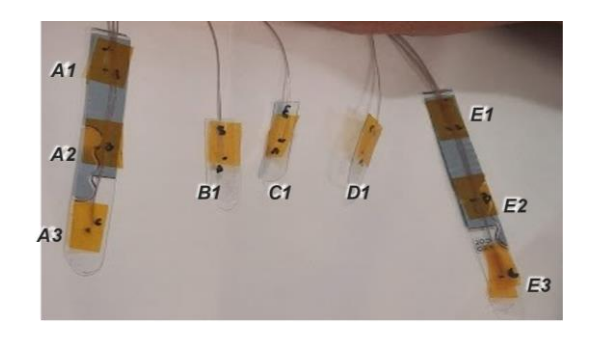


Figure 3.9: Module test setup inside chamber (without fire blanket)

During testing, the module was covered with a fire blanket to replicate an adiabatic system by minimising heat loss through convection in the chamber and ensure that basically all heat generated by the battery is exchanged through the coolant underneath the module. Additionally, the cell surface temperature was recorded at nine points using thermocouples which were taped to plastic inserts, as shown in Figure . These inserts were inserted in between cells 4 and 5, counting from the right, as shown in Figure . One more thermocouple, T1, also shown in Figure was placed at the position of one of the two stock temperature sensors from where the Taycan reads the module temperature in the actual Porsche Taycan EV.



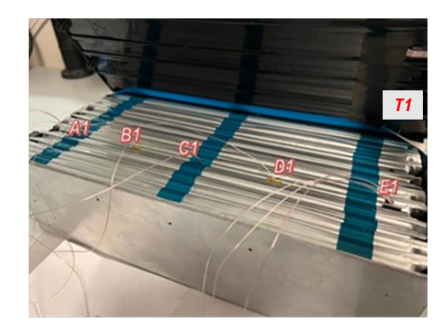


Figure 3.10: Thermocouples on plastic inserts

Figure 3.11: Thermocouples on inserts inside the battery module

The cooling system for the battery module testing setup is further detailed in Figure and Figure below. The former shows a view of the cooling channel in the cooling plate used, and the latter shows the placement of the module on the two cooling plates, with the coolant inlets marked in blue and the outlets in red.



Figure 3.12: Cooling channel within the selected cooling plate

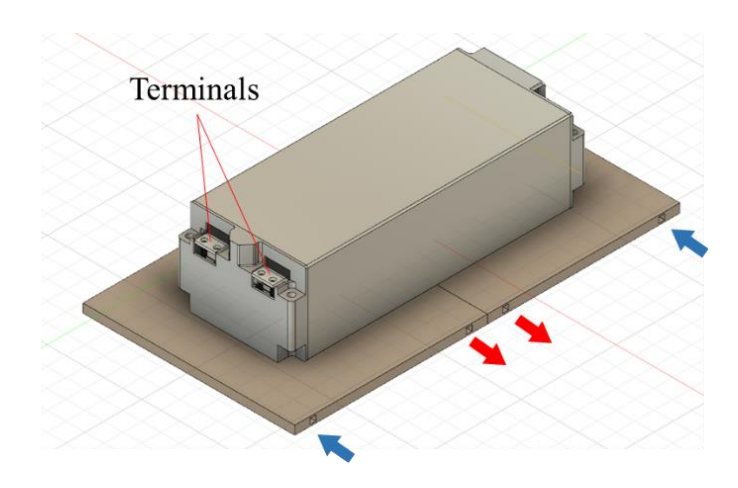


Figure 3.13: Placement of cooling plates showing inlets and outlets

The cooling plate comprises a top and a bottom component which are screwed together. The dimensions and properties of the cooling plate are as shown in Table, derived from (Zhao, 2021) who also made use of this cooling plate assembly. The thermal pad was purchased separately.

Table 3.2: Dimensions and properties of the cooling system components

Component	Material	Dimension	Density	Specific Heat	Thermal
		$L \times W \times H$	(kg/m^3)	Capacity	Conductivity
				$(J/kg \cdot K)$	$(W/m\cdot K)$
Cooling	Aluminium	11 × 10	2800	900	180
plate (top)	3003-Н4	\times 0.081 (in)	2800	900	100
Cooling	Aluminium	11 × 10			
plate	3003-H4	\times 0.375 (in)	2800	900	180
(bottom)	5005 111	7. 0.070 (iii)			
Thermal		228.6			
	Tflex B200	× 228.6	-	-	2
pad		× 4.83 (mm)			

The specific test conditions for the charging and constant power loss tests are summarised in Table . All tests on the module were performed with the ambient chamber

temperature set to 30°C. This is because, in the Porsche Taycan, the battery pack is preheated to 30°C before the fast charge is executed. Based on the assumption that this is the ideal temperature for maximising charge acceptance due to the increased reaction rates in the cell, all tests performed on the battery module were done with an ambient temperature of 30°C, letting the battery module soak for 1 to 2 hours, until all thermocouples on the cell surface inside the module were at 30°C. The chiller was also programmed to regulate the temperature under the module at 30°C for all tests by controlling the inlet coolant temperature.

Table 3.3. Test conditions for the Taycan module

Chamber setpoint	30°C
Initial coolant inlet temperature	30°C
Coolant	50/50 water/glycol mix
Coolant flow rate	1.75 l/min (split between the two parallel cooling plates)

Table shows the charging test procedure performed for the different charging rates as well as the multistage current steps. The same overall procedure was followed for the fast charge using the power profile from the Porsche Taycan obtained from (*Porsche Taycan 0 to 100% DC Fast Charge Test - YouTube*, n.d.) with the only difference being in step 3, where the obtained power profile was used instead of constant current to charge the battery.

Table 3.4: Module charging test procedure

Step	Action	Step End
1	Discharge at C/4	$V_{cell} < 2.8 V$

M.A.Sc. Thesis – L. Uwalaka; McMaster University – Electrical and Computer Engineering

Step	Action	Step End
2	Wait	1.5 hrs AND $T_{cell} \approx 30^{\circ}C$
	MCC Charge at C-rate	
	• 2C – 264A, 132A, 66A, 33A, 16.5A, 10A, 5A	
	• 1.5 C – 198A, 99A, 66A, 33A, 16.5A, 10A, 5A	V > 410 V
3	• 1C – 132A, 66A, 33A, 16.5A, 10A, 5A	$V_{cell} \ge 4.18 V$ at 5 A
	• 0.5 C – 66A, 33A, 16.5A, 10A, 5A	
	Fast Charge	
	• Rescaled fast charge power profile, as shown in Figure .	

Constant power loss tests were conducted at three different C-rates: 0.7C, 1.2C, and 1.5C. To avoid reaching voltage limits, the module was discharged to 70% SOC prior to the constant power loss tests. A square wave of the desired current value was applied to the module in 10-second pulses going from positive to negative, ensuring a net zero charge and a constant power loss. Table shows the constant power loss test procedure, which was run until the cells reached steady state temperature – about 2 hours.

Table 3.5: Constant power loss test procedure

Step	Action	Step End
1	Discharge at C/4	<i>SOC</i> ≈ 70%
2	Wait	1.5 hrs AND $T_{cell} \approx 30^{\circ}C$
3	CC Discharge at C-rate	10 s
4	CC Charge at C-rate	10 s

M.A.Sc. Thesis – L. Uwalaka; McMaster University – Electrical and Computer Engineering

Step	Action	Step End
5	Repeat steps 3 & 4	2 hrs AND T_{cell} at steady state

3.2 Cell Characterization and Module Performance Test Results

3.2.1 Cell Characterization Results

The cell discharge capacity, OCV, resistance, and terminal voltage at various temperatures obtained from the characterization tests are presented in Figure, Figure, and Figure respectively.

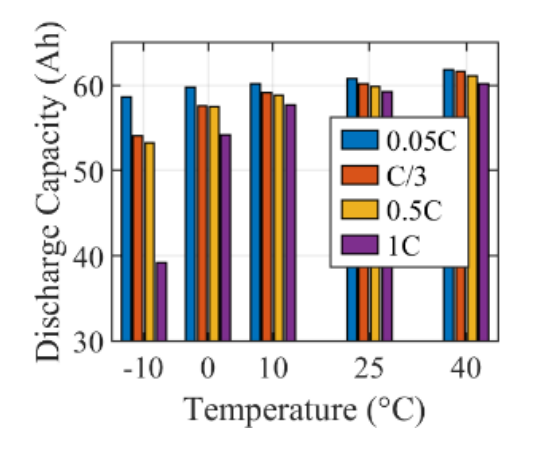


Figure 3.14: Discharge capacity at different temperatures

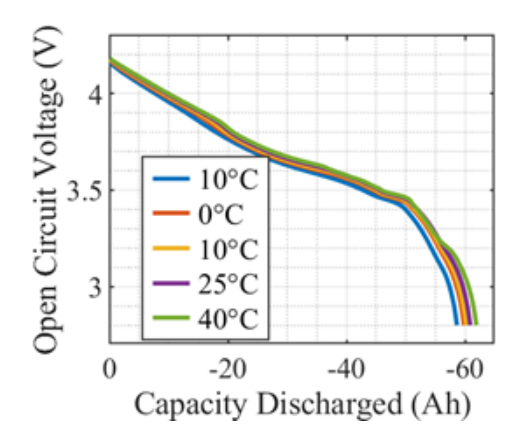


Figure 3.15: Open circuit voltage at different temperatures

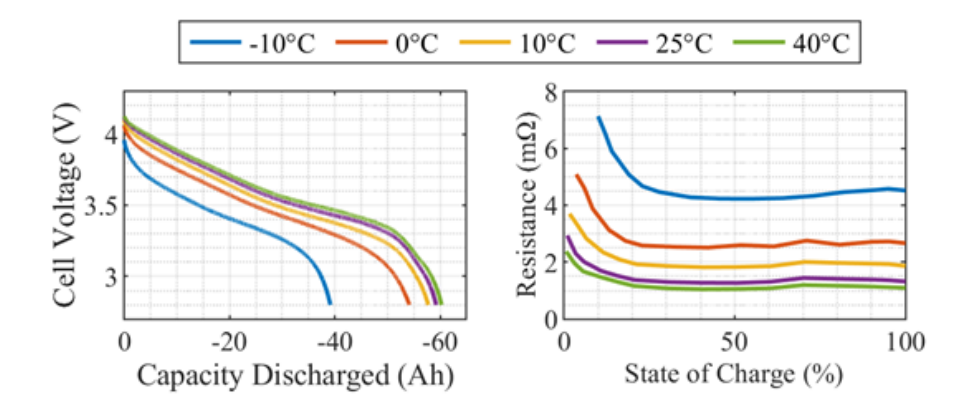


Figure 3.16: Terminal voltage and discharge resistance versus capacity discharged for 1C at different temperatures

The capacity of the cell, even at 40°C, is slightly lower than the expected value of 66 Ah. This can be attributed to the smaller voltage range used in these tests to protect the cell. Also, as expected, the discharge capacity significantly reduces as the temperature falls, especially with higher C-rates. The resistance also increases at lower temperatures, four times higher at -10°C, compared to the value at 40°C.

The complete data set for the characterization tests, including fifteen drive cycles performed at each temperature can be found on (Uwalaka et al., n.d.).

3.2.2 Module Test Results

3.2.2.1 Charging Test Results

Based on the C/4 discharge before each charge cycle, with a cell voltage range of 2.8 V to 4.18 V, the average capacity of the module used for the module tests is 111.79 Ah. This is the value with which the state of charge is calculated in Figure which shows the power profile from the Porsche Taycan scaled down to the module, as well as the SOC during the fast charge.

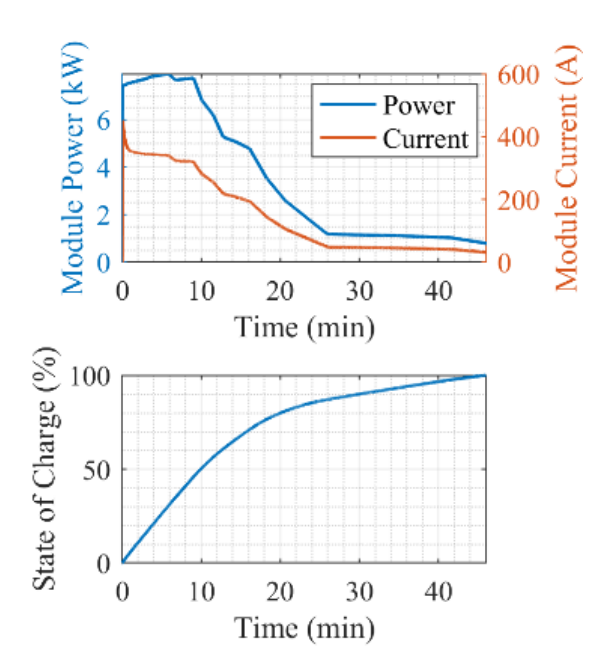


Figure 3.17: Fast charging power profile from the Porsche Taycan scaled down to the module with current and state of charge

The average cell voltage and current for the different charging C-rates are shown in Figure, while Figure shows the state of charge at the first current stepdown, when the cell voltage first reaches the upper limit at the maximum current of the charge cycle.

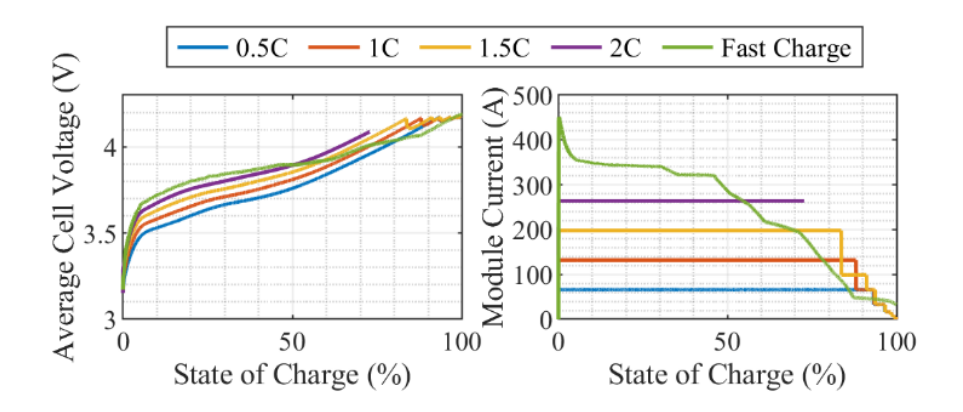
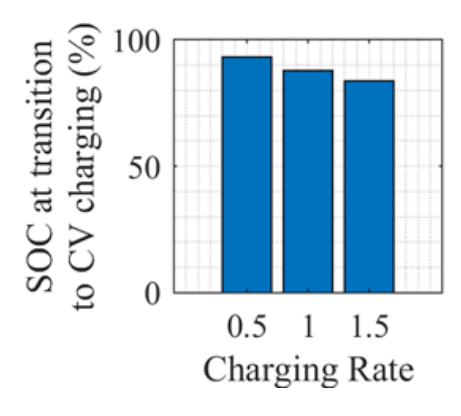


Figure 3.18: Voltage and current vs SOC for the different charging rates



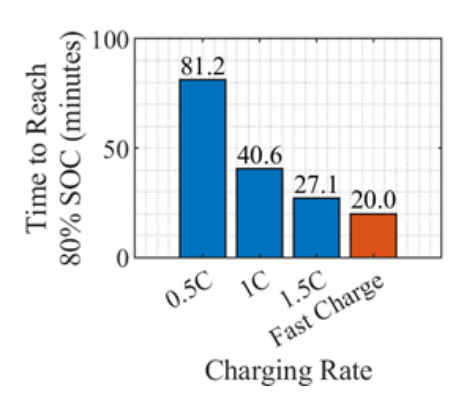


Figure 3.19: State of charge at transition to constant voltage charging

Figure 3.20: Time to reach 80% SOC at different C-rates

The time it takes to reach 80% SOC at each charge rate is in Figure above. It is important to note once again here that the capacity of the module differs from the expectation of 124.35 Ah when the cell capacity is doubled for the two parallel cell strings in the module. Because 1C was assumed to be 132 A for all module tests, this could be the reason for the discrepancy in the expected 1-hour duration for 1C tests, and hence influences the time it takes to charge up to 80% SOC.

When two times the measured cell capacity from the characterisation tests is used (124.35 Ah), the SOC of the module during the fast charge is as shown in Figure , and the time it takes to charge from 5 to 80% SOC, is 22.4 minutes, as opposed to 20 minutes obtained before. This is closer to the expected charging duration of 22.5 minutes advertised by Porsche, thereby validating the measured cell capacity from characterisation. This is also the capacity that will be used in the design of the fast-charging profile described in later chapters.

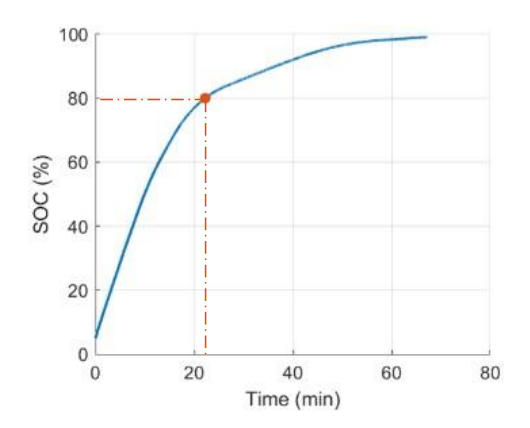


Figure 3.21: Ah charged into the module during fast charge with the Porsche Taycan power profile, assuming a module capacity of 124.35 Ah

Charging at 0.5C, it takes the module about 81 minutes to charge up to 80% SOC, while it takes the fast charge about 20 minutes to charge up to 80%. Charging at 2C would also have taken about 20 minutes to charge the module up to 80% had the temperature limit not been reached.

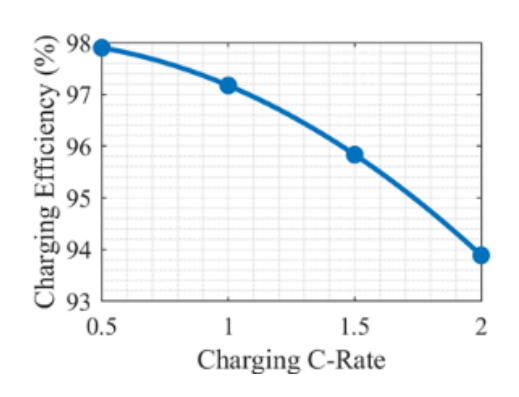
From the module tests, the charging efficiency, η_{ch} , was calculated with a correction to factor in the discharge loss, as shown in Equation 3.1, with the discharge loss, $Loss_{dch}$, given by Equation 3.2.

$$\eta_{ch} = \frac{E_{dch} + Loss_{dch}}{E_{ch}} \times 100\%$$
3.1

$$Loss_{dch} = \frac{Loss_{total} \times Crate_{dch}^{2} \times t_{CCDch}}{\left(Crate_{dch}^{2} \times t_{Dch}\right) + \left(Crate_{ch}^{2} \times t_{Ch}\right)}$$
3.2

Where E_{dch} and E_{ch} are the discharge and charge energy respectively in Wh; $Loss_{total}$ is the total loss from both charging and discharging; $Crate_{dch}$ and $Crate_{ch}$ are the discharging and charging C-rate respectively; and t_{CCDch} and t_{CCCh} are the duration of the discharge and charge respectively.

Figure presents the charging efficiency obtained for different charging rates. The module demonstrates a high charging efficiency of approximately 98% at 0.5C and 94% at 2C. The value obtained for the charging loss is assumed to be the peak module loss distributed over the charge. Assuming the larger Taycan pack size of 93.4 kWh, scaling this loss for each C-rate to the pack gives the measured loss shown in Figure . This is a representation of how much heat must be removed from the pack, including the heat which would go to the thermal mass of the battery during charging, assuming that it scales linearly. The results align with the expectation that the loss increases with higher C-rates, represented as $(I^2)R$ in Figure , and the measured loss is slightly higher than the theoretical loss.



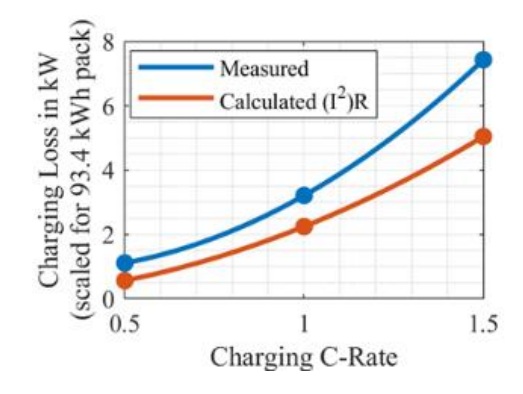


Figure 3.22: Charging efficiency of the Porsche Taycan module

Figure 3.23: Charging loss scaled to the 93.4 kWh pack for the different charging rates

The highest temperature reading on the cell surface was consistently obtained from thermocouple A1 which is close to the terminals as shown on the thermocouple placement in Figure, except during the 2C charge where A2 was slightly higher than A1, most likely due to the thermal resistance of the connections at the terminals which are closest to A2.

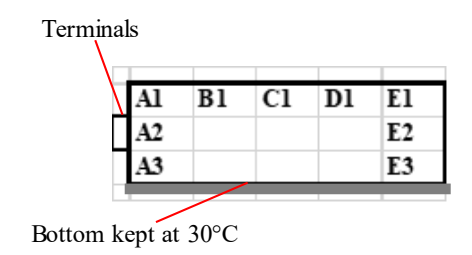


Figure 3.24: Thermocouple placement on the cell surface inside the module

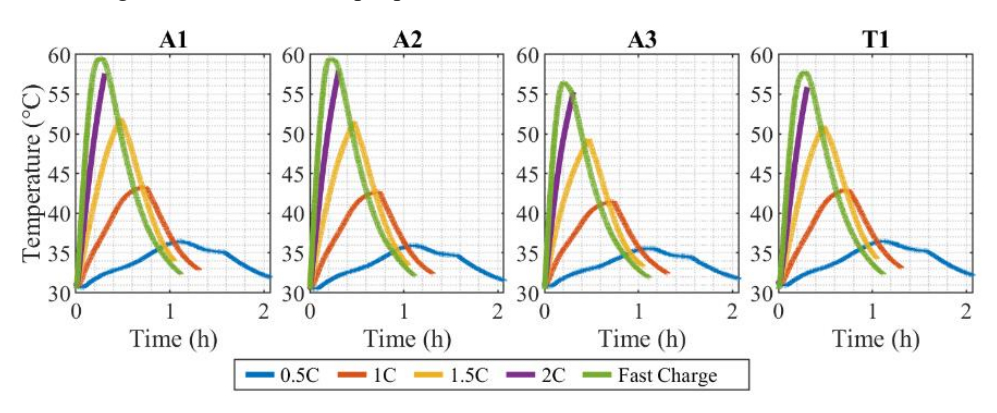


Figure 3.25: Temperatures on the cell surface and T1 for the different charging rates

As shown in Figure , the peak temperatures at A1 are 36.5°C, 43.3°C and 51.9°C at 0.5°C, 1°C and 1.5°C respectively. A2 and A3 are the other thermocouples close to the terminals, and T1 is the thermocouple placed at the position of the stock temperature sensor. With such a high current magnitude at 2°C (264 A), the temperature at the positive terminal hit 60°C, and the cell surface temperature also quickly approached 60°C at A1. However, in the fast charge, although the terminal temperature, measured for protection purposes by a separate thermocouple not shown here, approached 60°C even faster than for the 2°C charge, because of the gradual decrease in the charge power, the maximum cell surface temperature at A1 peaked at 59.5°C.

Figure illustrates the temperature distribution across the cell surface during charging tests at the time when T_{cell} is maximum. The hot spots on the cell surface are located at

both ends of the cell. The maximum temperature gradient between the highest and lowest temperature points on the cell surface at this instant is approximately 4.6°C during the fast charge, with a difference of 2.3°C from the centre. This temperature gradient at this point is less than 5°C which is recommended in lithium-ion battery packs because it is beneficial for cell aging and performance (Malik et al., 2017; Pesaran, 2002; Widyantara et al., 2022).

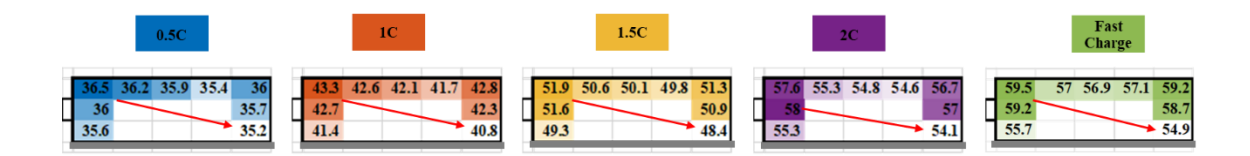
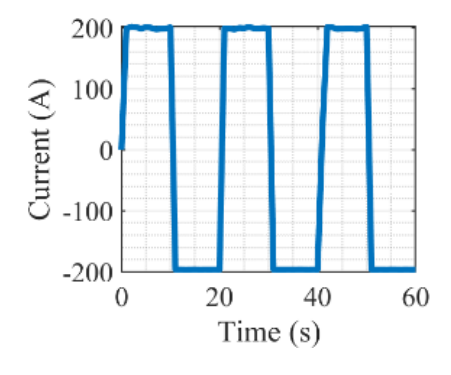


Figure 3.26: Temperature distribution across the cell surface for the different charging rates However, this does not represent the absolute maximum temperature gradient of 5.7°C which was obtained for a short while after the maximum temperature occurs, and the inlet coolant temperature is at its lowest, but the battery's heat generation is decreasing. It is not too far from the recommended variation of 5°C and it is only for a short while until the controller kicks in again because of the reduction on the temperature under the module.

3.2.2.2 Constant Power Loss Test Results

The cooling plate used for these tests is not the same design as in the Porsche Taycan. Constant power loss tests are, therefore, useful to assess the performance of the cooling system. Figure shows the first 60 seconds of the current profile applied to the module for the 1.5C constant power loss test and the accumulated cycler energy for the duration of the test was also obtained as shown in Figure .



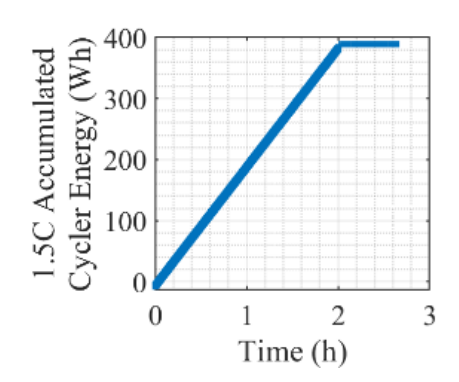


Figure 3.27: Sample 60s of current during 1.5C constant power loss test

Figure 3.28: Accumulated cycler energy for 1.5C constant power loss test

Since all the energy in a constant power loss test is treated as loss, the power loss, P_{loss} , is the slope of the accumulated cycler energy. To account for the losses that occurred in the cables from the cycler to the battery terminals, the total resistance of the cables was measured as 2.04 m Ω . This value was used to calculate the $(I^2)R$ losses across the cables, and thus, factor this deduction into the power loss obtained from the cycler energy, scaled to the cell. Finally, the temperature difference, T_{rise} , between the hottest point on the cell surface (A1) and the cooled surface (bottom of the module) at steady state was obtained. The thermal resistance, R_{th} , is therefore calculated using Equation 3.3:

$$R_{th} = \frac{T_{rise}}{P_{loss}}$$
 3.3

This procedure was repeated for the constant power loss tests at 0.7C, 1.2C and 1.5C, and the temperatures at A1 for each C-rate as well as the cell loss obtained are shown in Figure .

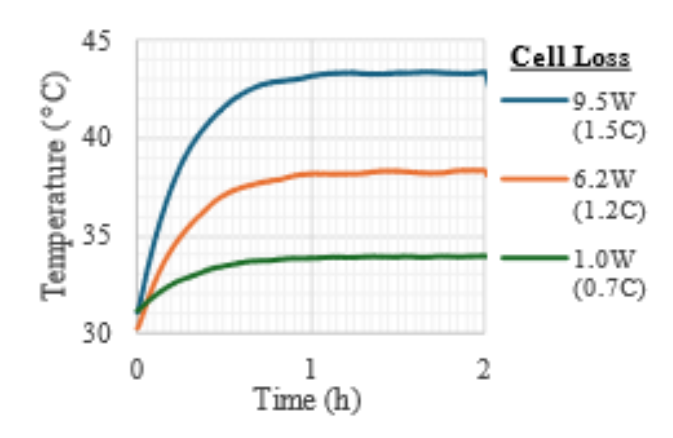


Figure 3.29: Temperatures at A1 for each C-rate and cell loss

The results obtained in Table are then plotted in Figure to get the overall thermal resistance of the system as 1.3132 °C/W.

 C-rate
 P_{loss} (W) per cell
 T_{rise} (°C)

 0.7
 1.0
 2.7

 1.2
 6.2
 8.3

 1.5
 9.5
 12.3

Table 3.6: Constant power loss tests

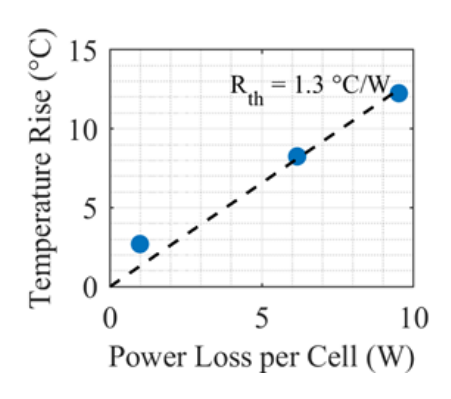


Figure 3.30: Temperature rise versus power loss for each C-rate

Using a simplified thermal equivalent circuit model and the temperature in Figure with the obtained thermal resistance gives a thermal capacity of about $850 J. kg^{-1}K^{-1}$. The procedure to do so is discussed further in Section 5.2.1.

3.3 Summary

In the module, during the charging tests, the temperature readings at T1, where the Porsche takes the module temperature readings from, was always slightly lower than the maximum cell surface temperature. During fast charging with the Taycan profile, T1 was lower than the hottest point, A1, which is close to the terminals, by 1.7°C. Therefore, the temperature readings used in the actual Porsche Taycan EV do not reflect the hottest points of the cell surface and may have some implications on battery life and safety especially during fast charge, where the temperature closely approaches the limits. Therefore, temperature readings at A1 will be used to represent the cell temperature when modelling this battery.

The results from the HPPC test and the OCV data from the characterisation are also necessary to estimate the voltage model parameters in 5.1.1 and design the battery loss model as will be discussed in Section 5.2.2.

The results obtained in this experimental evaluation of the module could be further improved by using cooling plates which match the design and specifications used in the Porsche Taycan. However, this is beyond the scope of this work. The aim of this thesis is to improve on the Porsche Taycan's fast-charging time while ensuring a lower cell surface temperature. The next chapter will investigate the most promising options among fast-charging protocols for lithium-ion batteries.

4 Fast-Charging Protocols for Lithium-Ion

Batteries

Charging time is a significant barrier to the adoption of EVs as an equal alternative to their internal combustion engine counterparts. As opposed to ICE vehicles whose gas tanks can be filled up from empty within five to ten minutes, EVs require up to 20 hours to fully charge the battery pack from a Level 1 AC charger (Charger Types and Speeds | US Department of Transportation, n.d.). Drivers who are used to the quick refill time of ICEs may have a hard time adapting to the extended charging duration of EVs and the additional challenge of range anxiety (10 Biggest Challenges Facing the EV Industry Today - EV Charging Summit Blog, n.d.). To help ICE vehicle drivers more easily adapt to EVs, and further reassure EV drivers of the viability of EVs for long-distance journeys, a lot of research is being done on fast-charging protocols. Before delving into the different charging protocols in literature, a basic understanding of the different charging systems is important.

In North America, the Society of Automotive Engineering (SAE) developed the J1772 standard, which defines categories of charging systems based on their rated power, voltage and current (Falvo et al., 2014). As mentioned in (Rachid et al., 2023), the October 2017 revision of the SAE J1772 defines the four charging levels as AC Level 1, AC Level 2, DC Level 1, and DC Level 2 which are discussed in detail below.

AC Level 1 charging uses an on-board charger which provides AC voltage of 120 V with two possible current levels of 12 A and 16 A, which gives a maximum power output of 1.44 kW and 1.92 kW respectively. It is typically a single-phase AC supply from a

household outlet. With 1.92 kW AC Level 1 charging, it is estimated to take about 17 hours to charge a BEV from 20% to 100%.

AC Level 2 charging also uses an on-board charger which provides AC voltage of 208 to 240 V, and it is typically supplied by a single-phase AC supply from a household installation or a charging station. The charging current can go up to 80A, but it is usually at 30 A. Additionally, the charging power can go up to 19.2 kW, with typical values of 7.2 kW. With 7 kW AC Level 2 charging, it is estimated to take about 3.5 hours to charge a BEV from 20% to 100%.

Both levels of DC charging can only be performed at a charging station with an output voltage ranging from 50 to 1000 V DC, with the charging current and power typically at 50 A and 50 kW respectively. DC Level 1 and DC Level 2 charging only differ in the maximum power and current values from the charging station. With DC Level 1 charging, the charging power can go up to 80 kW, and the maximum charging current is 80 A. With 50 kW DC Level 1 charging, it is estimated to take about 20 minutes to charge a BEV from 20% to 80%. On the other hand, DC Level 2 charging power can go up to 400 kW, and the maximum charging current value is 400 A. With 100 kW DC Level 2 charging, the estimated charge-time for a BEV is about 10 minutes from 20% to 80%.

It is evident that all fast charging would require DC charging, which can achieve faster charging times because of their higher power output and improved battery compatibility without the need for power converters.

However, despite the high-power output of the DC charging stations, the amount of power drawn by the battery pack is still controlled and limited by the on-board battery

management system (BMS) for the protection of the battery pack. The charging protocol is predetermined by an optimisation process based on the specifications of the cell used in the battery pack, and the BMS controls the power drawn based on this. Several factors affect the fast-charging behaviour of Lithium-ion batteries at the material level, cell level, pack level, and system level, some of which are discussed in detail in (Duru et al., 2021). For instance, the lithium-ion battery (LIB) architecture design is the first step in creating a fast-charging battery pack. High-specific-capacity anodes have a reduced thickness, which in turn, reduces the distance of charge carrier transport between electrodes, making them better materials for fast charging. (Duru et al., 2021) also mentions that the cathode chemistry affects the energy density, power density cycle life and thermal stability, with Lithium Iron Phosphate (LFP) being the predominantly used cathode material due to its high specific capacity, good cycling stability, and other favourable characteristics.

Various charging protocols have been studied extensively in literature to observe their impact on the performance, ageing and charge acceptance. The fast-charging protocols discussed here for their low complexity and ease of implementation, while still yielding promising results, are the constant current-constant voltage (CCCV) method, multistage constant current charging method (MCCC), boost charging method (BC), pulse charging (PC) method.

4.1 Constant Current-Constant Voltage (CCCV)

This is the most widely known and adopted charging algorithm due to its simplicity and ease of implementation (Shen et al., 2012). It is also frequently used as a benchmark to assess other charging protocols based on charging time, charging efficiency, and other

properties they may influence. A constant current (CC) is first applied to the battery in the CC mode until the battery voltage hits a preset maximum charging voltage, V_{max} . This initial charging current for the CC mode is chosen based on the specifications of the battery. Then, the charging voltage is kept constant in the constant voltage (CV) mode, at this preset value, V_{max} , while the charging current reduces exponentially to a predetermined minimum value. Figure shows the current and voltage profiles of the CCCV protocol.

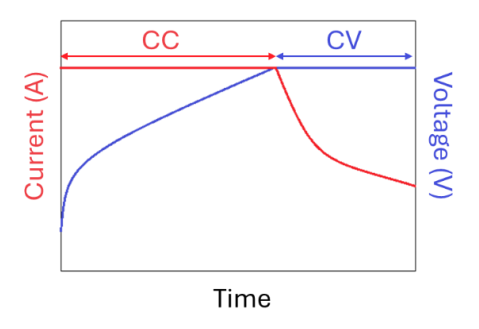


Figure 4.1: Illustration of the constant current-constant voltage protocol

Generally, the lower the charging current used in the CC mode, the higher the charging efficiency, the longer the charging time, and the longer the battery life (Shen et al., 2012). However, research has shown a high degradation rate when high currents are used in the CC mode (Bose et al., 2022).

4.2 Multistage Constant Current Charging (MCCC)

MCCC is considered as a variant of the CCCV method in various works such as (Bose et al., 2022; Gao et al., 2019; Sieg et al., 2019). This is because it still employs the CC mode, but it is divided into multiple steps starting from a higher current value and then decreasing the current at each subsequent stage when the preset cut-off voltage, V_{max} , is hit, which helps to increase battery life according to (Bose et al., 2022). This study

also refers to some works which studied a MCCC method where the charging current starts at a low value and increases at each stage, which reduces initial polarisation, but also lowers the capacity utilisation while increasing lithium plating. The last stage is the CV mode, which is the same as in CCCV mode, where the voltage is kept at V_{max} and the current decreases exponentially. Figure shows the current and voltage profiles of the MCCC method.

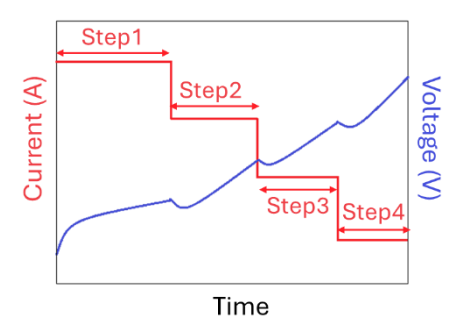


Figure 4.2: Illustration of a four-step multistage constant current charging protocol

A challenge in using the MCCC method is deciding on an appropriate charging current value and duration of each stage. (Shen et al., 2012) discusses different approaches used to determine the optimal current profile in literature – a fuzzy logic controller, the Taguchi method, the ant colony system, and using integer linear programming. (Bose et al., 2022) further mentions that these optimisation methods have been studied to determine the number of steps, current values at each step, and the duration of each step. The review in (Gao et al., 2019) discussed a paper which is based the current value on the internal resistance of the battery during charging, while (Sieg et al., 2019) refers to works which varied the cut-off voltage at each stage and compared the impact of the MCCC protocol on cycle life as opposed to other protocols.

4.3 Boost Charging (BC)

(Gao et al., 2019; Shen et al., 2012) also considered the boost-charging method as another variant of the CCCV method because it also uses the CC and CV modes, but at different points in the charging process. As described in (Notten et al., 2005), BC requires the battery to be fully discharged before starting charging, and the CV mode occurs at the beginning, called the boost charge period, where the maximum voltage, V_{max} , is applied to the battery for a short period of time which subjects the battery to a very high current. After the boost charge period, the standard CCCV protocol is then applied with much lower current values, and V_{max} does not necessarily have to be the same for the two CV periods in this protocol. If the currents at the boost charge period are unacceptably high, the alternative is to apply a more reasonable value for the current, I_{max} , changing the initial boost charge step from CV mode to CC mode, and then proceeding the standard CCCV protocol as well to fully charge the battery. Figure shows the current and voltage profiles of the BC protocol as illustrated in (Notten et al., 2005).

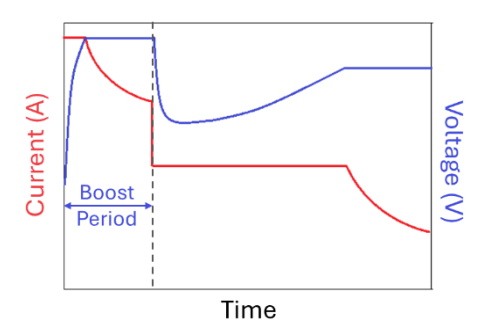


Figure 4.3: Illustration of the boost charging protocol

(Wassiliadis et al., 2021) explains that this high current at the beginning of charging could prevent lithium plating while minimising aging effects, and (Shen et al., 2012)

also states that V_{max} could also be set to 0.1 V higher than the battery's maximum voltage and that the charged capacity can reach around 30% of its nominal capacity in as little as 5 minutes.

4.4 Pulse Charging (PC)

Pulse charging is often presented as a fast and efficient charging protocol in literature (Gao et al., 2019; Shen et al., 2012). Here, intermittent pulses of high current separated by relaxation periods are applied to the battery. This method allows lithium ions to diffuse evenly, reducing the risk of lithium plating and enhancing battery life. However, the complexity of the control systems required for the rapid switching and the increased potential for heat generation are some of the challenges faced by this method. Figure shows the current and voltage profiles of the BC protocol.

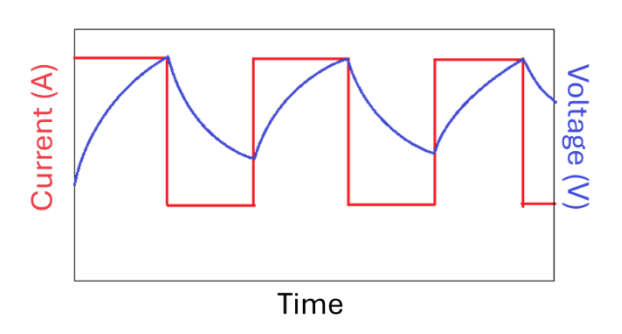


Figure 4.4: Zoomed-in illustration of pulse charging

(J. Liu & Wang, 2023) investigate how PC could be used to preheat the batteries at low temperature and, therefore, improve charging time. However, they also show how PC has a more pronounced effect on increased heat generation of the battery, which is contrary to the goal of this thesis. Nevertheless, it is a worthy mention because high-frequency PC has been found to be good for aging as discussed in (Huang et al., 2024),

as well as the following variations presented in literature. (Chen, 2007) proposed a variable frequency pulse charge system (VFPCS) which tracks and detects the optimal charge frequency during pulse charging. They found that the optimal frequency is variable. Therefore, fixed frequency pulse charging (FFPC) may not be perfectly suitable. With the proposed method, they recorded a 24% improvement in charging time as compared to CCCV charging. Furthermore, compared to an FFPC system with 100 Hz and 1 kHz, VFPCS showed 15% and 11% improvement in charging time respectively. However, a limitation in their analyses is that the charging time is only shown with respect to the voltage, and not the capacity.

The next chapter will explain the modelling procedure of the battery module for voltage and temperature prediction.

5 Electrical Model and Simplified Thermal Model of the Porsche Taycan Module

With the steadily increasing popularity of batteries as energy storage systems in a multitude of applications even reaching beyond the automobile industry, battery models are important for both battery operators and battery pack designers. An accurate battery model is useful in predicting the battery behaviour under different real-time operating conditions, and this prediction can help prevent unsafe operating points such as overcharging, over-discharging or high temperature, while also aiding in the development of efficient battery management systems (BMS) (C. Zhang et al., 2014). Battery models are also useful in estimating the performance indicators such as the state of charge (SOC), state of health (SOH), and cycle life (X. Zhang et al., 2016). Different battery modelling techniques have been studied extensively in literature, which are broadly classified into mathematical models, electrochemical models and electrical equivalent circuit models. The description of each as described in (Fotouhi et al., 2016) and other supporting literature is as follows.

Mathematical models could be analytical or stochastic. Analytical models are those where a series of equations is used to describe the properties of the battery. An example is the Kinetic Battery Model (KiBaM) developed by (Manwell & McGowan, 1993) which is based on the chemical kinetics of apparent change in capacity as a function of charge and discharge rates. Stochastic models, on the other hand, can predict the future of a process based only on the current state of the system without knowing its full history. A stochastic version of the KiBaM is presented in (Rao et al., 2005), represented

as a three-dimensional Markov process, which is the governing principle of the stochastic model.

From a different perspective, batteries are electrochemical systems and, therefore, can be represented using electrochemical models. These models represent the internal electrochemical dynamics of a battery using coupled partial differential equations that describe the impact of electrochemical reactions occurring within the cell on the generation and behaviour of the cell's potential. Because they are based on chemical reactions occurring at the microscopic level, electrochemical models are the most accurate of the different battery models. They also offer the advantage of full observability and virtual measurement of internal states which cannot, otherwise, be directly measured in practice. However, they are complex and impractical for real-time battery management due to their low-speed operation (Tamilselvi et al., 2021).

Due to the complexity of electrochemical models which limits their applications, the electrical circuit – also known as equivalent circuit – modelling (ECM) technique was developed. Today, this is the most applied battery modelling technique due to the reasonable accuracy it offers with much lower complexity, compared to the electrochemical model. ECMs are models where the battery is represented using electrical components such as resistors, capacitors and voltage sources. Various forms of ECMs exist such as the internal resistance model, the Thevenin models, and the Randles model and these are covered in detail in (Johnson, 2002; Mousavi G. & Nikdel, 2014; Salameh et al., 1992). However, for the purpose of this thesis, the second-order Thevenin model is used.

5.1 The Thevenin Battery Equivalent Circuit Model

The Thevenin ECM is the most prevalent ECM because of the simplicity but reasonable accuracy it offers (Hossain et al., 2019). It is used here for voltage estimation of the battery module. Figure shows the Thevenin equivalent circuit diagram for a single cell with n number of parallel RC branches.

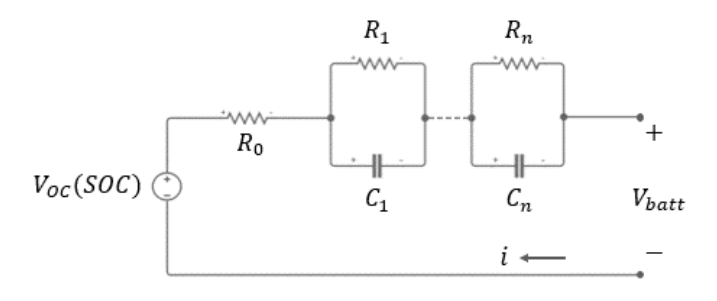


Figure 5.1: The venin equivalent circuit for a with n number of parallel RC branches

The voltage source, V_{OC} , which is a function of the battery's state of charge, represents the open circuit voltage of the battery. The series resistance, R_0 , which causes an instantaneous change in the battery terminal voltage during a charge or discharge pulse, represents the internal or ohmic resistance, and is also dependent on the battery's SOC. Finally, there are a number of parallel RC circuits, whose parameters are also dependent on SOC. Usually, one to three RC branches are used because, although an increase in the order of the RC branches increases the accuracy of the model, it also increases the complexity, and the additional computational complexity above the order of three does not give a directly proportional increase in accuracy. The fastest battery voltage transient is represented by the first RC branch, while the slower transient voltage components are represented by the remaining (n-1) branches. However, second order

ECMs are usually sufficient to model battery dynamics (Gurjer et al., 2019; Hossain et al., 2019).

The state-space equations of the second-order RC circuit for a given battery are given in Equations 5.1 and 5.2 below:

$$\begin{bmatrix} V_{1,k+1} \\ V_{2,k+1} \\ SoC_{k+1} \end{bmatrix} = \begin{bmatrix} 1 - \frac{\Delta t}{R_1 C_1} & 0 & 0 \\ 0 & 1 - \frac{\Delta t}{R_2 C_2} & 0 \\ 0 & 0 & 1 \end{bmatrix} \begin{bmatrix} V_{1,k} \\ V_{2,k} \\ SoC_k \end{bmatrix} + \begin{bmatrix} \frac{\Delta t}{C_1} \\ \frac{\Delta t}{C_2} \\ -\frac{\eta \Delta t}{C_{hatt}} \end{bmatrix} i_k$$
 5.1

$$V_{batt,k} = V_{OC}(SoC_k) - R_0 i_k - V_{1,k} - V_{2,k}$$
5.2

Where V_{OC} is the open circuit voltage (OCV) in Volts; R_0 is the internal resistance in ohms; R_1 and R_2 are the modelling resistance values for the first and second RC branches respectively in Ohms; C_1 and C_2 are the capacitance values in Farads across R_1 and R_2 respectively; C_{batt} is the battery capacity in Ampere-seconds; i_k is the input current in Amps; SoC_k is the battery's state of charge ranging from 0 (empty) to 1 (full); Δt is the sampling period in seconds; η is the Coulombic efficiency, assumed to be 1; and V_{batt} is the output of the model, which is the terminal voltage of the battery.

5.1.1 RC Parameter Estimation

The OCV is obtained through characterisation tests at 25°C, and the RC parameters, assumed here to be identical for both charging and discharging, are obtained using a preexisting battery modelling tool in MATLAB/Simulink developed by Javier Gazzarri (Gazzarri, 2024). The tool works by randomly initialising the parameters to be estimated, then, comparing the model output with the experimentally measured values until either the minimum cost function is reached, the difference between the parameters

in successive iterations is less than a specified tolerance value, or the specified number of iterations is achieved. The inputs of the model are the current and voltage which were obtained from the hybrid power pulse characterisation (HPPC) test data, as well as the initial guesses of the parameters to be estimated, while the outputs are the battery terminal voltage and the SOC. Because the tool uses the time constants of the RC branches as opposed to the individual C values, Equation 5.1 as used by the model is, therefore, rewritten as Equation 5.3:

$$\begin{bmatrix} V_{1,k+1} \\ V_{2,k+1} \\ SoC_{k+1} \end{bmatrix} = \begin{bmatrix} 1 - \frac{\Delta t}{\tau_1} & 0 & 0 \\ 0 & 1 - \frac{\Delta t}{\tau_2} & 0 \\ 0 & 0 & 1 \end{bmatrix} \begin{bmatrix} V_{1,k} \\ V_{2,k} \\ SoC_k \end{bmatrix} + \begin{bmatrix} \frac{R_1 \Delta t}{\tau_1} \\ \frac{R_2 \Delta t}{\tau_2} \\ -\frac{\eta \Delta t}{C_{hatt}} \end{bmatrix} i_k$$
 5.3

The parameters were estimated for three temperatures greater than 0°C –(10, 25 and 40°C), because these are the temperatures from the cell characterisation which fall within the acceptable temperature range of the battery module to allow charging. Lookup tables of the estimated parameters, dependent on the SOC and the temperature, were then created, and Figure shows the results of the parameter optimisation on the HPPC data obtained at 25°C. The state of charge element of the model was obtained simply by using the Coulomb counting method, assuming that the battery terminal voltage at the beginning of the test before any current is applied to the battery module is also the open circuit voltage because of the 1.5-hour relaxation time.

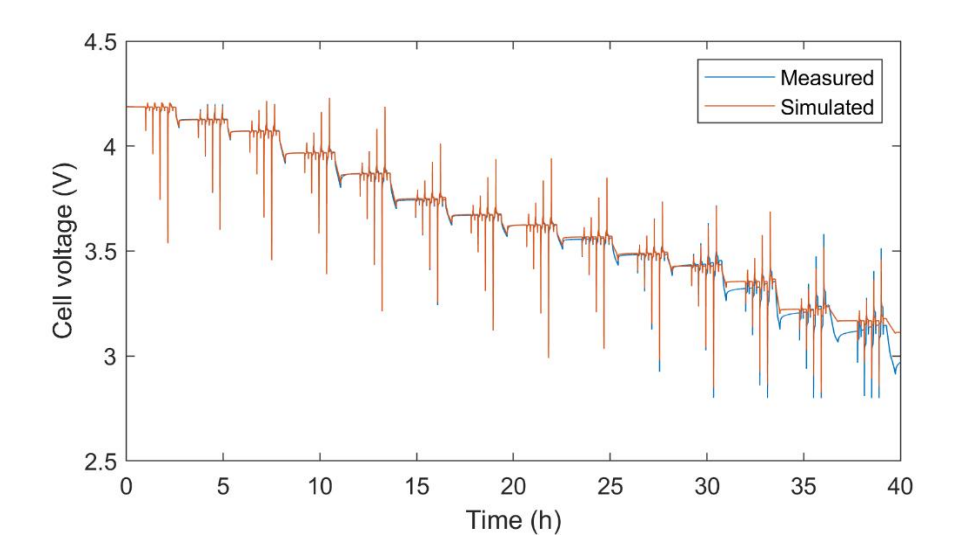


Figure 5.2: Parameter optimisation on the HPPC data at 25°C

The HPPC data used for the parameter estimation can be found on (Uwalaka et al., n.d.). For the HPPC tests, four charge and four discharge pulses were performed at 15 SOC levels – 100, 95, 90, 80, ..., 20, 15, 10, 5, 2.5, 0%, and the pulse magnitudes for each temperature were selected based on the limits of the preceding (higher) temperature, in order to ensure that the tests yielded useful battery characterisation data for as much of the SOC range as possible. Using this HPPC data, the estimated parameters are shown in Figure to Figure .

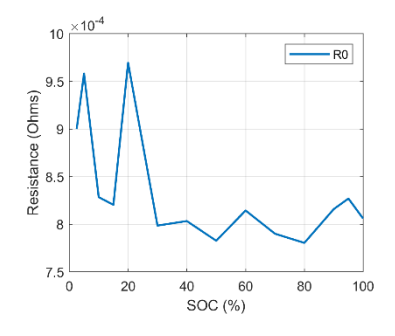


Figure 5.3: R0 at 25°C

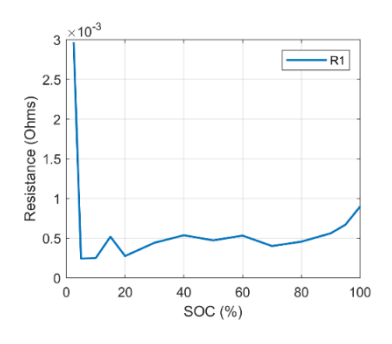


Figure 5.4: R1 at 25°C

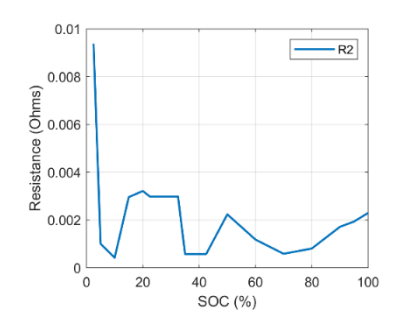


Figure 5.6: R2 at 25°C

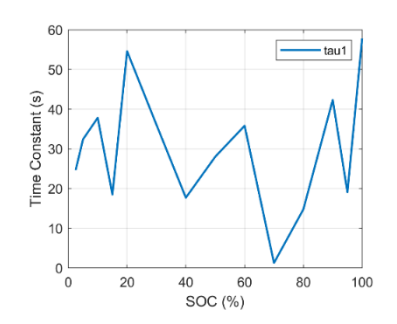


Figure 5.5: tau1 at 25°C

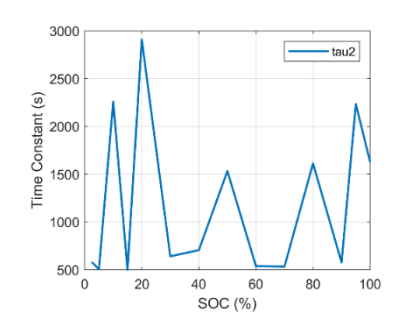


Figure 5.7: tau2 at 25°C

5.1.2 Validation of Estimated Parameters

The parameters estimated using the HPPC test at different temperatures were then validated using drive cycle data also obtained experimentally during the cell characterisation. Figure shows the current and voltage profile of the cell for the US06 drive cycle at 25°C, while Figure shows the measured and simulated voltage of the cell.

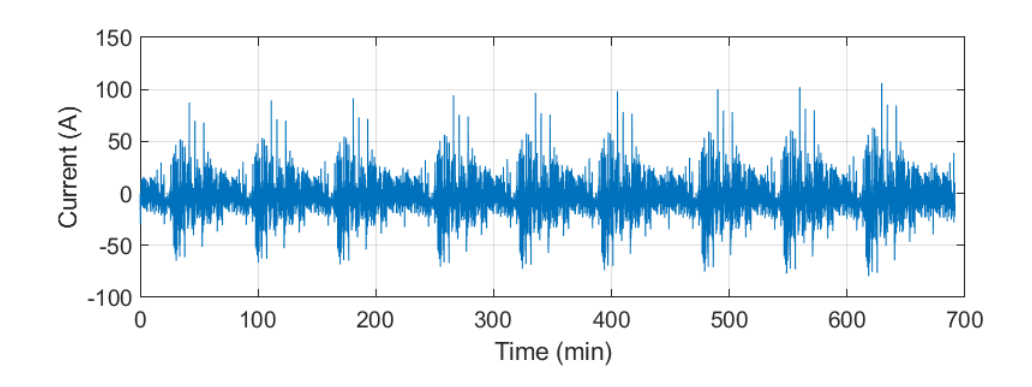


Figure 5.8: Current profile for the US06 drive cycle

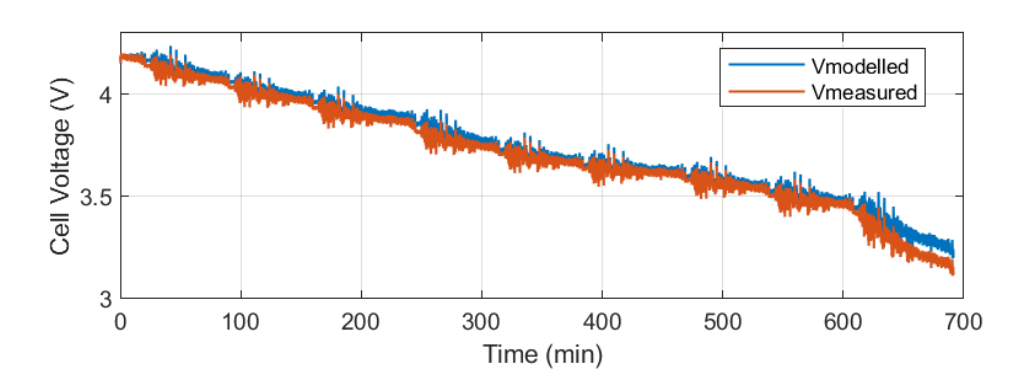


Figure 5.9: Measured and modelled voltage profile for the US06 drive cycle

The root mean squared error between the simulated and the measured voltage is 0.0334 V. There is reasonable agreement between the measured and the simulated voltage for the cell, which validates the estimated parameters.

5.2 Simplified Electrical Equivalent Circuit Thermal Model

As can be seen in the Simulink ECM for the battery terminal voltage prediction, the battery temperature is an input for the model. This is because, in general, the battery's operating temperature and the temperature variation within modules has a significant impact on battery performance (Karimi & Li, 2013). Therefore, a thermal model is

required for a holistic model. Figure gives an overview of the thermal model for the battery module developed based on a concept presented in (Iraola et al., 2013).

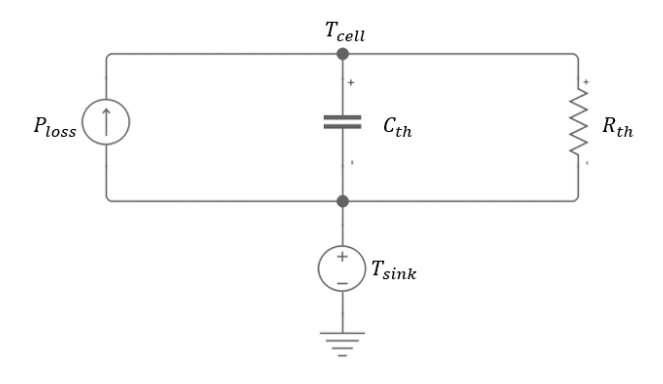


Figure 5.10: Thermal model electrical equivalent circuit

The thermal behaviour of the battery is modelled here as an RC circuit where P_{loss} represents the heat generation of the battery in Watts. The thermal resistance, R_{th} , in °C/W, resists the flow of heat out of the battery and, hence, is proportional to the temperature rise, ΔT in °C, which is calculated as the difference in temperature between a point on the cell surface, T_{cell} , and the bottom of the module, T_{sink} where the heat sink (the cooling plate) is located. In constant power loss tests, a higher thermal resistance gives a higher steady-state temperature.

The thermal capacity, C_{th} with units of J/ $^{\circ}$ C, on the other hand, impacts how much heat the battery can absorb without a significant increase in temperature. A higher thermal capacitance will slow down the rate of the temperature rise in the transient section of constant power loss tests. Because the battery module is covered with a fire blanket to imitate an adiabatic system, it is assumed that all heat generated by the battery is removed by the coolant flowing through the cooling plate, and none is lost through convection with the air in the thermal chamber.

As described in (Shabani & Biju, 2015), the temperature of the battery is obtained using the equation of a homogenous entity's heat exchange with the environment (in this case, the heat sink) in Equation 5.4.

$$C_{th}\frac{dT}{dt} = P_{loss} - \frac{T_{cell} - T_{sink}}{R_{th}}$$
 5.4

Where C_{th} is the thermal capacity (J/°C); T_{cell} is the cell surface temperature (°C); T_{sink} is the temperature at the boundary with the heat sink; R_{th} is the thermal resistance (W/m^2K) ; and P_{loss} is the power generated by the battery. To express Equation 5.4 in discrete time and iteratively calculate the temperature at each timestep, k, based on the temperature at the previous timestep, k-1, gives Equation 5.5 below:

$$C_{th} \frac{T_{cell,k} - T_{cell,k-1}}{\Delta t} = P_{loss,k} - \frac{T_{cell,k-1} - T_{sink}}{R_{th}}$$
 5.5

Therefore, solving for the cell surface temperature yields Equation 5.6:

$$T_{cell,k} = T_{cell,k-1} + \left(\frac{P_{loss,k}}{C_{th}} - \frac{T_{cell,k-1} - T_{sink}}{C_{th}R_{th}}\right)\Delta t$$
 5.6

Assuming that the initial temperature of the cell is equal to T_{sink} when the setup is at equilibrium temperature, this implies that $T_{cell} - T_{sink}$ is the temperature rise of the cell, which can be replaced by ΔT . Also, subtracting T_{sink} from both sides yields Equation 5.7 which calculates for temperature rise of the battery:

$$\Delta T_{cell,k} = \Delta T_{cell,k-1} + \left(\frac{P_{loss,k} - \frac{\Delta T_{cell,k-1}}{R_{th}}}{C_{th}}\right) \Delta t$$
 5.7

5.2.1 Thermal Model Parameter Identification

The equation for the cell surface temperature has two unknowns, C_{th} and R_{th} , which have been determined experimentally from the constant power loss tests as discussed in the previous section. The thermal resistance, R_{th} , obtained as the slope of the temperature rise per given power loss in Figure was obtained as 1.3° C/W. To identify C_{th} , because there is net zero charge during a constant power loss test, all the energy put into the battery module is therefore considered to be loss. The accumulated cycler energy in Watt-hours was first obtained, taking into consideration the measured $2.04m\Omega$ resistance (and hence power loss) of the cables which connect from the cycler to the battery module terminals. Because the constant power loss test runs for a duration of 2 hours, and reflects the total power loss of the 12 cells inside the module, the power loss for each cell, given by Equation 5.8, was calculated as 9.58 W.

$$P_{loss} = \frac{Accumulated\ cycler\ energy\ (Wh)}{2*12}$$
 5.8

Using the values of R_{th} and P_{loss} , the thermal capacity, C_{th} , was obtained as 850 J/kg°C by fitting Equation 5.7 to the temperature profile obtained from the constant power loss test. Figure shows that the constant power loss temperature obtained using these values of thermal resistance and thermal capacity give a good agreement with the measured values.

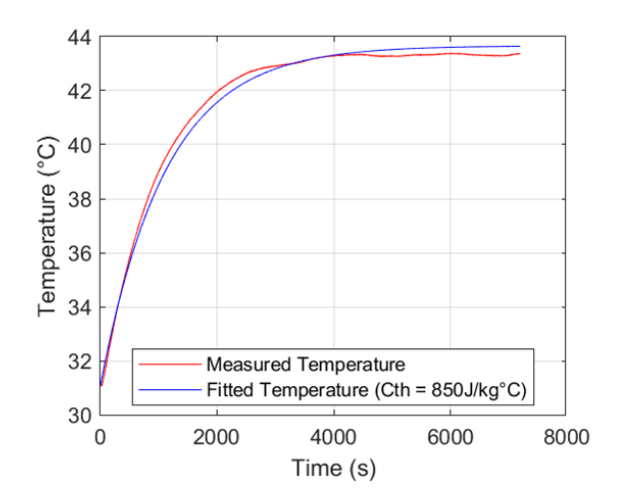


Figure 5.11: Fitted constant power loss test temperature for 1.5C using $C_{th} = 850 \text{J/kg}^{\circ}\text{C}$

5.2.2 Heat Generation

The equation for the internal heat generation of a battery, P_{loss} , is given by the Equation 5.9:

$$P_{loss} = i \times \{V_{OC}(SOC) - V_{batt}(SOC)\} - i \times \left\{ T \frac{dV_{OC}}{dT}(SOC) \right\}$$
 5.9

The first term in the equation is the irreversible component also known as the ohmic heat loss and the second is the reversible component also known as the entropic heat loss. The ohmic heating term is given by the product of the current and the absolute value of the difference between the open circuit voltage and the terminal voltage at any state of charge. For this study the entropic heat term is disregarded because, for the small proportion it contributes to the heat generation, the experimental measurement is known to be quite time-consuming. Therefore, because the ohmic heat loss is assumed to be the dominant term, the heat generation of the battery module for this work is given

by Equation 5.10 below. With this approximation, we anticipate some errors in the temperature estimation model.

$$P_{loss} = i \times \{V_{OC}(SOC) - V_{batt}(SOC)\}$$
 5.10

Figure shows the overall Simulink model for the cell surface temperature prediction at the thermocouple, A1, which was combined with the battery equivalent circuit model to create the electrothermal model for voltage and temperature prediction.

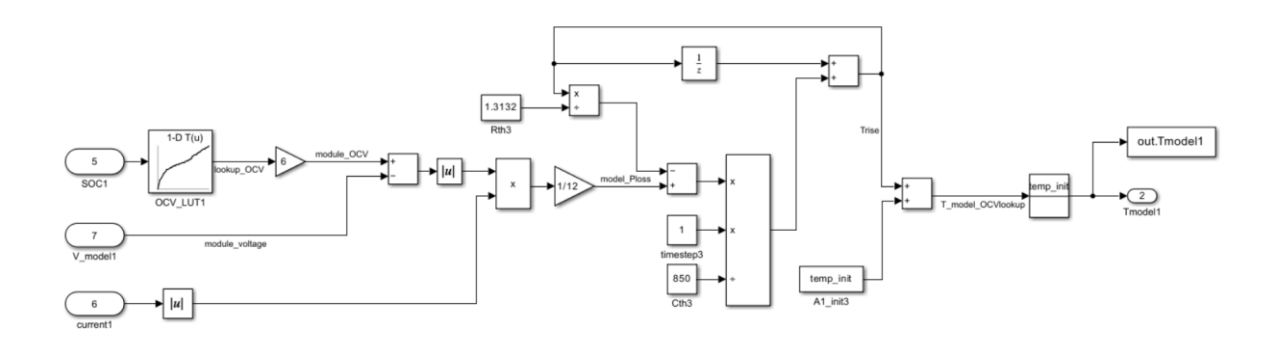


Figure 5.12: Simulink model of the simplified electrical equivalent circuit thermal model. The thermal model and the equivalent circuit model combined make the overall electrothermal model for the Porsche Taycan battery module which will be used for the design and simulation of the fast-charging profile.

5.2.3 Electrothermal Model Validation

The combined electrothermal model is shown in Figure . The current profile feeds into the ECM and the loss model, and is also used to obtain the SOC. The SOC is used to look up the OCV which is also fed into the battery loss model along with the estimated battery voltage obtained from the ECM to obtain the power loss from the battery. This power loss value is then fed into the thermal model which generates the estimated

battery temperature. This estimated battery temperature is the second input to the ECM which is required for the temperature-dependent parameters.

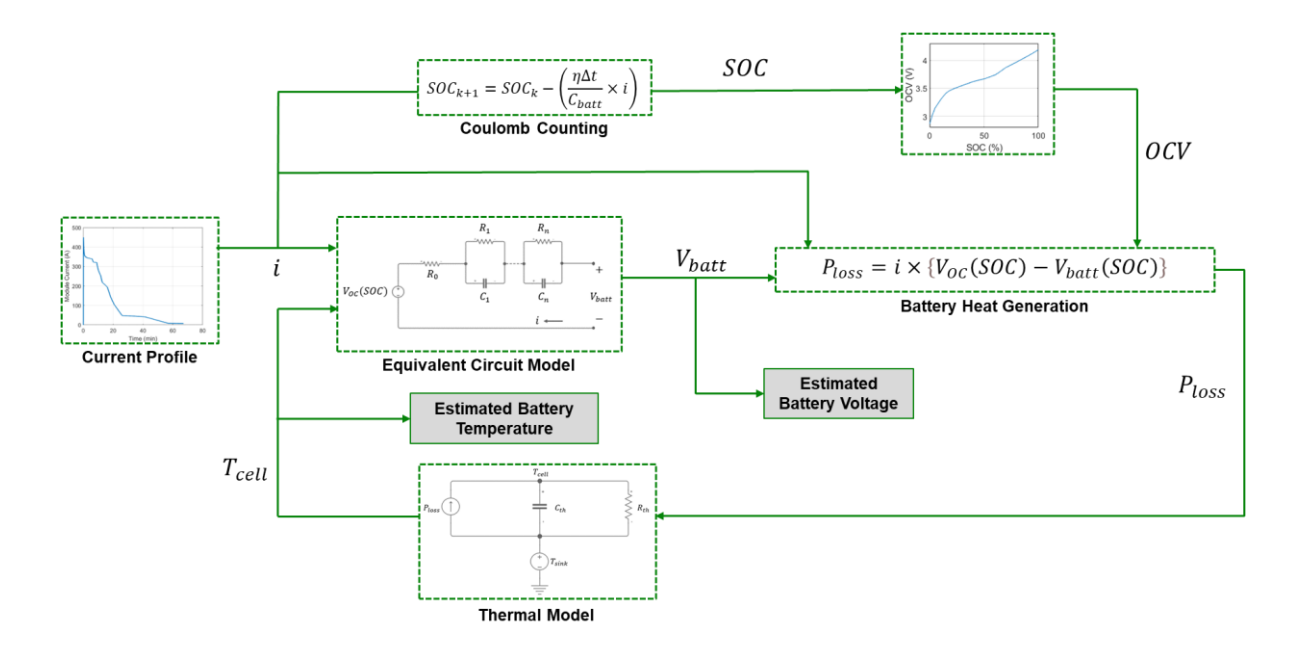


Figure 5.13: The combined electrothermal model

To validate the electrothermal model and assess its accuracy, the fast-charging test data performed on the battery module was used. The current profile from the experimental data serves as the input to the electrothermal model, which gives the estimated voltage and temperature. The current profile from the Porsche Taycan fast charge is shown in Figure 5.14 with the battery SOC in Figure 5.15. Figure shows the estimated voltage compared to the actual voltage measurement for the fast charge using this current from the Taycan fast charge profile, while Figure shows the temperature estimation of the model compared to the measured cell surface temperature at A1.

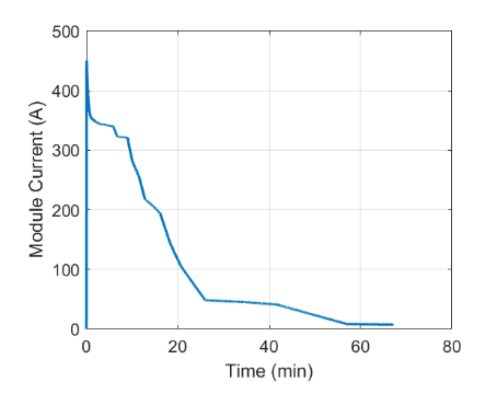


Figure 5.14: Current profile of the Porsche Taycan fast-charging profile

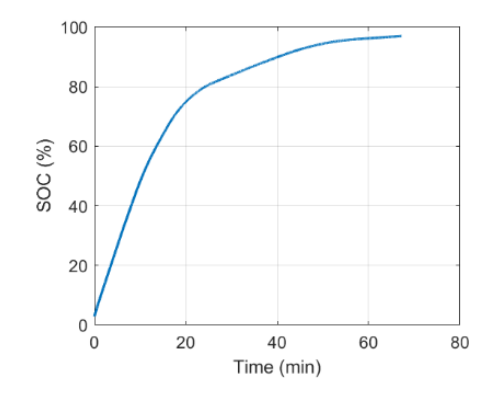


Figure 5.15: Battery module state of charge for the Porsche Taycan fast-charging profile

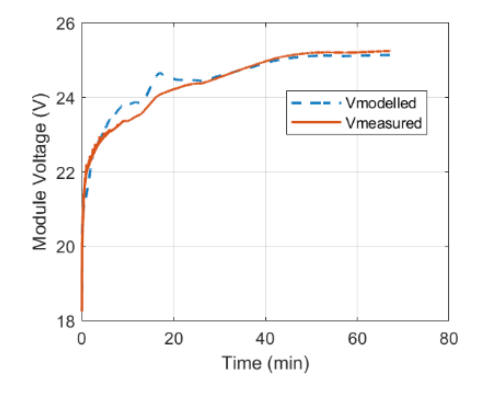


Figure 5.16: Estimated and measured module voltage during the fast charge

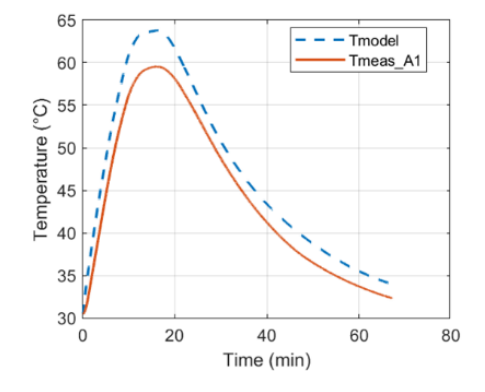
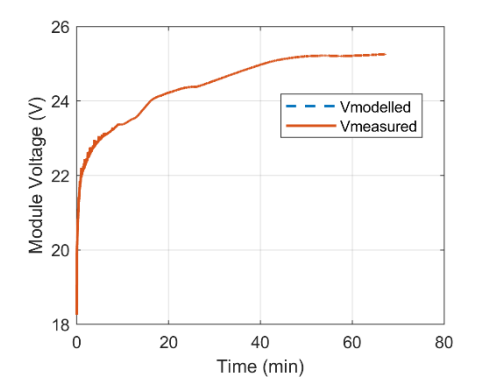


Figure 5.17: Estimated and measured module temperature during the fast charge

The root mean squared error of the model voltage and the actual measured voltage is 0.22 V which, although can be improved upon, is an acceptable error. The reason for the discrepancy could be attributed to the fact that the sixth parallel pair of cells in the battery module were aged as observed using the Orion Jr 2 BMS. This was also verified by the difference in the terminal voltage of the sixth parallel pair when compared to the other parallel pairs in the battery module. For the temperature estimation, the maximum temperature difference between the modelled and the measured temperature at A1 is 4.7°C. The error could be attributed to the error from the terminal voltage estimation which directly influences the battery loss model and hence, the temperature rise. To verify this, Figure shows the temperature estimated by the model when the measured

voltage is fed into the thermal model instead of the modelled voltage as shown in Figure

.



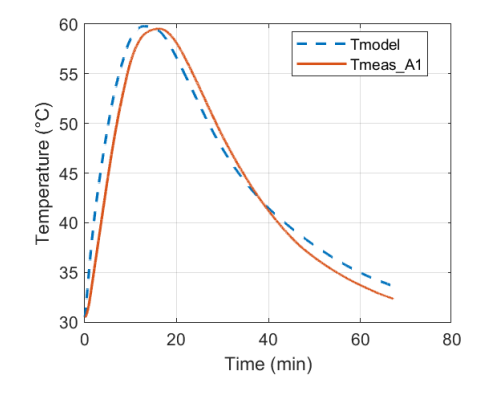


Figure 5.18: Measured voltage used for temperature prediction

Figure 5.19: Estimated temperature with a lower error of 0.23°C at maximum when model uses measured voltage

It is evident that the peak temperature prediction error is significantly lower than when performed using the modelled voltage, reinforcing the need for accurate voltage estimation models for the thermal model. Moving forward, the root mean squared temperature error of the electrothermal model is 2.9°C, which will be taken into consideration in the design of the fast-charging profile presented in the following section.

6 Design Methodology and Selection of the Fast-

Charging Profile

The review of fast-charging protocols reveals that the most used charging method is the constant-current constant-voltage charging protocol. However, this protocol is not practical in the design of a fast-charging profile because of its negative impact on battery health at high C-rates. Additionally, as presented in Section 4.1, using a constant-current value of 2C led to the interruption of the charge due to temperature constraints without having a significant reduction in charging time as compared to the Porsche Taycan fastcharging profile. On the other hand, considering a battery module capacity of 124.35 Ah, the Taycan's fast-charging profile had a continuous current of up to 3C after the initial transients which went up to 3.4C (450 A). With respect to pulse charging, although research has reported this protocol to be good for aging, it causes more heat generation. Therefore, because the focus of this work is on temperature-controlled fastcharging without taking into consideration the effects of aging, the pulse charging protocol is also inappropriate for this case. Boost charging is a promising protocol for our purposes because, as seen from Figure, although it does not explicitly have a duration of constant current at the beginning of the charge, the current profile from the Taycan profile does start at a high C rate for the initial transients and gradually decreases. An additional case for boost charging is that it is preferred to use high current values at low states of charge to minimise the chance of lithium plating occurring. Finally, multistage constant-current charging has been acclaimed for its fast-charging capabilities. Therefore, the fast-charging profile design was done based on the Taycan profile, taking into consideration the possibility of including a specific boost charging period at the beginning of the charge and employing multistage constant current charging with a ramp in between steps.

6.1 Fast-Charging Profile Design Procedure

From the Taycan profile, two things influenced the design procedure of the new fast-charging profile. Firstly, the maximum current peaked at 450 A at the beginning of the charge; however, after the transients, the current was continuous at about 340 A. Secondly, the current profile does not explicitly follow steps typical of the multistage constant current protocol, but rather follows a profile similar to a ramped step waveform. Based on these observations, the selected fast-charging profile outline is a ramped step waveform with three distinct step heights, to which variations will be made to assess their performance and select the best performing profile.

The main constraints in the design of the profile in all variations are as follows:

- The maximum temperature estimated by the electrothermal model should not exceed 63.5°C. This is because the root mean squared temperature estimation error from the Taycan profile is 2.9°C. Therefore, an estimate of about 63°C from the thermal model gives a buffer for actual results which will not exceed 60°C. 63.5°C was selected as the maximum temperature constraint in order to shortlist a larger number of results and better assess the distribution of the valid profiles.
- The maximum voltage estimated by the electrothermal model throughout the profile should be less than the maximum module voltage of 25.2 V.
- The initial temperature of the cell surface in the module should be at 30°C.

- The maximum duration of the profile to charge up to 80% should not exceed 1500 seconds (25 minutes). Once again, a maximum duration constraint slightly larger than the Taycan profile duration was chosen in order to shortlist a larger number of results and better assess the distribution of the results.
- The minimum duration of the profile to charge up to 80% is not less than 900 seconds (15 minutes), to ensure the results are kept within feasible bounds.

In the following subsections, the two main variations of this profiles generated are discussed in detail.

6.1.1 Variation 1 – Simple Ramped Step

The first variation is a simple ramped step waveform with three step heights as shown in Figure . The ramped step waveform was selected because the shape more closely aligns with the current shape of the Taycan profile. It also allows more variation in what fast-charging profiles can be obtained due to flexibility offered by changing the slope of the ramps as opposed to a simple stepped waveform. Under this variation, two options based on the magnitude of the initial step heights were considered as discussed below.

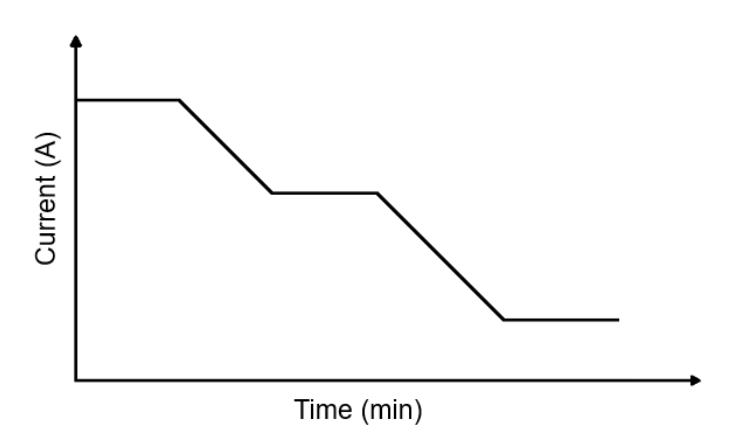


Figure 6.1: Outline of the fast-charging profile variation 1 – simple ramped step

6.1.1.1 Simple Ramped Step – 375 A Option

For the first option, the first step height was selected as 375 A, a value which falls between the maximum value of 450 A in the initial transient section of the Taycan profile and the continuous current of 340A. Using the capacity of the module as 124.35 Ah from the cell characterisation capacity, 375 A roughly translates to a value of 3C. The second step height was selected as 250 A which is approximately equal to 2C. For the final step height, this profile is designed to terminate charging at 80% SOC. Therefore, the Taycan profile was also analysed to obtain a reasonable current value which, from the experimental results, was certain to not cause overvoltage in the battery module at 80% SOC. This current value from the Taycan profile at 80% was about 120 A. However, because the first step height in the designed profile has been determined as 375 A which is higher than 340 A, it was presumed that using the same current value towards 80% SOC would quite possibly lead to overvoltage on the module, especially with the use of a 250 A current stage in between, which is higher than in the Taycan

profile. Therefore, the third step height value was selected as 100 A, which approximately equals 0.8C.

The variables in this profile are the durations of the three step heights and the two ramp durations. First, the maximum duration of each step height was determined by calculating the time it would take to charge the battery module up to 80% SOC assuming it were applied as a constant current. For a battery module capacity of 124.35 Ah, Table shows the calculated durations to 80% SOC for each step height magnitude.

Table 6.1: Durations for each step height for profile variation 1, 375 A Option

Current step	Time to 100%	Time to 80%	Constrained max
magnitude (A)	SOC (s)	SOC (s)	duration (s)
375	1193.75	955	955
250	1790.64	1146	1146
100	4476.54	3581	1500

For each step height, sixteen possible durations were generated from 1 to the maximum duration using the "linspace" function in MATLAB, and the first 1 second duration was eliminated due to its impracticality, leaving a total of 15 possible durations. For each ramp duration, the same procedure was repeated, but for thirty possible durations ranging from 0 to 1500 seconds (0 included) to allow for ramp duration increments of 50 seconds between possible ramp durations, as well as instantaneous step height changes when ramp duration is 0 s. Finally, because the SOC is calculated by the simple Coulomb counting method, it was possible to also perform a check that the time the profile takes to charge the battery up to 80% SOC is less than 1500 s. Only the generated duration combinations which met this requirement, as well as the condition, 80% ≤

 $SOC \le 85\%$, were shortlisted because of the high chance of overvoltage for any SOC greater than this value with the selected magnitudes for the current values.

A table of the duration variables was created based on the total minimum and maximum duration constraints mentioned previously, to generate the feasible combinations where the duration of the entire profile falls between 900 s and 1500 s. Based on this, 3423 possible combinations were generated for the 375 A Option which fulfilled the constraints. Table shows a sample of 15 rows of the generated table of durations for the 375 A option of the simple ramped step profile.

Table 6.2: Sample of 15 generated duration combinations for the 375 A option of the simple ramped step profile

1	2	3	4	5	6
Duration_375A	Duration_250A	Duration_100A	Ramp1_Duration	Ramp2_Duration	T_to_80
68	82	107	500	700	1442
68	82	107	550	650	1373
68	82	107	600	550	1342
68	82	107	600	600	1307
68	82	107	650	450	1311
68	82	107	650	500	1274
68	82	107	650	550	1250
68	82	107	700	350	1280
68	82	107	700	400	1242
68	82	107	700	450	1216
68	82	107	750	250	1248
68	82	107	750	300	1211
68	82	107	750	350	1183
68	82	107	800	200	1180
68	82	107	800	250	1150

6.1.1.2 Simple Ramped Step – 400 A Option

For the second option of variation 1, the first step height was selected as $400 \, \text{A} \approx 3.2 \, \text{A}$, which is lower than the maximum current value peaked during the transients with the Taycan profile (450 A), but also higher than 375 A, in order to observe the

performance of a higher initial step magnitude. The other two step height magnitudes remain the same as the 375 A Option.

Also following the same procedure as before to calculate the maximum durations for each step height based on the time it would take to charge the battery module up to 80% SOC yields the values shown in Table .

Table 6.3: Durations for each step height for variation 1, 400 A Option

Current step	Time to 100%	Time to 80%	Constrained max
magnitude (A)	SOC (s)	SOC (s)	duration (s)
400	1119.14	896	896
250	1790.64	1146	1146
100	4476.54	3581	1500

Once again, for each step height in the 400 A Option, fifteen possible durations were generated from 1 to the maximum duration using the "linspace" function in MATLAB and eliminating the 1 second duration. Thirty possible durations were also generated for the ramp durations, ranging from 0 to 1500 seconds (0 included) as well. Finally, only the generated duration combinations which charge the battery up to 80% SOC is less than 1500 s while ensuring that the condition, $80\% \le SOC \le 85\%$ was met, were shortlisted.

3653 possible combinations were generated for the 400 A Option which fulfilled the constraints. Table shows a sample of 15 rows of the generated table of durations for the 400 A option of profile variation 1.

Table 6.4: Sample of 15 generated duration combinations for profile variation 1, 400 A Option

1	2	3	4	5	6
Duration_400A	Duration_250A	Duration_100A	Ramp1_Duration	Ramp2_Duration	T_to_80
64	82	107	450	750	1450
64	82	107	500	700	1375
64	82	107	550	600	1337
64	82	107	550	650	1302
64	82	107	600	500	1300
64	82	107	600	550	1264
64	82	107	650	400	1262
64	82	107	650	450	1226
64	82	107	650	500	1201
64	82	107	700	300	1225
64	82	107	700	350	1187
64	82	107	700	400	1163
64	82	107	750	200	1187
64	82	107	750	250	1150
64	82	107	750	300	1125

6.1.2 Variation 2 – Ramped Step with Initial Step Current

The second variation is a combination of the simple ramped step waveform from the 375 A Option in Section 6.1.1 (375, 250, 100 A) with an initial step current whose duration is dependent on the time to charge to 10% SOC as shown in Figure .

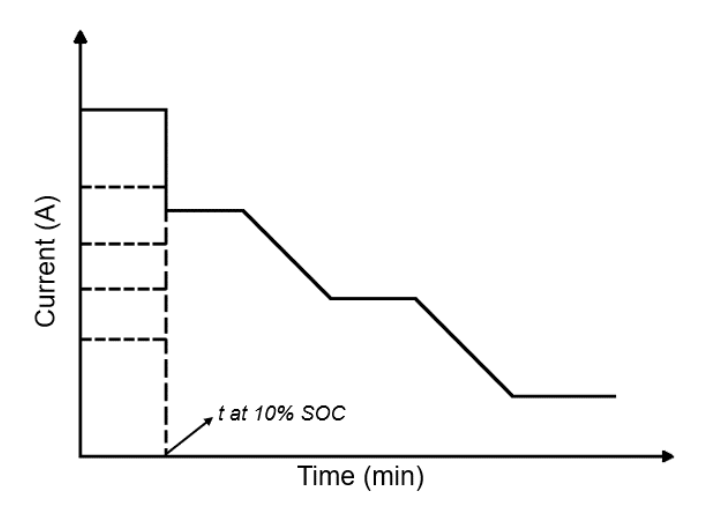


Figure 6.2: Outline of the fast-charging profile variation 2 – ramped step with initial step current

Under this variation, five options based on the magnitude of the initial step heights were considered as discussed below. This profile is based on the boost charging protocol where a high current magnitude is applied to the battery for a short period of time at the beginning of the fast charge when the state of charge is low. However, inspection of the battery resistance in Figure shows that the battery resistance, even for the temperatures of 10, 25 and 40°C relevant to the fast charging, almost doubles at the lowest SOC values when compared to the resistance around 15% SOC. With the understanding that the battery resistance has a significant correlation with the power loss of the battery as shown in Figure, five options of the initial step current magnitudes were analysed to determine their influence on the heat generation of the battery and to observe if the use of boost charging with very high current values initially is, in fact, counterintuitive to the goal of minimising temperature rise. With respect to the choice of 10% SOC as the transition point as opposed to 15% SOC, this is because the difference in resistance at 10% SOC and 15% SOC is not very significant. Also, the boost charging period should typically only last for a short while as discussed in Section 4.3. Therefore, 10% was a more logical choice.

For the initial step current magnitude, the five step current options considered to charge the battery module up to 10% SOC before the simple ramped step 375 A Option, were based on a boost current magnitude of 400 A. 400 A was chosen because it is lower than the maximum current value peaked during the transients with the Taycan profile (450 A), but also higher than 375 A which begins the 375 A Option simple ramped step profile. Based on this 400 A value and considering the I^2R power losses, the five initial step current options shown in Table were selected based on Equation 6.2 which was derived from Equation 6.1.

$$(I_1)^2 \times scaling\ factor = (I_2)^2$$
 6.1

$$I_2 = \sqrt{(I_1)^2 \times scaling \ factor}$$
 6.2

Where $I_1 = 400 \, A$; I_2 is the initial step current magnitude until 10% SOC, and the scaling factor was chosen as 1.56, 1, 0.8, 0.5 and 0.3. Because the initial step current only lasts until 10% SOC, its duration is calculated as a fixed value considering the initial SOC of the battery. The durations for the initial current step options assuming the battery is initially at 0% SOC are as shown in Table .

Table 6.5: Initial step current magnitudes and durations for variation 2 of the fast-charging profile

Scaling factor	Initial step current	Duration until 10% SOC (s)
	magnitude (A)	
1.56	500	89.5
1	400	111.9
0.8	358	125
0.5	283	158.2
0.3	219	204.4

The other variables in this profile are the durations of the components which occur after the initial step current – the three step heights (375, 250 and 100 A) for the ramped step and the two ramp durations. Just like before, the maximum duration of each step height was determined by calculating the time it would take to charge the battery module from 10% to 80% SOC assuming it were applied as a constant current. For the battery module capacity of 124.35 Ah, Table shows the calculated durations from 10% to 80% SOC for each ramped step height magnitude.

Table 6.6: Durations for each ramped step height after initial step current to 10% SOC

Current step	Time to 100%	Time from 10 –	Constrained max
magnitude (A)	SOC (s)	80% SOC (s)	duration (s)
375	1193.75	836	836
250	1790.64	1253	1253
100	4476.54	3134	1500

For the ramped step portion of the profile, the same procedure that was used in the 375 A Option was followed, but according to the new calculated durations shown in Table. Only the generated duration combinations that charged the battery up to 80% SOC within 1500 seconds, while ensuring that $80\% \le SOC \le 85\%$, were shortlisted.

A table of the duration variables was created based on the total minimum and maximum duration constraints mentioned, to generate the feasible combinations where the duration of the entire profile falls between 900 s and 1500 s. Based on this, Table A to Table A in Appendix A show a sample of 15 of the generated combinations for the duration of each step height in the ramped step portion of the second profile variation with initial step current.

6.2 Simulation of the Designed Profiles with the Electrothermal Model

The feasible duration combinations for the two fast charging profile variations were fed into the electrothermal model designed in Chapter 5. From the module tests, the module voltage after 1.5 hours of wait time after the complete discharge was recorded as 18.96 V. This is considered to be the open circuit voltage at the beginning of the charge, which

is used to obtain the module's initial SOC before the fast charge profile. This gives an initial SOC value of about 5.4%. Considering that the fast charge time recorded by Porche was also given for 5-80% SOC, this means that the results of the designed profile will give a good comparison to the Porsche Taycan's fast charging profile.

When running all the designed profiles on the electrothermal model with an initial temperature of 30°C as described in the constraints, the shortlisted profiles are those where the maximum temperature is less than 63.5°C and the module voltage is less than 25.2 V.

6.2.1 Variation 1 Performance – Simple Ramped Step

From the simulations, the 375 A Option of the first variation (step heights of 375, 250, 100 A) had a total of 583 duration combinations that met the requirements of voltage being less than 25.2 V and the maximum temperature being less than 63.5°C. The 400 A Option had 497 shortlisted duration combinations. Comparing these two options of the simple ramped step variation of the fast-charging profile, Figure gives a visual representation of the relationship between the maximum temperature and the charging time to 80% for these two options, including the measured and modelled peak temperature and time obtained from the Taycan profile.

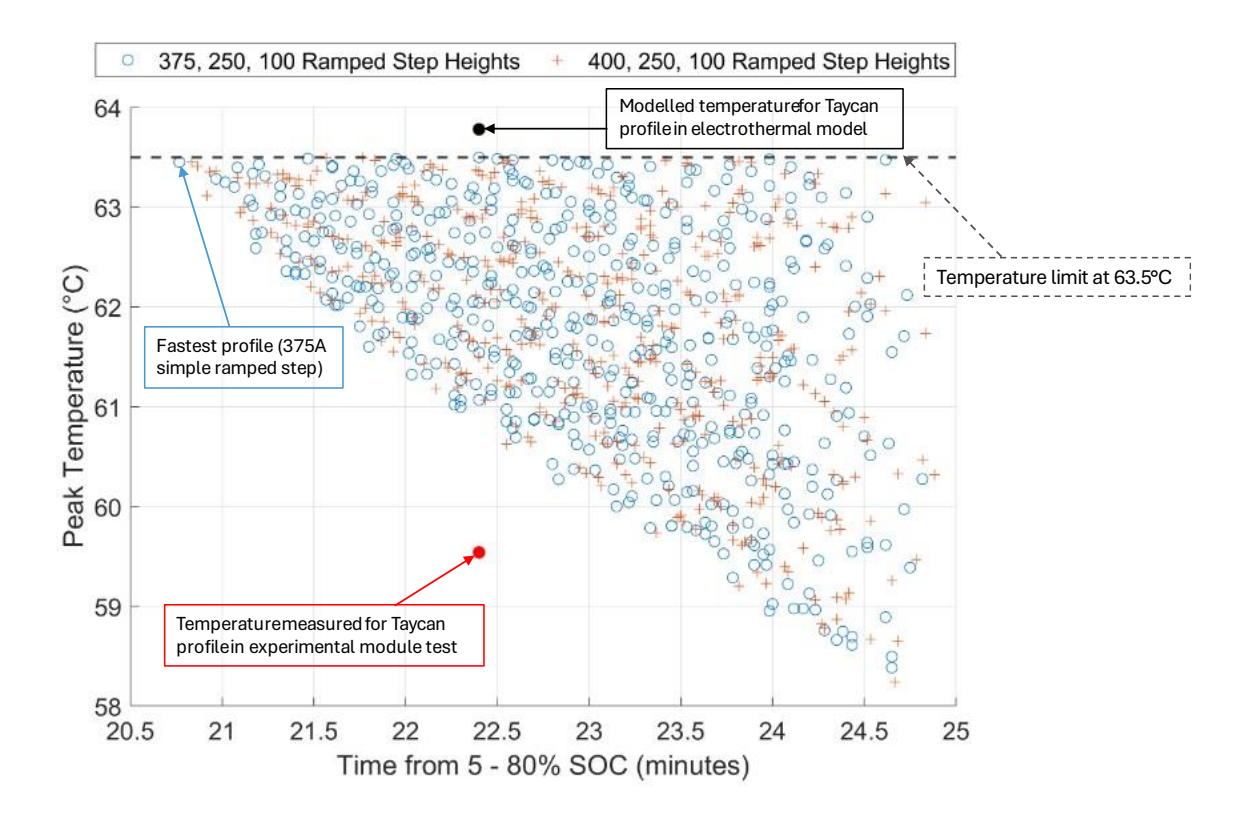


Figure 6.3: Peak temperature vs charging time for both options of the simple ramped step profile variation

Figure shows the simulated results from the profile which gave the shortest charging time of 20.8 minutes to 80% SOC with a peak modelled temperature of 63.5°C compared to the simulation results for the Taycan profile. Figure also compares the simulation results of the Taycan profile compared to the simulated results from the profile which yielded the lowest charging temperature of 58.2°C with a charging time of 24.67 minutes to 80% SOC. The initial SOC of the Taycan profile was offset upwards to align with the initial SOC of the designed profile at 5%.

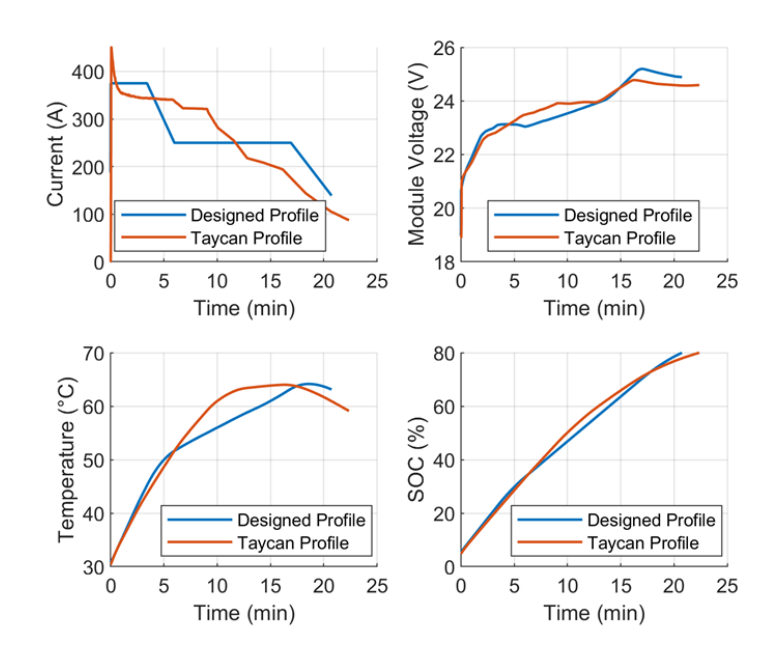


Figure 6.4: Simulated fastest charging simple ramped step profile (from the 375 A option) compared to the simulated Taycan profile

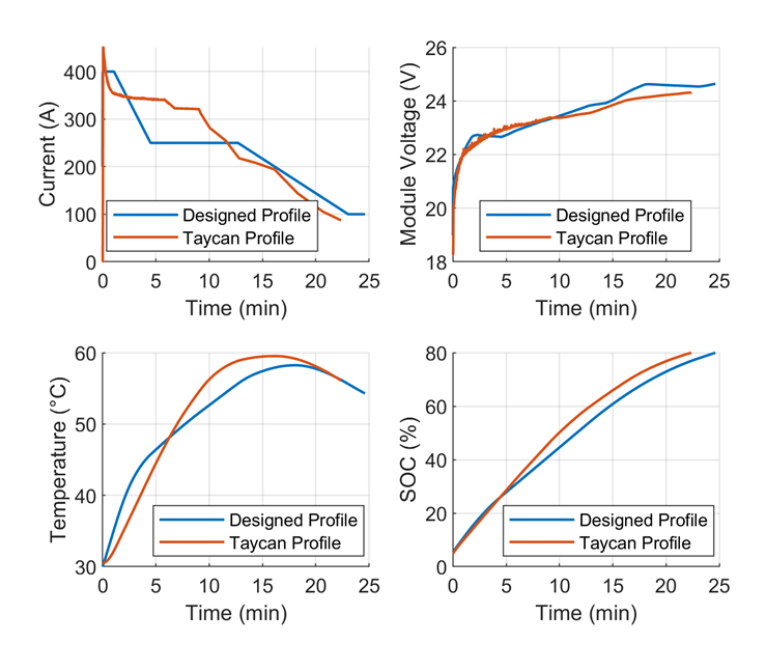


Figure 6.5: Simulated lowest temperature from simple ramped step profile (from the 400 A option) compared to the simulated Taycan profile

It is interesting to see from the plot in Figure that the profile with the lowest temperature rise is not the profile with the longest charging time, which emphasises the need for an efficient method of charging profile design.

Furthermore, there are two results which contradict the hypotheses of which option would give the faster charging time and which would give the lower charging temperature. The profile which gives the shortest charging time was surprisingly from the 375 A Option, not 400 A as one might expect. On the other hand, the lowest charging temperature occurs in the 400 A option, also contrary to the expectation of the 375 A option yielding the lowest temperature rise. However, to explain this from a neutral standpoint, the profile generation process did not consider all the possible duration combinations for both options. So, it is possible that there is a duration combination using the 400 A simple ramped step option which could outperform all 375 A option combinations with respect to charging time, or a combination using 375 A which could give the lowest charging temperature. Nevertheless, one can argue that the spread of the results from the 375 A Option and the 400 A Option look quite balanced in Figure, leading to the possible conclusion that there is not a significant benefit of increasing the first step height to 400 A as opposed to using 375 A. Therefore, in order to minimise the stress of higher currents on the battery, the 375 A option is considered moving forward. With respect to the profiles that match the performance of the Taycan profile, two duration combinations which charge in about the same total duration as the Taycan profile from the 375 A Option and the 400 A Option respectively are shown in Figure and Figure compared to the simulation results for the Taycan profile.

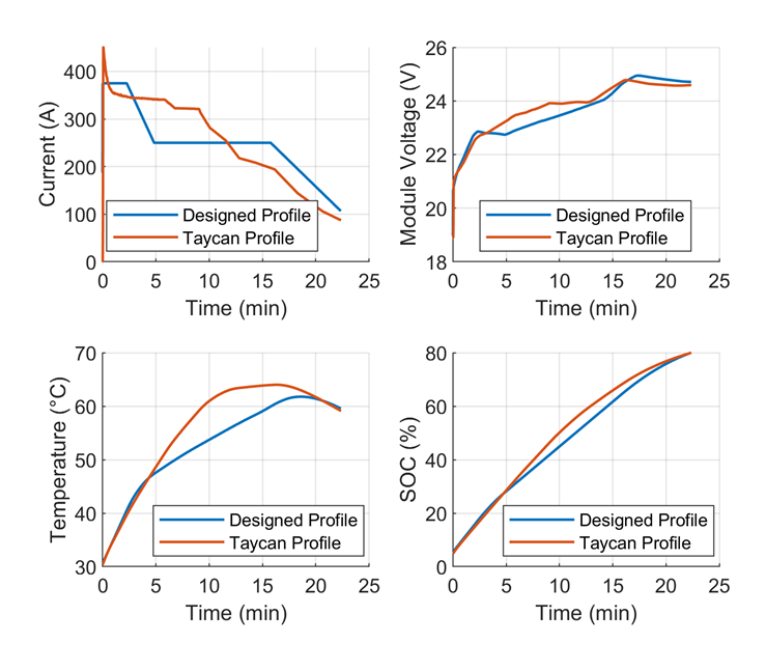


Figure 6.6: Simulated simple ramped step profile (375 A Option) with the same charge time (22.4 minutes) as the Taycan profile compared to the simulated Taycan profile

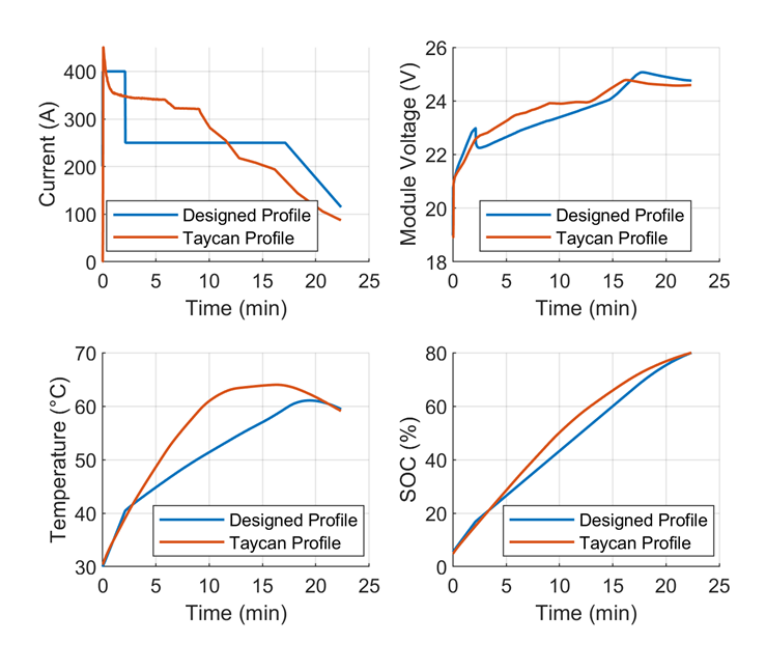


Figure 6.7: Simulated simple ramped step profile (400 A Option) with the same charge time (22.43 minutes) as the Taycan profile compared to the simulated Taycan profile

Figure and Figure above both have a maximum modelled temperature of 61.1°C which is lower than the modelled Taycan peak temperature of 63.8°C. However, considering

the temperature error of the model and, therefore, subtracting the model root mean squared error of 2.9°C, the anticipated peak temperature of these designed profiles in actuality is expected to be 58.2°C. Based on this result, the peak temperature is 1.3°C lower than the Taycan profile's peak temperature of 59.5°C, showing that the profile used in the Porsche Taycan is not the most efficient fast-charging profile in terms of the temperature rise.

6.2.2 Variation 2 Performance – Ramped Step with Initial Step Current

From the simulations, the second variation (initial step current of specified magnitude until 10% SOC followed by ramped step with heights of 375, 250, 100 A) had a total of 5662 duration combinations that met the requirements of voltage being less than 25.2 V and the maximum temperature being less than 63.5°C. The number of valid duration combinations which can charge the battery module in less than 25 minutes were 966, 1097, 1157, 1211 and 1231 for the 500 A, 400 A, 358 A, 283 A and 219 A initial step current options respectively. Comparing the five options of the ramped step with initial step current variation of the fast-charging profile, Figure gives a visual representation of the relationship between the maximum temperature and the charging time to 80% for all options, including the measured and modelled peak temperature and time obtained from the Taycan profile.

The profile which gave the fastest charging time of 20.8 minutes to 80% SOC is shown in Figure 6.9, while Figure is the profile which yielded the lowest charging temperature of 57.37°C with a charging time of 24.9 minutes to 80% SOC. The simulated results are shown, compared to the simulated results of the Taycan profile.

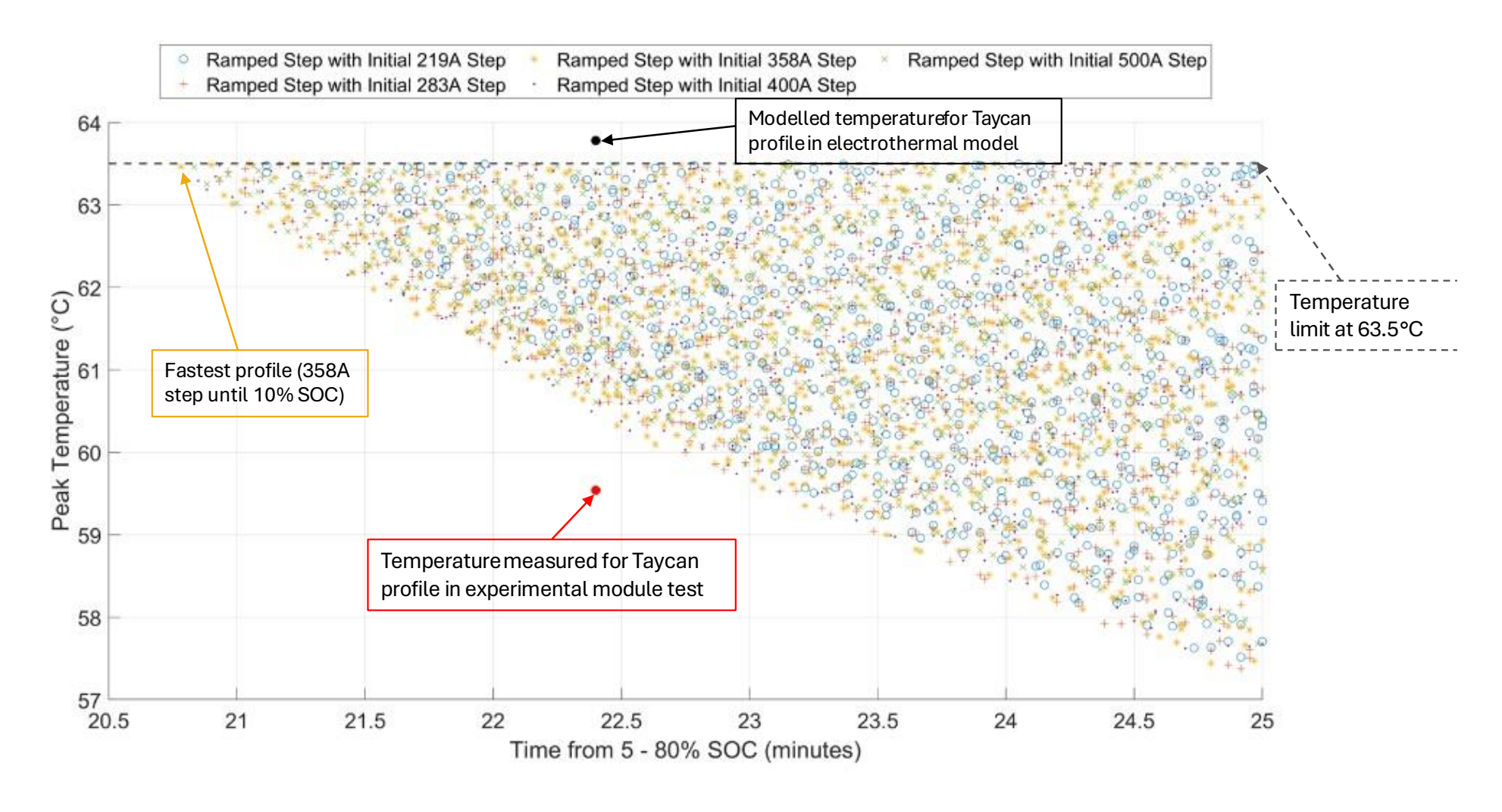


Figure 6.8: Peak temperature vs charging time for the five options of the ramped step with initial step current profile variation

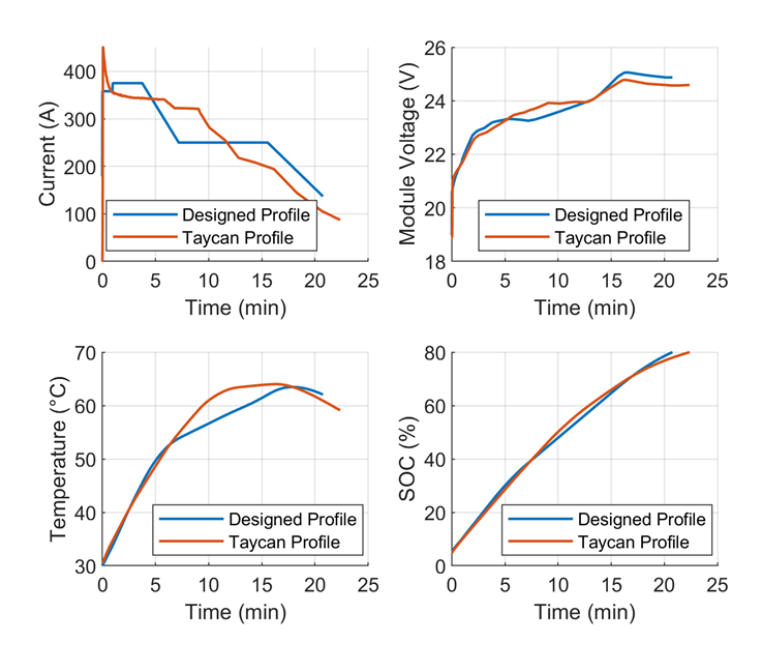


Figure 6.9: Simulated fastest charging (20.8 minutes) ramped step with initial step current profile (from the 358 A option) compared to the simulated Taycan profile

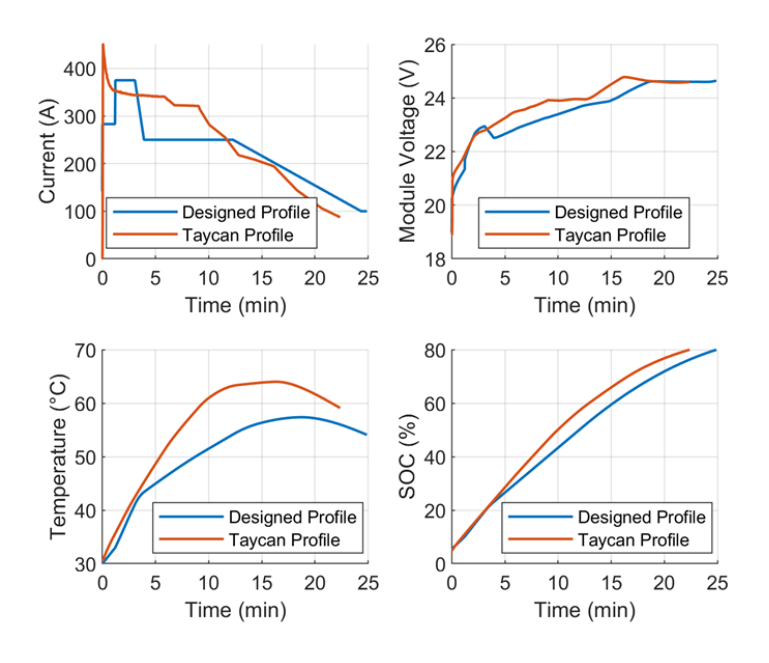


Figure 6.10: Simulated lowest temperature ramped step with initial step current profile (from the 283 A option) 20.8 minutes

Similar to the results from the simple ramped step variation which contradict the expectation of the fastest profile and the lowest temperature profile, the profile which gives the shortest charging time in the ramped step with initial step current profile

variation was the 358 A option, not the 500 A option as expected. This profile also charges the battery module up to 80% SOC before the final ramp step height is reached. However, the lowest charging temperature was from the 283 A option and, as seen in Figure , for the same charging time, the 500 A option very rarely gives the lowest temperature rise, which is not surprising due to the high initial step current magnitude. Again, these results are for a profile generation process which does not consider all the possible duration combinations for the waveform durations.

Another evident result from Figure is that, as the charging time reduces, for the same charging time, the lowest initial step current option (219 A) consistently does not yield the lowest temperature rise within the specified constraints, as compared to the other four higher current options. This could be explained by the higher durations required for the subsequent current steps of a higher magnitude (375 A and 250 A) in the ramped step portion that comes after, to reduce the total charging time. Therefore, the advantage of lowering the initial power loss in the higher battery resistance region is lost when using 219 A. Nonetheless, besides the observation of the 219 A option in Figure , the spread of the results from the other options is balanced, although the best performance seems to consistently be from the 358 or 400 A options. The 500 A option not being among the lowest temperature values validates the initial concern about the higher boost current values being counterproductive to the design objectives, by causing a higher temperature rise.

Figure to Figure are included in Appendix B to show the variations from each option which charge in about the same 22.4-minute duration as the Taycan profile but with a lower temperature rise.

Table gives the maximum temperature obtained from the electrothermal model for the profiles in Appendix B which charge in the same time as the Taycan but show lower temperature rise in the simulation results, as well as the anticipated actual maximum temperature when taking into account the model error.

Table 6.7: Estimated maximum temperature from electrothermal model and approximated actual temperature for each initial step current option with the same 22.4-minute charging time as the Taycan

Initial	Model T _{max}	Actual T _{max} (Model	Reduction vs
current	(°C)	T_{max} – RMSE) (°C)	Taycan profile
option			(°C)
219	61.5	58.6	0.9
283	61.1	58.2	1.3
358	61.3	58.4	1.1
400	61.6	58.7	0.8
500	60.6	57.7	1.8

The profile from the 500 A initial current step option yields an almost 2°C temperature drop compared to the Taycan profile with the same charging time. Once again, this proves that the profile used in the Porsche Taycan is not the most efficient fast-charging charging profile, and several more efficient alternative fast-charging profiles have been generated and validated to prove this using the electrothermal model. In the next section, the generated profiles will be validated experimentally to verify the performance of the designed profiles and the electrothermal model.

7 Experimental Verification of Selected Fast-

Charging Profiles

Two profiles were selected from the generated simple ramped step profiles with step heights of 375, 250 and 100 A for experimental verification.

7.1 Verification Test Procedure

Table shows the verification test procedure performed using the selected profiles.

Table 7.1: Selected fast-charging profile verification test procedure

Step	Action	Step End
1	Soak module in thermal chamber at 30°C with coolant at 30°C	$T_{cell} \ge 30^{\circ}C \text{ AND } T_{cell} \le 31^{\circ}C$
2	Cover module with fire blanket	
3	Top-up charge with 1C MCCC (132A,	$V_{cell} \ge 4.18 V$
3	66A, 33A, 16.5A, 10A, 5A)	at 5 A
4	Wait	$1 hr$ AND $T_{cell} \ge 30^{\circ}C$ AND
	wait	$T_{cell} \leq 31^{\circ}C$
5	Discharge at C/4	$V_{cell} \le 2.8 V$
6	Wait	$1 hr$ AND $T_{cell} \ge 30^{\circ}C$ AND
	wait	$T_{cell} \leq 31^{\circ}C$
7	Charge with selected fast-charging	Profile end
/	profile	I i oj ite enu
8	Wait 30 minutes	30 minutes
9	End	

7.2 Results for Simple Ramped Step Profile

7.2.1 Profile with Modelled Peak Temperature Less than 60°C

The first profile to be verified is an arbitrary profile highlighted in Figure 7.1 below for which the electrothermal model gives a maximum temperature below 60°C.

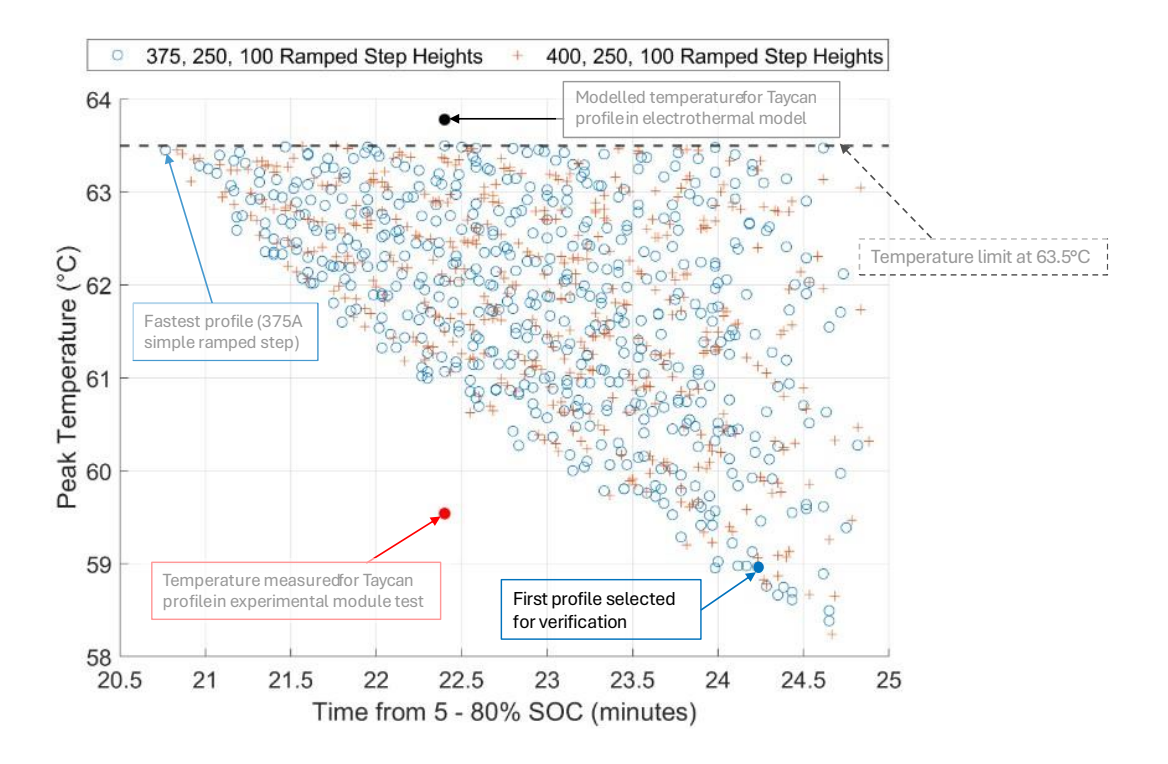


Figure 7.1: First profile selected for experimental verification with modelled peak temperature less than $60^{\circ}\mathrm{C}$

This profile was selected as the first test for verification as a safety precaution, because it would verify the actual temperature rise during experimentation as compared to the temperature estimated by the electrothermal model while staying well below the maximum temperature of 60°C on the cell surface. The selected profile has a charging time of 24.2 minutes, and the modelled maximum temperature is approximately 59.0°C

which, when factoring in the root mean squared error, gives an expected actual temperature of 56.0°C.

Figure shows the results from the experimental verification of this profile compared to the results from the electrothermal model.

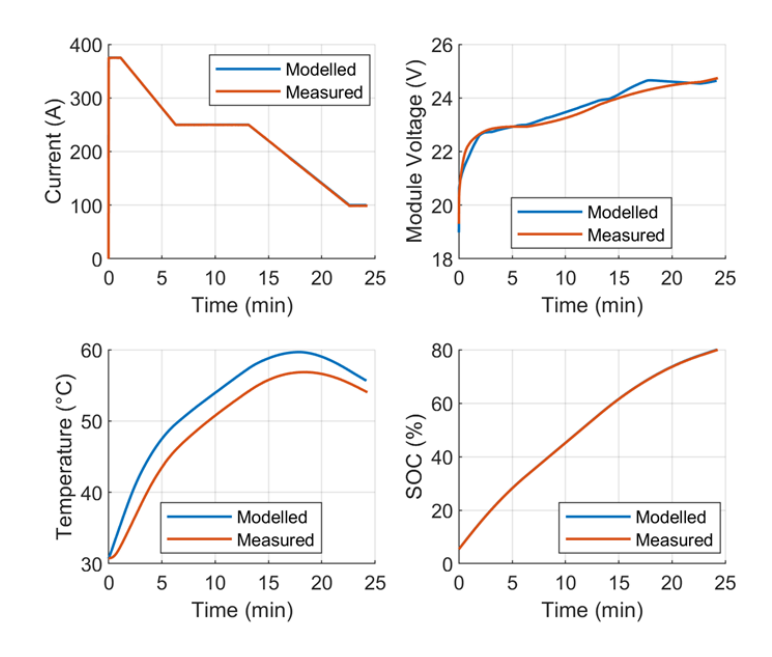


Figure 7.2: Modelled and measured data for the first selected profile with peak temperature less than $60^{\circ}C$

The maximum temperature obtained experimentally is 56.9°C, which is in close alignment with the expected temperature of 56.0°C when taking the root mean squared error from the model into consideration and subtracting this error from the model estimate of 59.0°C. The root mean squared error of the measured and estimated temperature for this profile is 2.4°C while that of the voltage is 0.24 V. These results are in close alignment with the expected values, showing that the electrothermal model does a good job of voltage and temperature estimation.

Figure gives a distribution of the cell surface temperatures at the point when the overall maximum surface temperature occurs at A1.

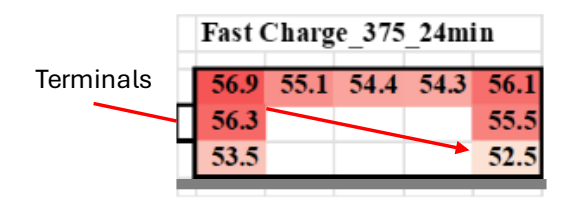


Figure 7.3: Cell surface temperature distribution when T_{cell} is maximum for the selected 24-minute profile

The maximum temperature variation across the cell surface at this instant of peak cell surface temperature is 4.4°C from thermocouple A1 to thermocouple E3. However, the overall maximum temperature variation of 5.1°C does not occur at this point, but instead when A1 is at 56.0°C, after the peak cell surface temperature is reached as shown in the temperature profiles of A1, E3 and the coolant inlet temperature on Figure, because this is when the inlet coolant temperature is minimum, and the heat generation of the battery is reducing. However, a temperature variation of 5.1°C is not too far from the recommended maximum temperature variation of 5°C, and so this was considered as an acceptable value for the cell, considering that the Taycan profile gave a maximum temperature variation of 5.7°C across the cell surface.

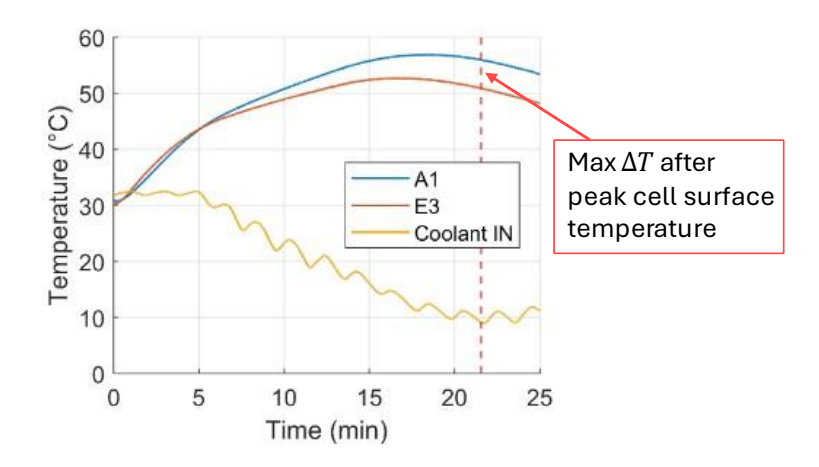


Figure 7.4: Temperature at A1 (hottest spot), E3 (coolest spot), and the inlet coolant temperature

7.2.2 Fastest Designed Profile within Constraints

With the results from the first verification test in Section 7.2.1, the temperature difference between the maximum experimental temperature reading and the maximum modelled temperature reading is 2.1°C. This hints at the likelihood that choosing a profile with a peak temperature greater than 62°C would cause the temperature to exceed the limit of 60°C. Because of this, the temperature limit for the selection of the fastest profile selection was adjusted to 62°C as shown in Figure, which also shows the updated selection for the fastest charging profile that charges the battery module up to 80% within 21.75 minutes with a peak temperature below 62°C.

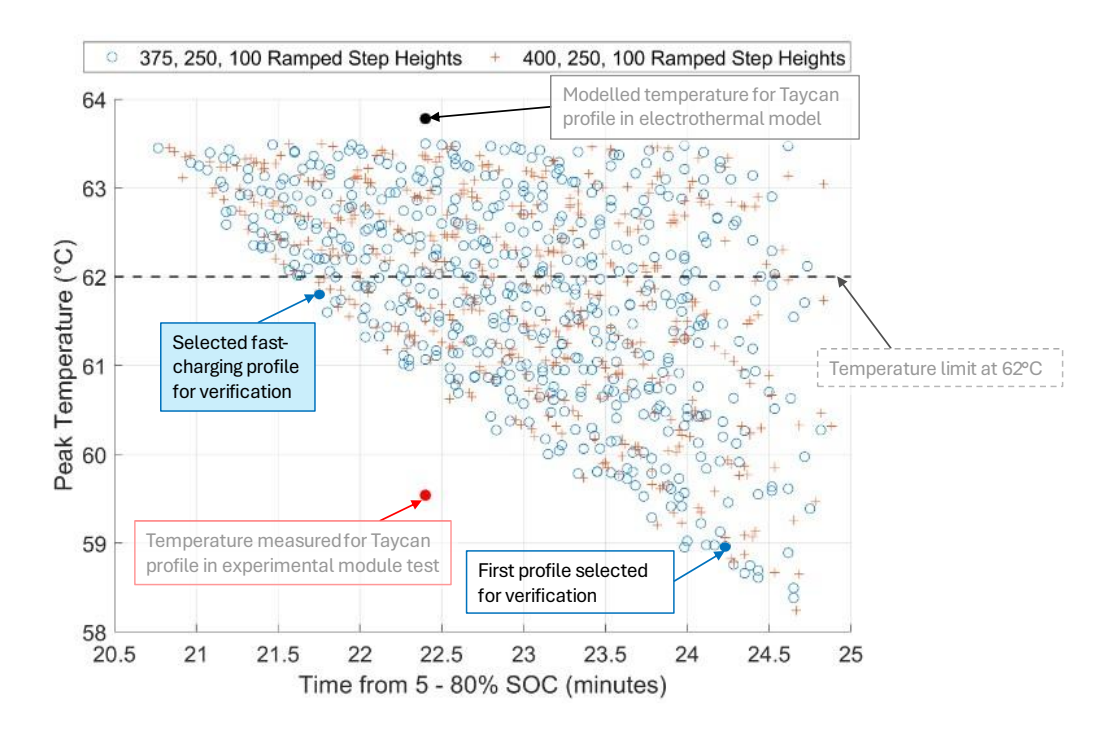


Figure 7.5: Updated temperature limit at 62°C showing the updated selected fast-charging profile for the simple ramped step profile variation

Figure shows the results from the experimental verification of this profile compared to the results from the electrothermal model.

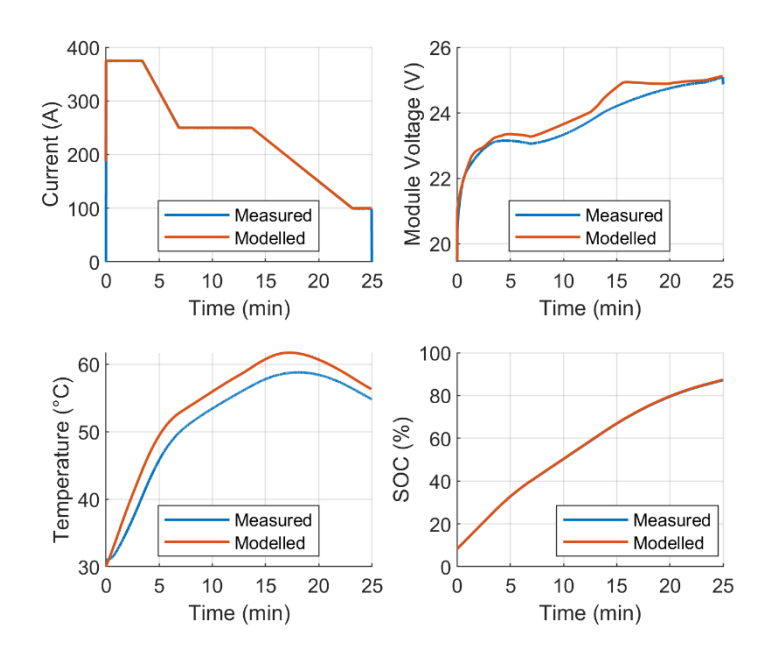


Figure 7.6: Modelled and measured data for the fastest charging profile within constraints

The maximum temperature obtained experimentally is 58.8°C, while the model estimates a maximum temperature of 61.8°C. The root mean squared error of the temperature is 2.7°C while that of the voltage is 0.29 V. Once again, the results are in close alignment with the expected values.

Figure shows a comparison of the designed profile against the Taycan profile. The maximum temperature from the designed profile is 0.7°C less than that obtained from the Taycan profile, while also decreasing the charging time by approximately 3%, and Figure gives a distribution of the cell surface temperatures at the point when the overall maximum surface temperature occurs at A1.

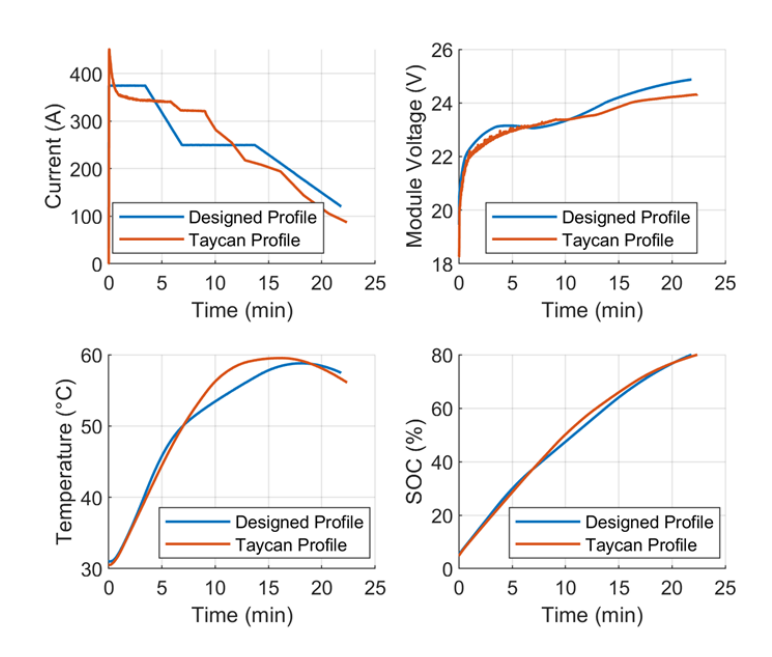


Figure 7.7: Comparison of the fastest charging profile within constraints with the Taycan profile

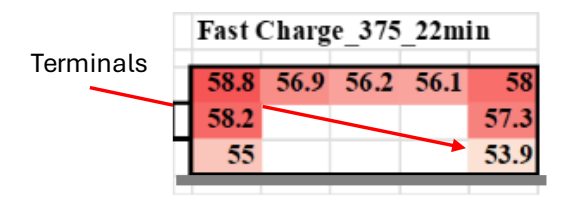


Figure 7.8: Cell surface temperature distribution when T_{cell} is maximum for the fastest 22-minute profile within constraints

The maximum temperature variation across the cell surface at this instant is 4.9°C. However, the maximum temperature variation of 5.6°C also does not occur at this point, but instead when A1 is at 57.6°C, moments after the peak cell surface temperature is reached, due to the inlet coolant temperature being at minimum, and the heat generation of the battery reducing. This is about the same temperature variation obtained using the Taycan profile, but with a profile that achieves faster charging with a lower peak cell surface temperature. This profile proves that it is possible to improve on the Porsche Taycan's fast-charging profile, and this has been verified experimentally.

8 Conclusions and Future Work

8.1 Summary and Conclusions

The aim of this work was to develop a fast-charging profile which can minimise the charging time of a battery module from a production EV without exceeding the temperature limit of 60°C. Because temperature has a significant impact on charging, the BTMS in fast-charging EVs were first reviewed, paying close attention to the predominant cooling media and the architectures of the cooling systems, while highlighting the strengths and limitations of the various approaches. Air-cooled vehicles were found lacking in terms of meeting the cooling requirements of the levels of DC charging we need to approach. Therefore, air cooling was not an option for the thermal management system of the module under study. The shortcomings of PCMs and heat pipes also rendered them poor choices for the purpose of this study and its usefulness in real-world applications. An edge-cooled architecture for a single module was chosen as the cooling system for the Taycan battery module.

A battery module from the Porsche Taycan EV, which has an 800 V powertrain architecture, was selected for this thesis. The LG-E66 cell used in this battery module was characterised and the battery module was extensively tested to observe its performance at different charging rates, and also assess the performance of the selected BTMS. In the module tests, the cell surface was also instrumented with several thermocouples to record the thermal behaviour of the cell within an actual module and record the temperature distribution on the cell surface during charging. The LG E-66 cell which is the cell used in the Taycan battery module, showed a strong performance

as a fast-charging cell, with a low internal resistance, and little capacity variation with

C-rates at temperatures 10, 25 and 40°C. The data from the extensive tests are necessary to create and validate the battery model created for the Porsche Taycan battery module. With experimental data on the performance of the Taycan battery module, it was also important to analyse the possible options for the fast-charging profiles that would meet the requirements of minimising charging time and temperature rise. Therefore, four main protocols which showed the most promise and low complexity in implementation

from reviewed literature were presented. An understanding of the pros and cons of each

one was required to choose which protocol would best meet the target of this work.

The voltage estimation model was then created for the LG E-66 cell, which gave good performance with a voltage RMSE of 0.0334 V on the US06 drive cycle test. However, scaling this up to the module level gave results with a higher voltage error of 0.22 V. It is important to mention that one parallel pair branch of cells in the battery module was performing poorly. This could have had an influence on the significant error obtained from the voltage prediction for the battery module. Because the cell was not instrumented with thermocouples for temperature measurement, the battery loss model could only be verified at the module level. Therefore, the error from the module voltage prediction had a significant impact on the temperature prediction, giving an RMSE of 2.9°C.

Using the electrothermal model, several fast-charging current profiles were simulated to obtain the optimal profile. The results showed that several profiles could potentially outperform the fast-charging profile used in the Taycan, both in terms of lower temperature rise and faster charging time. Two of the designed profiles were chosen for

experimental validation, one of which was the fastest profile which still kept the battery temperature under 60°C. This faster profile was designed to charge the module from 5 – 80% SOC within 21.75 minutes, which is a 3% reduction in charging time, while still giving a maximum temperature of 58.8°C, which is 0.7°C lower than what is obtained with the Taycan profile, thus, meeting the targets set for this work. Considering the small reduction in charging time obtained with the designed profile, one can assume that Porsche may have followed a similar design process and selected a different profile.

8.2 Recommendations and Future Work

While this thesis successfully presents a method to design more efficient fast-charging profiles, the first gap identified is the concern over battery aging. This thesis does not consider the impact of subjecting the battery module to frequent fast charging and, hence, high temperatures, which are known to affect battery life. It would be important to perform subsequent studies on how the designed profiles influence the aging of the battery module compared to the Taycan profile. The fast-charging design procedure could also be researched further for a mid-life battery pack. The battery parameters such as capacity and resistance change as the battery ages. Therefore, making this fast-charging design process more health aware would improve its relevance to production EVs.

In addition to this, the voltage estimation model has a lot of room for improvement. The impact of voltage estimation errors on the temperature prediction was shown here. Therefore, the accuracy of the voltage estimation model still needs to be improved upon in order to generate more accurate temperature prediction for the different fast-charging profiles generated. The heat loss model accuracy could also be further improved by

considering the entropic heat loss term. This would involve additional testing, which is time consuming, however, an alternative would be to employ the method presented by (Damay et al., 2016) which achieves good results using experiments that only take a few hours to complete. Another point which could be further researched is the use of an electrochemical-thermal model for the voltage and temperature estimation. The high accuracy of the electrochemical model will improve the overall accuracy of the combined model. Furthermore, the thermal model could also take into account the conduction that occurs between the cells. This could also further improve the accuracy of the temperature estimation.

Finally, the approach used in this thesis is a brute-force method which, although attempts were made to generate a wide range of profiles, does not cover the full spectrum of all possible fast-charging profiles. It is possible that the optimal profile was still not identified in this work. It would be important to use dynamic programming to solve this problem and generate the truly optimal fast-charging profile.

Appendix A

Table A.1: Sample of 15 generated duration combinations for the ramped step with initial step current profile (219 A option)

1	2	3	4	5	6
Duration_375A	Duration_250A	Duration_100A	Ramp1_Duration	Ramp2_Duration	T_to_80
56	84	100	414	776	1485
56	84	100	414	828	1447
56	84	100	466	672	1453
56	84	100	466	724	1414
56	84	100	466	776	1383
56	84	100	517	621	1383
56	84	100	517	672	1350
56	84	100	569	517	1350
56	84	100	569	569	1315
56	84	200	466	621	1491
56	84	200	466	672	1453
56	84	200	517	517	1461
56	84	200	517	569	1422
56	84	200	517	621	1383
56	84	200	569	466	1388

Table A.2: Sample of 15 generated duration combinations for the ramped step with initial step current profile (283 A option)

1	2	3	4	5	6
Duration_375A	Duration_250A	Duration_100A	Ramp1_Duration	Ramp2_Duration	T_to_80
56	84	100	362	879	1497
56	84	100	414	776	1464
56	84	100	414	828	1426
56	84	100	466	672	1431
56	84	100	466	724	1393
56	84	100	466	776	1362
56	84	100	517	621	1361
56	84	100	517	672	1329
56	84	100	569	517	1329
56	84	100	569	569	1294
56	84	200	466	621	1470
56	84	200	466	672	1431
56	84	200	517	517	1439
56	84	200	517	569	1400
56	84	200	517	621	1361

Table A.3: Sample of 15 generated duration combinations for the ramped step with initial step current profile (358 A option)

1	2	3	4	5	6
Duration_375A	Duration_250A	Duration_100A	Ramp1_Duration	Ramp2_Duration	T_to_80
56	84	100	362	879	1481
56	84	100	414	776	1448
56	84	100	414	828	1410
56	84	100	466	672	1416
56	84	100	466	724	1377
56	84	100	466	776	1346
56	84	100	517	621	1346
56	84	100	517	672	1313
56	84	100	569	517	1313
56	84	100	569	569	1278
56	84	200	414	724	1487
56	84	200	466	621	1454
56	84	200	466	672	1416
56	84	200	517	517	1424
56	84	200	517	569	1385

Table A.4: Sample of 15 generated duration combinations for the ramped step with initial step current profile (400 A option)

1	2	3	4	5	6
Duration_375A	Duration_250A	Duration_100A	Ramp1_Duration	Ramp2_Duration	T_to_80
56	84	100	362	879	1475
56	84	100	414	776	1442
56	84	100	414	828	1404
56	84	100	466	672	1410
56	84	100	466	724	1371
56	84	100	466	776	1340
56	84	100	517	621	1339
56	84	100	517	672	1307
56	84	100	569	517	1307
56	84	100	569	569	1272
56	84	200	414	724	1481
56	84	200	466	621	1448
56	84	200	466	672	1410
56	84	200	517	517	1417
56	84	200	517	569	1378

Table A.5: Sample of 15 generated duration combinations for the ramped step with initial step current profile (500 A option)

1	2	3	4	5	6
Duration_375A	Duration_250A	Duration_100A	Ramp1_Duration	Ramp2_Duration	T_to_80
56	84	100	362	879	1468
56	84	100	414	776	1435
56	84	100	414	828	1396
56	84	100	466	672	1402
56	84	100	466	724	1363
56	84	100	466	776	1332
56	84	100	517	621	1332
56	84	100	517	672	1299
56	84	200	414	724	1474
56	84	200	466	621	1440
56	84	200	466	672	1402
56	84	200	517	517	1410
56	84	200	517	569	1371
56	84	200	517	621	1332
56	84	300	466	569	1479

Appendix B

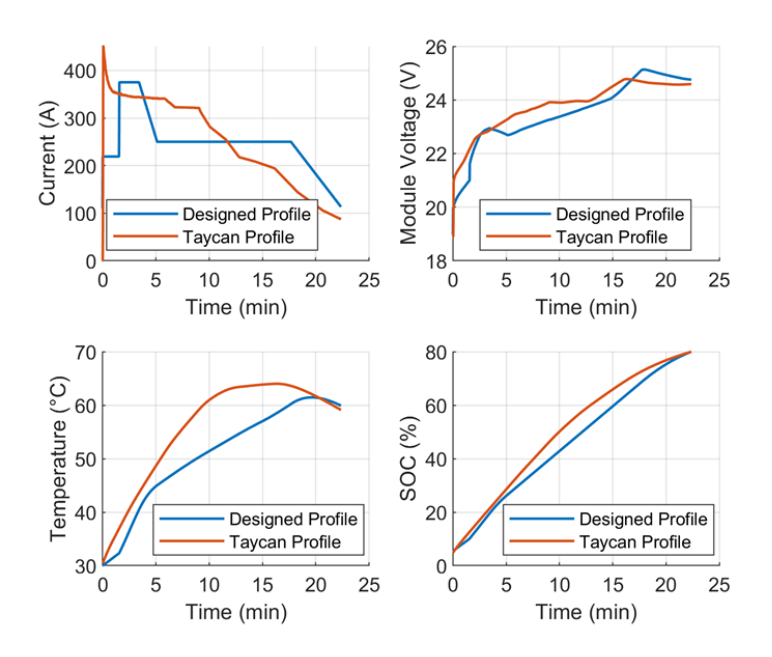


Figure B.1: Simulated performance of the ramped step with initial 219 A step current profile for 80% charge time of 22.4 minutes compared to the simulated Taycan profile

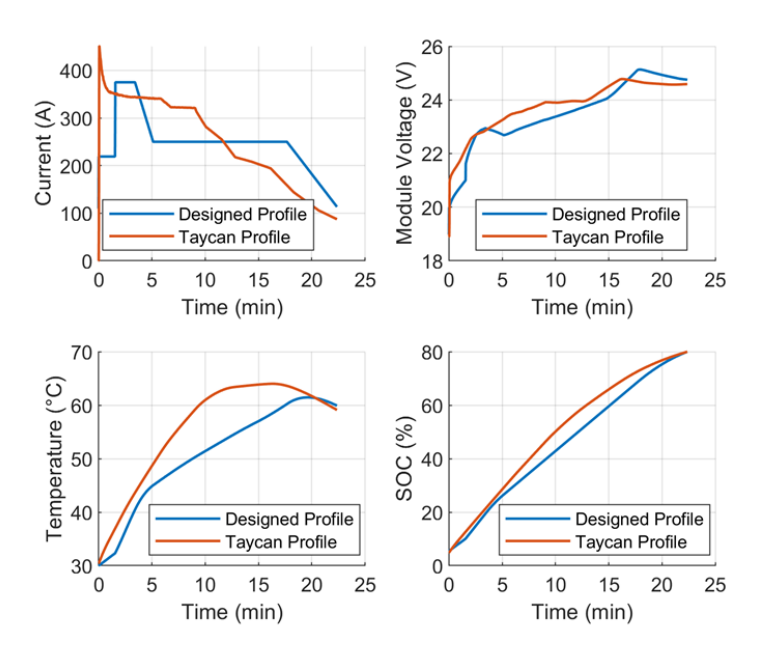


Figure B.2: Simulated performance of the ramped step with initial 283 A step current profile for 80% charge time of 22.4 minutes compared to the simulated Taycan profile

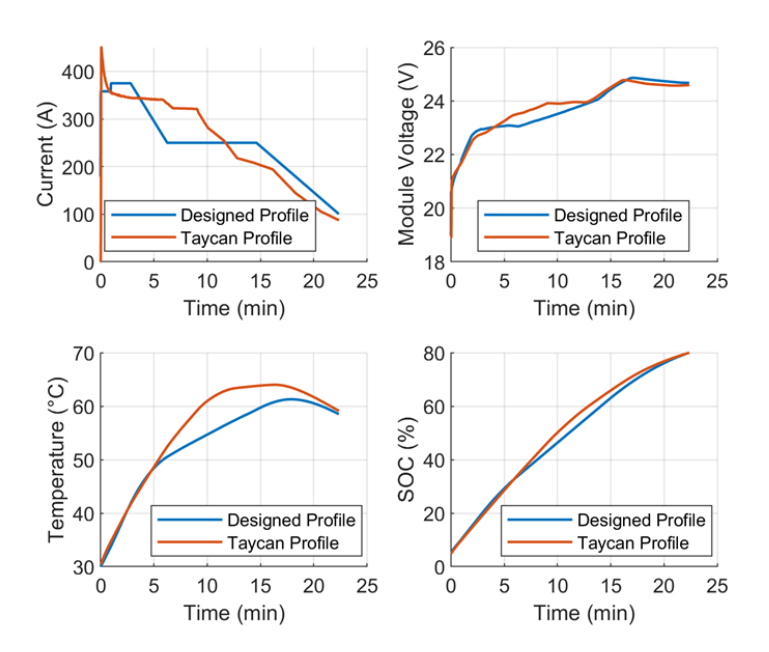


Figure B.3: Simulated performance of the ramped step with initial 358 A step current profile for 80% charge time of 22.4 minutes compared to the simulated Taycan profile

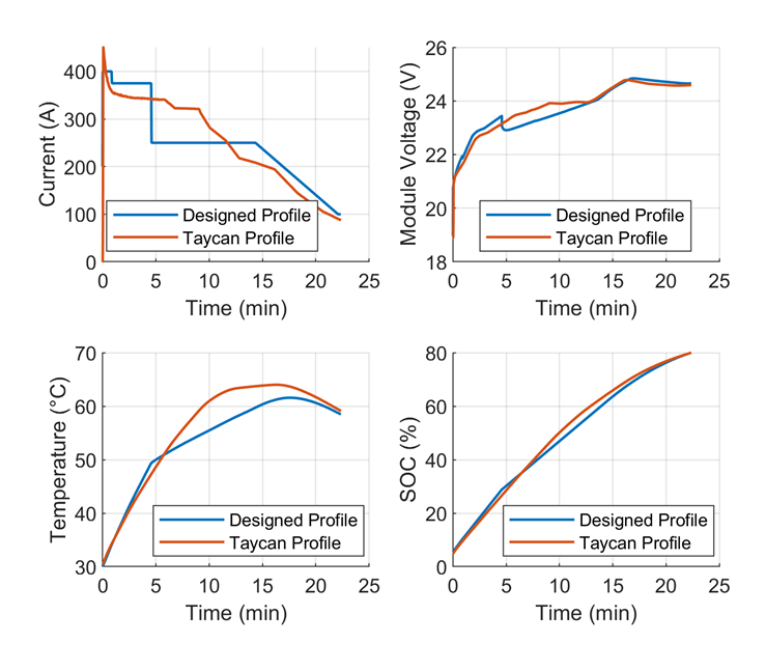


Figure B.4: Simulated performance of the ramped step with initial 400 A step current profile for 80% charge time of 22.4 minutes compared to the simulated Taycan profile

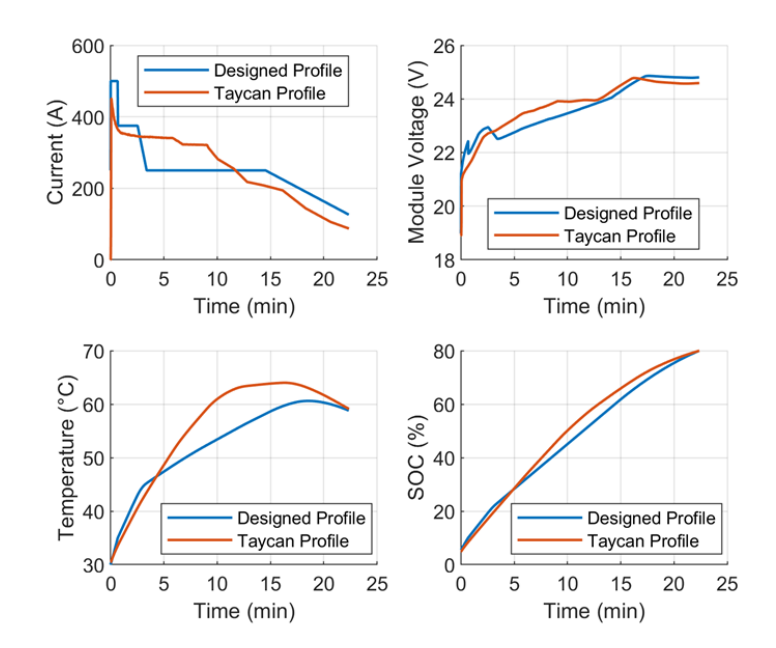


Figure B.5: Simulated performance of the ramped step with initial 500 A step current profile for 80% charge time of 24.2 minutes

References

- 10 Biggest Challenges Facing the EV Industry Today EV Charging Summit Blog.
 (n.d.). Retrieved May 26, 2024, from https://evchargingsummit.com/blog/challenges-facing-the-ev-industry-today/
- Akbarzadeh, M., Kalogiannis, T., Jaguemont, J., Jin, L., Behi, H., Karimi, D., Beheshti, H., Van Mierlo, J., & Berecibar, M. (2021). A comparative study between air cooling and liquid cooling thermal management systems for a high-energy lithiumion battery module. *Applied Thermal Engineering*, 198, 117503. https://doi.org/10.1016/j.applthermaleng.2021.117503
- Al-Hallaj, S., & Selman, J. R. (2002). Thermal modeling of secondary lithium batteries for electric vehicle/hybrid electric vehicle applications. *Journal of Power Sources*, *110*(2), 341–348. https://doi.org/10.1016/S0378-7753(02)00196-9
- Audi Q8 e-tron | Audi MediaCenter. (n.d.). Retrieved October 5, 2023, from https://www.audi-mediacenter.com/en/photos/album/audi-q8-e-tron-2132
- Bandhauer, T. M., Garimella, S., & Fuller, T. F. (2011). A Critical Review of Thermal Issues in Lithium-Ion Batteries. *Journal of The Electrochemical Society*, *158*(3), R1. https://doi.org/10.1149/1.3515880
- Bernagozzi, M., Georgoulas, A., Miché, N., & Marengo, M. (2023). Heat pipes in battery thermal management systems for electric vehicles: A critical review. In *Applied Thermal Engineering* (Vol. 219, p. 119495). Pergamon. https://doi.org/10.1016/j.applthermaleng.2022.119495

- Bose, B., Garg, A., Panigrahi, B. K., & Kim, J. (2022). Study on Li-ion battery fast charging strategies: Review, challenges and proposed charging framework.

 **Journal of Energy Storage*, 55, 105507*. https://doi.org/10.1016/J.EST.2022.105507*
- Cano, Z. P., Banham, D., Ye, S., Hintennach, A., Lu, J., Fowler, M., & Chen, Z. (2018).

 Batteries and fuel cells for emerging electric vehicle markets. In *Nature Energy*(Vol. 3, Issue 4, pp. 279–289). Nature Publishing Group.

 https://doi.org/10.1038/s41560-018-0108-1
- Charger Types and Speeds | US Department of Transportation. (n.d.). Retrieved May 26, 2024, from https://www.transportation.gov/rural/ev/toolkit/ev-basics/charging-speeds
- Chen, L. R. (2007). A design of an optimal battery pulse charge system by frequency-varied technique. *IEEE Transactions on Industrial Electronics*, *54*(1), 398–405. https://doi.org/10.1109/TIE.2006.888796
- Damay, N., Forgez, C., Bichat, M. P., & Friedrich, G. (2016). A method for the fast estimation of a battery entropy-variation high-resolution curve Application on a commercial LiFePO4/graphite cell. *Journal of Power Sources*, *332*, 149–153. https://doi.org/10.1016/j.jpowsour.2016.09.083
- Duan, J., Tang, X., Dai, H., Yang, Y., Wu, W., Wei, X., & Huang, Y. (2020). Building Safe Lithium-Ion Batteries for Electric Vehicles: A Review. In *Electrochemical Energy Reviews* (Vol. 3, Issue 1, pp. 1–42). Springer. https://doi.org/10.1007/s41918-019-00060-4

- Duru, K. K., Karra, C., Venkatachalam, P., Betha, S. A., Anish Madhavan, A., & Kalluri, S. (2021). Critical Insights into Fast Charging Techniques for Lithium-Ion Batteries in Electric Vehicles. *IEEE Transactions on Device and Materials Reliability*, 21(1), 137–152. https://doi.org/10.1109/TDMR.2021.3051840
- from https://www.youtube.com/watch?v=kY-F8dzyUjs&list=PLkiDlGyJnprd2EdkNDAAGpHcU6n4wxZoe&index=9
- Falvo, M. C., Sbordone, D., Bayram, I. S., & Devetsikiotis, M. (2014). EV charging stations and modes: International standards. 2014 International Symposium on Power Electronics, Electrical Drives, Automation and Motion, SPEEDAM 2014, 1134–1139. https://doi.org/10.1109/SPEEDAM.2014.6872107
- Farhan, M., Amjad, M., Tahir, Z. ul R., Anwar, Z., Arslan, M., Mujtaba, A., Riaz, F., Imran, S., Razzaq, L., Ali, M., Filho, E. P. B., & Du, X. (2022). Design and Analysis of Liquid Cooling Plates for Different Flow Channel Configurations.
 Thermal Science, 26(2), 1463–1475. https://doi.org/10.2298/TSCI201111196F
- FIA Region I-Expert study on guidance and recommendations regarding electric vehicle propulsion battery end-of-life policies. (n.d.).
- Fotouhi, A., Auger, D. J., Propp, K., Longo, S., & Wild, M. (2016). A review on electric vehicle battery modelling: From Lithium-ion toward Lithium–Sulphur. *Renewable and Sustainable Energy Reviews*, 56, 1008–1021. https://doi.org/10.1016/J.RSER.2015.12.009

- Gao, Y., Zhang, X., Cheng, Q., Guo, B., & Yang, J. (2019). Classification and Review of the Charging Strategies for Commercial Lithium-Ion Batteries. *IEEE Access*, 7, 43511–43524. https://doi.org/10.1109/ACCESS.2019.2906117
- Gazzarri, J. (2024). *Battery Modeling*. MATLAB Central File Exchange. https://www.mathworks.com/matlabcentral/fileexchange/36019-battery-modeling
- Ghaeminezhad, N., Wang, Z., & Ouyang, Q. (2023). A Review on lithium-ion battery thermal management system techniques: A control-oriented analysis. *Applied Thermal Engineering*, 219, 119497. https://doi.org/10.1016/j.applthermaleng.2022.119497
- Ghalkhani, M., & Habibi, S. (2023). Review of the Li-Ion Battery, Thermal Management, and AI-Based Battery Management System for EV Application. In *Energies* (Vol. 16, Issue 1, p. 185). Multidisciplinary Digital Publishing Institute. https://doi.org/10.3390/en16010185
- Goli, P., Legedza, S., Dhar, A., Salgado, R., Renteria, J., & Balandin, A. A. (2014). Graphene-enhanced hybrid phase change materials for thermal management of Liion batteries. *Journal of Power Sources*, 248, 37–43. https://doi.org/10.1016/j.jpowsour.2013.08.135
- Gurjer, L., Chaudhary, P., & Verma, H. K. (2019). Detailed Modelling Procedure for Lithium-ion Battery Using Thevenin Equivalent. *Proceedings of 2019 3rd IEEE International Conference on Electrical, Computer and Communication Technologies, ICECCT 2019*. https://doi.org/10.1109/ICECCT.2019.8869224

- Hossain, M., Saha, S., Haque, M. E., Arif, M. T., & Oo, A. M. T. (2019). A Parameter Extraction Method for the Thevenin Equivalent Circuit Model of Li-ion Batteries.

 2019 IEEE Industry Applications Society Annual Meeting, IAS 2019. https://doi.org/10.1109/IAS.2019.8912326
- Hou, J., Yang, M., Wang, D., & Zhang, J. (2020). Fundamentals and Challenges of Lithium Ion Batteries at Temperatures between -40 and 60 °C. In *Advanced Energy Materials* (Vol. 10, Issue 18). https://doi.org/10.1002/aenm.201904152
- Huang, X., Meng, J., Liu, W., Ru, F., Duan, C., Xu, X., Stroe, D. I., & Teodorescu, R.
 (2024). Lithium-Ion Battery Lifetime Extension with Positive Pulsed Current
 Charging. *IEEE Transactions on Industrial Electronics*, 71(1), 484–492.
 https://doi.org/10.1109/TIE.2023.3250850
- Iraola, U., Aizpuru, I., Canales, J. M., Etxeberria, A., & Gil, I. (2013). Methodology for thermal modelling of lithium-ion batteries. *IECON Proceedings (Industrial Electronics Conference)*, 6752–6757. https://doi.org/10.1109/IECON.2013.6700250
- Johnson, V. H. (2002). Battery performance models in ADVISOR. *Journal of Power Sources*, *110*(2), 321–329. https://doi.org/10.1016/S0378-7753(02)00194-5
- Karimi, G., & Li, X. (2013). Thermal management of lithium-ion batteries for electric vehicles. *International Journal of Energy Research*, 37(1), 13–24. https://doi.org/10.1002/ER.1956
- Khan, A. B., Pham, V. L., Nguyen, T. T., & Choi, W. (2016). Multistage constant-current charging method for Li-Ion batteries. 2016 IEEE Transportation Electrification

- Conference and Expo, Asia-Pacific, ITEC Asia-Pacific 2016, 381–385. https://doi.org/10.1109/ITEC-AP.2016.7512982
- Kumar Thakur, A., Sathyamurthy, R., Velraj, R., Saidur, R., Pandey, A. K., Ma, Z.,
 Singh, P., Hazra, S. K., Wafa Sharshir, S., Prabakaran, R., Kim, S. C., Panchal, S.,
 & Ali, H. M. (2023). A state-of-the art review on advancing battery thermal management systems for fast-charging. *Applied Thermal Engineering*, 226, 120303. https://doi.org/10.1016/j.applthermaleng.2023.120303
- Kurmaev, R. K., Struchkov, V. S., & Novak, V. V. (2020). Experience in the development of an effective thermal management system for the high-voltage battery of the vehicle. *IOP Conference Series: Materials Science and Engineering*, 819(1). https://doi.org/10.1088/1757-899X/819/1/012020
- Li, X., Zhao, J., Duan, J., Panchal, S., Yuan, J., Fraser, R., Fowler, M., & Chen, M. (2022). Simulation of cooling plate effect on a battery module with different channel arrangement. *Journal of Energy Storage*, 49, 104113. https://doi.org/10.1016/j.est.2022.104113
- Liu, C., Xu, D., Weng, J., Zhou, S., Li, W., Wan, Y., Jiang, S., Zhou, D., Wang, J., & Huang, Q. (2020). Phase change materials application in battery thermal management system: A review. In *Materials* (Vol. 13, Issue 20, pp. 1–37).
 Multidisciplinary Digital Publishing Institute (MDPI). https://doi.org/10.3390/ma13204622
- Liu, J., & Wang, X. (2023). Investigating effects of pulse charging on performance of Li-ion batteries at low temperature. *Journal of Power Sources*, 574, 233177. https://doi.org/10.1016/J.JPOWSOUR.2023.233177

- Lu, Z., Yu, X. L., Wei, L. C., Cao, F., Zhang, L. Y., Meng, X. Z., & Jin, L. W. (2019). A comprehensive experimental study on temperature-dependent performance of lithium-ion battery. *Applied Thermal Engineering*, 158, 113800. https://doi.org/10.1016/j.applthermaleng.2019.113800
- Lucid Air | Performance. (n.d.). Retrieved October 5, 2023, from https://www.lucidmotors.com/air/performance
- Luo, J., Zou, D., Wang, Y., Wang, S., & Huang, L. (2022). Battery thermal management systems (BTMs) based on phase change material (PCM): A comprehensive review.

 In *Chemical Engineering Journal* (Vol. 430, p. 132741). Elsevier. https://doi.org/10.1016/j.cej.2021.132741
- Mach-E: Battery Tray and Battery Cell Features YouTube. (n.d.). Retrieved January 20, 2024, from https://www.youtube.com/watch?v=4vRjo0gaG1g&t=184s
- Mai, W., Colclasure, A. M., & Smith, K. (2020). Model-Instructed Design of Novel Charging Protocols for the Extreme Fast Charging of Lithium-Ion Batteries Without Lithium Plating. *Journal of The Electrochemical Society*, *167*(8), 080517. https://doi.org/10.1149/1945-7111/ab8c84
- Makeen, P., Ghali, H. A., & Memon, S. (2022). A Review of Various Fast Charging Power and Thermal Protocols for Electric Vehicles Represented by Lithium-Ion Battery Systems. *Future Transportation 2022, Vol. 2, Pages 281-299*, 2(1), 281–299. https://doi.org/10.3390/FUTURETRANSP2010015
- Malik, M., Dincer, I., Rosen, M., & Fowler, M. (2017). Experimental Investigation of a New Passive Thermal Management System for a Li-Ion Battery Pack Using Phase

- Change Composite Material. *Electrochimica Acta*, 257, 345–355. https://doi.org/10.1016/J.ELECTACTA.2017.10.051
- Manwell, J. F., & McGowan, J. G. (1993). Lead acid battery storage model for hybrid energy systems. *Solar Energy*, 50(5), 399–405. https://doi.org/10.1016/0038-092X(93)90060-2
- Miao, Y., Hynan, P., Von Jouanne, A., & Yokochi, A. (2019). Current li-ion battery technologies in electric vehicles and opportunities for advancements. In *Energies* (Vol. 12, Issue 6, p. 1074). Multidisciplinary Digital Publishing Institute. https://doi.org/10.3390/en12061074
- Michael, L. K., K V, S., Hungund, S. S., & Fernandes, M. (2022). Factors influencing adoption of electric vehicles—A case in India. *Cogent Engineering*, 9(1). https://doi.org/10.1080/23311916.2022.2085375
- Monika, K., & Datta, S. P. (2022). Comparative assessment among several channel designs with constant volume for cooling of pouch-type battery module. *Energy Conversion and Management*, 251. https://doi.org/10.1016/j.enconman.2021.114936
- Mousavi G., S. M., & Nikdel, M. (2014). Various battery models for various simulation studies and applications. *Renewable and Sustainable Energy Reviews*, *32*, 477–485. https://doi.org/10.1016/J.RSER.2014.01.048
- Mpoi, G., Milioti, C., & Mitropoulos, L. (2023). Factors and incentives that affect electric vehicle adoption in Greece. *International Journal of Transportation*

Science and Technology, 12(4), 1064–1079. https://doi.org/10.1016/j.ijtst.2023.01.002

- Najafi Khaboshan, H., Jaliliantabar, F., Adam Abdullah, A., & Panchal, S. (2023). Improving the cooling performance of cylindrical lithium-ion battery using three passive methods in a battery thermal management system. *Applied Thermal Engineering*, 227, 120320. https://doi.org/10.1016/j.applthermaleng.2023.120320
- NISSAN | NISSAN TECHNICAL REVIEW 2022 no. 88. (2022). https://www.nissan-global.com/EN/TECHNICALREVIEW/
- Notten, P. H. L., Veld, J. H. G. O. H., & Van Beek, J. R. G. (2005). Boostcharging Liion batteries: A challenging new charging concept. *Journal of Power Sources*, 145(1), 89–94. https://doi.org/10.1016/J.JPOWSOUR.2004.12.038
- Peng, X., Garg, A., Zhang, J., & Shui, L. (2017). Thermal management system design for batteries packs of electric vehicles: A survey. 2017 Asian Conference on Energy, Power and Transportation Electrification, ACEPT 2017, 2017-Decem, 1– 5. https://doi.org/10.1109/ACEPT.2017.8168557
- Pesaran, A. A. (2002). Battery thermal models for hybrid vehicle simulations. *Journal of Power Sources*, 110(2), 377–382. https://doi.org/10.1016/S0378-7753(02)00200-8
- Porsche. (2023). *The Battery: Sophisticated thermal management, up to 800-volt system voltage*. Porsche Newsroom. https://newsroom.porsche.com/en/products/taycan/battery-18557.html

- Porsche Taycan 0 to 100% DC Fast Charge Test YouTube. (n.d.). Retrieved April 9, 2024, from https://www.youtube.com/watch?v=PrkAeTWDed4&t=1165s
- Rachid, A., El Fadil, H., Gaouzi, K., Rachid, K., Lassioui, A., El Idrissi, Z., & Koundi,
 M. (2023). Electric Vehicle Charging Systems: Comprehensive Review. In
 Energies (Vol. 16, Issue 1, p. 255). Multidisciplinary Digital Publishing Institute.
 https://doi.org/10.3390/en16010255
- Rajan, J. T., Jayapal, V. S., Krishna, M. J., Mohammed Firose, K. A., Vaisakh, S., John,
 A. K., & Suryan, A. (2022). Analysis of Battery Thermal Management System for
 Electric Vehicles using 1-Tetradecanol Phase Change Material. Sustainable Energy
 Technologies and Assessments, 51, 101943.
 https://doi.org/10.1016/J.SETA.2021.101943
- Rao, V., Singhai, G., Kumar, A., & Navet, N. (2005). Battery model for embedded systems. *Proceedings of the IEEE International Conference on VLSI Design*, 105–110. https://doi.org/10.1109/ICVD.2005.61
- Salameh, Z. M., Casacca, M. A., & Lynch, W. A. (1992). A mathematical model for lead-acid batteries. *IEEE Transactions on Energy Conversion*, 7(1), 93–98. https://doi.org/10.1109/60.124547
- Shabani, B., & Biju, M. (2015). Theoretical Modelling Methods for Thermal Management of Batteries. *Energies 2015, Vol. 8, Pages 10153-10177*, 8(9), 10153–10177. https://doi.org/10.3390/EN80910153
- Shen, W., Vo, T. T., & Kapoor, A. (2012). Charging algorithms of lithium-ion batteries:

 An overview. *Proceedings of the 2012 7th IEEE Conference on Industrial*

- *Electronics and Applications, ICIEA 2012*, 1567–1572. https://doi.org/10.1109/ICIEA.2012.6360973
- Sieg, J., Bandlow, J., Mitsch, T., Dragicevic, D., Materna, T., Spier, B., Witzenhausen, H., Ecker, M., & Sauer, D. U. (2019). Fast charging of an electric vehicle lithium-ion battery at the limit of the lithium deposition process. *Journal of Power Sources*, 427, 260–270. https://doi.org/10.1016/J.JPOWSOUR.2019.04.047
- Tamilselvi, S., Gunasundari, S., Karuppiah, N., Razak Rk, A., Madhusudan, S., Nagarajan, V. M., Sathish, T., Shamim, M. Z. M., Saleel, C. A., & Afzal, A. (2021).
 A Review on Battery Modelling Techniques. *Sustainability 2021, Vol. 13, Page 10042*, 13(18), 10042. https://doi.org/10.3390/SU131810042
- Tanim, T. R., Shirk, M. G., Bewley, R. L., Dufek, E. J., & Liaw, B. Y. (2018). The Implications of Fast Charge in Lithium Ion Battery Performance and Life: Cell vs. Pack. ECS Meeting Abstracts, MA2018-01(1), 121–121. https://doi.org/10.1149/ma2018-01/1/121
- Tesla Model S Plaid Battery: Clever New Advancements Discovered. (n.d.). Retrieved October 5, 2023, from https://insideevs.com/news/566047/tesla-models-clever-battery-advancements/
- Tomaszewska, A., Chu, Z., Feng, X., O'Kane, S., Liu, X., Chen, J., Ji, C., Endler, E., Li, R., Liu, L., Li, Y., Zheng, S., Vetterlein, S., Gao, M., Du, J., Parkes, M., Ouyang, M., Marinescu, M., Offer, G., & Wu, B. (2019). Lithium-ion battery fast charging:
 A review. In *eTransportation* (Vol. 1, p. 100011). Elsevier. https://doi.org/10.1016/j.etran.2019.100011

- Uwalaka, L., & Kollmeyer, P. (n.d.). Fast Charging EVs Cooling Systems. Retrieved January 27, 2024, from https://doi.org/10.5683/SP3/6B9BBE
- Uwalaka, L., Yao, Q., Duque, J., & Kollmeyer, P. J. (n.d.). Fast Charging and Characterization Dataset for Porsche Taycan LG E66 Battery Cell and Module. https://doi.org/https://doi.org/10.5683/SP3/7JP3NM
- Vidal, C., Gross, O., Gu, R., Kollmeyer, P., & Emadi, A. (2019). XEV Li-Ion Battery Low-Temperature Effects-Review. *IEEE Transactions on Vehicular Technology*, 68(5), 4560–4572. https://doi.org/10.1109/TVT.2019.2906487
- Wang, Y., Gao, Q., Wang, G., Lu, P., Zhao, M., & Bao, W. (2018). A review on research status and key technologies of battery thermal management and its enhanced safety. In *International Journal of Energy Research* (Vol. 42, Issue 13, pp. 4008–4033). John Wiley and Sons Ltd. https://doi.org/10.1002/er.4158
- Wassiliadis, N., Schneider, J., Frank, A., Wildfeuer, L., Lin, X., Jossen, A., & Lienkamp, M. (2021). Review of fast charging strategies for lithium-ion battery systems and their applicability for battery electric vehicles. *Journal of Energy Storage*, 44, 103306. https://doi.org/10.1016/J.EST.2021.103306
- Wazeer, A., Das, A., Abeykoon, C., Sinha, A., & Karmakar, A. (2022). Phase change materials for battery thermal management of electric and hybrid vehicles: A review. *Energy Nexus*, 7, 100131. https://doi.org/10.1016/j.nexus.2022.100131
- Weragoda, D. M., Tian, G., Burkitbayev, A., Lo, K. H., & Zhang, T. (2023). A comprehensive review on heat pipe based battery thermal management systems.

- In *Applied Thermal Engineering* (Vol. 224, p. 120070). Pergamon. https://doi.org/10.1016/j.applthermaleng.2023.120070
- Widyantara, R. D., Zulaikah, S., Juangsa, F. B., Budiman, B. A., & Aziz, M. (2022).

 Review on Battery Packing Design Strategies for Superior Thermal Management in Electric Vehicles. *Batteries*, 8(12), 287–287.

 https://doi.org/10.3390/BATTERIES8120287
- Wu, W., Yang, X., Zhang, G., Ke, X., Wang, Z., Situ, W., Li, X., & Zhang, J. (2016). An experimental study of thermal management system using copper mesh-enhanced composite phase change materials for power battery pack. *Energy*, 113, 909–916. https://doi.org/10.1016/j.energy.2016.07.119
- Zhang, C., Li, K., McLoone, S., & Yang, Z. (2014). Battery modelling methods for electric vehicles A review. 2014 European Control Conference, ECC 2014, 2673–2678. https://doi.org/10.1109/ECC.2014.6862541
- Zhang, X., Li, Z., Luo, L., Fan, Y., & Du, Z. (2022). A review on thermal management of lithium-ion batteries for electric vehicles. *Energy*, 238. https://doi.org/10.1016/j.energy.2021.121652
- Zhang, X., Liu, C., & Rao, Z. (2018). Experimental investigation on thermal management performance of electric vehicle power battery using composite phase change material. *Journal of Cleaner Production*, 201, 916–924. https://doi.org/10.1016/j.jclepro.2018.08.076
- Zhang, X., Zhang, W., & Lei, G. (2016). *A Review of Li-ion Battery Equivalent Circuit Models*. 17(6), 311–316. https://doi.org/10.4313/TEEM.2016.17.6.311

M.A.Sc. Thesis – L. Uwalaka; McMaster University – Electrical and Computer Engineering

Zhao, Z. (2021). Testing and Thermal Management System Design of an Ultra-Fast

Charging Battery Module for Electric Vehicles.

https://macsphere.mcmaster.ca/handle/11375/27017